SANDIA REPORT
SAND2002-0807
Unlimited Release
Printed March 2002

On the Development of the Large Eddy Simulation Approach for Modeling Turbulent Flow: LDRD Final Report

Rodney C. Schmidt, Thomas M. Smith, Paul E. DesJardin, Thomas E. Voth, Mark A. Christon, Alan R. Kerstein, and Scott Wunsch

Prepared by
Sandia National Laboratories
Albuquerque, New Mexico 87185 and Livermore, California 94550

Sandia is a multiprogram laboratory operated by Sandia Corporation, a Lockheed Martin Company, for the United States Department of Energy under Contract DE-AC04-94AL85000.

Issued by Sandia National Laboratories, operated for the United States Department of Energy by Sandia Corporation.

Available to DOE and DOE contractors from
U.S. Department of Energy
Office of Scientific and Technical Information
P.O. Box 62
Oak Ridge, TN 37831

Telephone: (865)576-8401
Facsimile: (865)576-5728
E-Mail: reports@adonis.osti.gov
Online ordering: http://www.doe.gov/bridge

Available to the public from
U.S. Department of Commerce
National Technical Information Service
5285 Port Royal Rd
Springfield, VA 22161

Telephone: (800)553-6847
Facsimile: (703)605-6900
E-Mail: orders@ntis.fedworld.gov
Online order: http://www.ntis.gov/ordering.htm

SAND2002-0807
Unlimited Release
Printed March 2002

On the Development of the Large Eddy Simulation Approach for Modeling Turbulent Flow: LDRD Final Report

Rodney C. Schmidt and Thomas M. Smith
Computational Sciences Department

Paul E. DesJardin
Fire Science and Technology Department

Thomas E. Voth and Mark A. Christon
Computational Physics Research and Development Department

Sandia National Laboratories
P.O. Box 5800
Albuquerque, NM 87185

Alan R. Kerstein and Scott Wunsch
Reacting Flow Research Department
Sandia National Laboratories
Livermore, CA 94551

Abstract

This report describes research and development of the large eddy simulation (LES) turbulence modeling approach conducted as part of Sandia's laboratory directed research and development (LDRD) program. The emphasis of the work described here has been toward developing the capability to perform accurate and computationally affordable LES calculations of engineering problems using unstructured-grid codes, in wall-bounded geometries and for problems with coupled physics. Specific contributions documented here include (1) the implementation and testing of LES models in Sandia codes, including tests of a new conserved scalar - laminar flamelet SGS combustion model that does not assume statistical independence between the mixture fraction and the scalar dissipation rate, (2) the development and testing of statistical analysis and visualization utility software developed for Exodus II unstructured grid LES, and (3) the development and testing of a novel new LES near-wall subgrid model based on the one-dimensional Turbulence (ODT) model.

Acknowledgments

This work was supported by the Laboratory Directed Research and Development (LDRD) program at Sandia National Laboratories.

Contents

List of Figures

1 Introduction

A vast number of engineering problems require an analysis of the effects of gaseous or liquid fluid flow in order to obtain adequate solutions. In some cases the flow is laminar, and even sometimes steady; a fortunate situation where a variety of well developed analytical and numerical approaches can be brought to bear to provide accurate solutions. However, in most problems of engineering interest laminar flows are the exception instead of the norm because turbulent flows are so much more common in nature. Turbulent flow is 3-dimensional, unsteady, irregular and chaotic in nature, and analytical solutions to the governing equations for turbulent flow are not possible. Experience has shown that accounting for turbulence effects is usually a challenge, and predicting a-priori the effects of turbulence often impossible. This is especially so in problems where the turbulent flow is coupled to other physical processes such as combustion and radiation heat transfer. Although direct numerical simulations (DNS) using high-order numerical approximations are in principle possible, the computational cost of such calculations is so large that DNS is at present only useful for the simplest of turbulent flows. Thus the development of methods for providing approximate solutions of turbulent flow problems has been an area of great interest in the scientific and engineering community for many years.

There are tremendous differences in complexity and range of applicability among turbulence models. Usually the cost of increased generality is a corresponding increase in complexity and computational effort. Current and historical approaches began with the use of simple empirical correlations that relate nondimensional parameters of the flow, such as Reynolds number, Grashof number and Prandtl number, to bulk parameters of interest such as the pressure drop, wall shear, or wall heat transfer. With the advent of computers, computational fluid dynamics (CFD) calculations could be performed to approximately solve various reduced forms of the governing equations describing the conservation of mass, momentum, and energy (as well as other parameters of interest). This has led to the development of a rich collection of turbulence models that continue to be developed, refined, and improved to this day.

Many models of great utility leverage the concept of time or ensemble averaging. This type of averaging is the basis for deriving the Reynolds-averaged Navier-Stokes (RANS) equations, which in turn form the basis for a host of turbulence models that are commonly used. When cast in this form, the modeling problem becomes one of computing the so - called Reynolds shear stress tensor, the term which represents the averaged effect of the time-dependent 3-D motions on the transport of momentum.

The simplest type of RANS based models are variations of the approach originally introduced by Prandtl [62]. This method relates knowledge of a mixing length "l", to the magnitude of the Reynolds shear stress through the concept of a turbulent or eddy viscosity as first proposed by Boussinesq [7]. One implication of models of this type is the presumed

equivalence between the "generation" and "destruction" of the turbulence quantities affecting the Reynolds shear stress. Application of the Prandtl mixing length method requires empirically determined knowledge of the mixing length, and a vast amount of experimental data has been gathered for this purpose. With todays computers, calculations are quick and relatively inexpensive. However, outside the domain for which an appropriate mixing length has been empirically determined the method cannot be applied with confidence.

More complex models based on the RANS equations have been developed which introduce additional transport equations for various statistical properties of interest. These turbulence quantities are then related to appropriate effective transport properties in the time-averaged momentum and scaler transport equations. These models are often categorized by the number of additional equations introduced, e.g. "one-equation models", "two-equation models", and so forth. This concept in turbulence modeling was first introduced by Kolmogorov [41] and Prandtl [63], but it was not until computers became available that these approaches could effectively be developed.

Many early one-equation models choose the turbulent kinetic energy "k", as the turbulence property of interest. To account for the near wall damping of turbulence, these models can be modified such that the turbulence viscosity includes a functional dependence on a local turbulence Reynolds number. Since, in this method, an appropriate length scale must still be prescribed algebraically according to previously determined empirical information, the method also suffers from a significant dependence on flow dependent empirical information.

A more recent innovation in the development of one-equation RANS turbulence models is the model of Spalart and Allmaras [71]. In this model, the Boussinesq eddy viscosity approximation is invoked, and a transport equation for the turbulent viscosity is developed. This model has proven to be significantly more accurate and robust than earlier one-equation models and is valid clear to the wall.

Two-equation turbulence models typically solve one transport equation for k, the turbulent kinetic energy. In addition, they also solve an equation for a parameter related to the local turbulence length scale. Choices for this parameter are varied, but three of the most common are "ϵ", the dissipation rate, "W", a pseudo-vorticity density, and "k*l", where l is a turbulence length scale. Because these quantities are related to each other, it can be shown that the real differences between the various models lie in the representation of the transport and source terms, and in the constants employed. Because "exact" equations governing both k and ϵ can be derived, the differences between the various models are introduced in the process of reducing these exact forms into a tractable approximate form suitable for computation. Modelers must choose which terms can be considered insignificant and dropped, and how best to approximate the higher-order correlations that remain. These choices, and the determination of the constants that are introduced, are the essence of turbulence modeling of this type.

"Reynolds stress" or "stress equation" type models add additional partial differential

equations which compute all of the components of the turbulent stress tensor.

In regions adjacent to solid walls, the character of turbulent motions is significantly altered. To properly account for this region, additional modifications must be made to the turbulent transport equations. This is usually done through the introduction of so-called low-Reynolds-number (LRN) functions. Thus any of the "n-equation" models mentioned earlier, if further modified to account for this effect, can be referred to as a LRN form of that particular model.

Despite years of development, RANS based modeling has yielded only limited predictive capabilities. As faster computers have become available, alternative and potentially more accurate modeling approaches have become more attractive. Of particular interest in this report is the large-eddy simulation (LES) approach.

In contrast to RANS methods, whose basic equations are derived by ensemble or time averaging, the LES equations are obtained by applying the idea of spatial filtering. The governing equations derived by applying these ideas are time dependent and three dimensional — a vital feature of many engineering and environmental flows — but only account explicitly for turbulent motions larger than a certain "cut-off" length scale. These "large scale" motions are in general anisotropic and flow geometry dependent, and contain the bulk of the turbulent kinetic energy in the flow. To be accurate the LES must resolve a significant portion of these larger scale motions. To close the LES equations, a subgrid model is required in order to capture the effects of the unresolved small-scale turbulent motions on the resolved flow scales. These smaller scale motions are in general more isotropic in nature, account for most of the dissipation of the energy, and are considered easier to model. The fidelity required of a subgrid model to achieve acceptable overall predictions depends upon several factors, including the fineness of the resolved mesh, the type of problem being solved, and what aspects of the particular flow are important.

For turbulent flows with solid (i.e. no-slip) walls, the subgrid closure problem in the near-wall region is a particularly difficult problem that remains an area of active research. Briefly, this region is problematic for three reasons. First, the dominant flow scale at a given distance from the wall is of the order of that distance. Thus, the "large eddies" that must be captured on the mesh to perform an accurate LES shrink in size as one approaches the wall, leading to excessive computational costs. This problem is discussed by Baggett, who estimates that the number of grid points required for proper resolution scales as Re_τ^2. To some extent the computational expense can be mitigated by resolving only the near-wall region with a fine mesh. This requires non-uniform meshing techniques coupled with accurate numerics and LES models designed for non-uniform meshes. Although recent work has demonstrated some success in this area (see [42, 64]) the computational expense is still quite large, especially for higher Reynolds-number flows. A second problem is that uniform filtering becomes ill defined in the near-wall region when the filter width at a given point extends beyond the wall boundary. This introduces mathematical ambiguities that are difficult to reconcile. Finally,

the dynamics of the flow near the wall are strongly anisotropic, and the turbulence production in this region is associated with an up-scale energy cascade that is largely dominant over the commonly assumed down-scale energy cascade that is present elsewhere.

A relatively new and novel approach to turbulence modeling that is important to the work described here is the 'One-Dimensional Turbulence' (ODT) model. ODT can be viewed as a method for simulating, with spatial and temporal resolution comparable to direct numerical simulation, the evolution of the velocity vector and fluid properties along a one-dimensional (1D) line of sight through a 3D turbulent flow. ODT is an outgrowth of the linear-eddy model [34], in which fluid motions are prescribed without explicit introduction of a velocity field. By means of a detailed analogy between a 1D spatial random process and turbulent advection, this strategy has been implemented as a computational model that has shown remarkable success in various stand-alone calculations. The first ODT formulation [35] involved simulation of a single velocity component evolving on a line. A more recent formulation [36] introduced the evolution of the three-component velocity vector on the 1D domain and a generalization to treat variable-density effects dynamically is in progress.

In many respects ODT is complementary to conventional multidimensional turbulence modeling approaches that cannot afford the computational expense of resolving the fine scales of high intensity turbulence. Accordingly, ODT lacks important attributes of conventional approaches, yet captures important aspects of turbulence with fine-scale physiochemical processes and phenomena. A particular example of this that will developed here is to use ODT as a near-wall subgrid model for LES.

The remainder of the report is divided into three parts. The first part provides a review of the fundamental concepts and basic equations underlying the LES approach to turbulence modeling. Additional topics discussed include current closure models, the statistical analysis of turbulent flows, numerical errors, and the near-wall resolution and modeling problem.

The next part described the implementation and testing of LES models and utilities into MPSalsa [69], an unstructured-grid finite-element code developed at Sandia. Test results from calculations of isotropic turbulence decay in a box (a classic test problem) and results of simulations of a methanol pool fire are presented.

The final part of the report is a presentation of an LES near-wall subgrid model based on ODT. The ODT model is reviewed and the formulation of the ODT near-wall LES model is described in depth. Detailed results from applying the model to turbulent channel flow are presented as well as some preliminary calculations of turbulent flow over a backward facing step.

2 LES Concepts and Basic Equations

The classic way to obtain reduced forms of the Navier-Stokes equations which are suitable for introducing turbulence models is to apply the concepts of temporal, ensemble, and/or spatial filtering. For example, if temporal averaging is applied, the Reynolds-averaged Navier-Stokes (RANS) equations are obtained (they can also be obtained by using ensemble averaging ideas). In contrast, the LES equations are obtained by applying the idea of spatial filtering.

In this section we provide a short review of the concepts, theory, and basic equations that underlie the large eddy simulation (LES) approach to turbulence modeling. For convenience the equations are presented in incompressible isothermal form. Although most of the concepts discussed here are also applicable to compressible and variable density flow conditions, the more complex equations that arise under these conditions are not presented here.

2.1 Continuity and Navier Stokes Equations

For conditions where the fluid medium can be treated as a continuum, it is well accepted that turbulent flow is governed by the basic equations describing the conservation of mass and momentum (i.e. the continuity and Navier-Stokes equations). For an incompressible Newtonian fluid, the continuity and Navier-Stokes equations can be expressed in the following form.

$$\frac{\partial u_i}{\partial x_i} = 0 \tag{2.1}$$

$$\rho \frac{\partial u_i}{\partial t} + \rho \frac{\partial}{\partial x_j}(u_i u_j) = -\frac{\partial p}{\partial x_i} + \frac{\partial}{\partial x_j}\left[\mu\left(\frac{\partial u_i}{\partial x_j}\right)\right] + \rho f_i \tag{2.2}$$

where u_i is the velocity component in the x_i direction, ρ is the fluid density, f_i is a body force (e.g. gravity) in the x_i direction, p denotes pressure, and we use of the convention that repeated indices imply summation. When prescribed with boundary and initial conditions, these equations define the spatial and temporal behavior of the velocity components, u_i and the pressure, p.

Although closed form solutions to these equations can only be obtained for a very limited number of problems, solutions to discrete approximations are now possible for most laminar flows of interest using todays high speed computers and any of a number of numerical techniques (e.g. finite element, finite volume, etc.). However, in flows where the Reynolds number (Re) is large, the flow becomes turbulent and the range in length and time scales that must be resolved generally makes the direct numerical solution to these equations intractable for all but the simplest of problems. Thus for practical problems of engineering interest, turbulence modeling has become indispensable as a tool for obtaining approximate solutions.

2.2 Conceptual Framework of LES

A Fourier analysis of the 3-D velocity field in any turbulent flow reveals that the velocity field consists of contributions from a wide range of length scales. For conceptual purposes, it is common to refer to motions at different length scales in terms of characteristic "eddies", i.e. swirling motions, that denote the vortical nature of the flow over a given length scale. The concept of LES is based on the idea of trying to capture (or resolve) only the largest length scales (or eddies) of a particular turbulent flow, while at the same time modeling the effect of the smaller unresolved scales. Hence the name "large eddy simulation."

As explained by C. Hartel [29], the viability of the LES approach to modeling turbulent flow rests mainly on "two presumptions which appear plausible in view of both practical experience and theoretical considerations. The first of these is that most global features of turbulent flows, like average mixing rates or averaged losses, are governed by the dynamics of the largest scales and depend only little on the small-scale turbulence. From a practical point of view such global features are of primary interest and hence a reliable simulation of the largest scales will usually suffice. The other presumption is that the small-scale turbulence, especially at high Reynolds numbers, becomes independent of the strong inhomogeneities which are typical for the energy-containing eddies and thus tends to local isotropy. . . . It is reasonable to suppose that in this case models for the small-scale turbulence can be much simpler than statistical turbulence models and will be more universally applicable, because statistical models have to account for the inhomogeneous eddies as well."

To obtain equations which formally represent the LES concepts in mathematical form requires one to begin with the continuity and Navier-Stokes equations, and then apply the concept of spatial filtering.

2.3 Spatial Filtering

Conceptually, spatial filtering is simply the idea of defining a weighted average over some finite spatial domain. Mathematically, we can define a generic filtered variable $\bar{\phi}$ as a function of its associated unfiltered variable ϕ as follows.

$$\bar{\phi}(\mathbf{x}, t) = \int_D \phi(\mathbf{x}, t) G(\mathbf{x} - \mathbf{z}, \Delta)\, d\mathbf{z}, \tag{2.3}$$

where G is a normalized filter kernel (or weighting function), D is the domain of the flow, and Δ is the filter width in each spatial direction. The shape and spatial extent of the filter kernel is a modeling choice. For example, if a box filter is chosen, then the value of $\bar{\phi}$ is the instantaneous average value of ϕ within the domain enclosed by a box of dimension Δ. Other common filter types used in LES include the Gaussian filter and the sharp spectral filter. Pope [61], Sagaut [66] and many others provide simple figures which illustrate the shape of these filters both in physical space and in wavenumber space.

It is also useful to define a related variable ϕ' as the instantaneous difference between ϕ and $\bar{\phi}$, such that

$$\phi = \bar{\phi} + \phi' \tag{2.4}$$

and we add as a reminder that although not explicitly indicated, all of these values are, in general, functions of $\mathbf{x}$ and t.

Finally, it is important to note that contrary to traditional Reynolds averaging, spatially filtered variables have the following properties

$$\overline{\bar{\phi}} \neq \bar{\phi} \tag{2.5}$$

and

$$\overline{\phi'} \neq 0. \tag{2.6}$$

2.4 The Spatially Filtered Equations

There are several ways to derive LES equations of motion. The most common approach (what might be termed the "classic" approach) begins by requiring that the filtering operation commute with differentiation (which Pope [61] notes is true for all homogeneous filters). Under this constraint, one can simply apply the filtering operation to the continuity and Navier-Stokes equations directly, term by term. Denoting filtered quantities with an overbar, this yields the following LES equations for an incompressible fluid with constant properties:

$$\rho\frac{\partial \bar{u}_i}{\partial t} + \rho\frac{\partial}{\partial x_j}(\overline{u_i u_j}) = -\frac{\partial \bar{p}}{\partial x_i} + \frac{\partial}{\partial x_j}\left[\mu\left(\frac{\partial \bar{u}_i}{\partial x_j}\right)\right] + \rho\bar{f}_i \tag{2.7}$$

$$\frac{\partial \bar{u}_i}{\partial x_i} = 0. \tag{2.8}$$

Of particular interest is the nonlinear advection term (the second term) in Eq. (2.7). This is the term which requires closure, and thus where an LES subgrid model must be defined and applied in order to solve these equations. Example closure models are reviewed shortly. Although Eqs. (2.7) and (2.8) are often considered the basic LES equations of motion, it is important to recognize that because exact solutions of these equations are not possible, and if solutions are to be obtained, one cannot avoid the further step of choosing and implementing a numerical discretization scheme (e.g., finite difference, control volume, finite element, etc.) in order to define a set of discrete LES equations that can be solved on a finite grid. Thus the real LES equations are always a discrete form of Eqs. (2.7) and (2.8) coupled with a particular closure model.

An alternative way to develop a set of discrete LES equations is described by Schumann [67]. In this approach, called the 'volume-balance method,' the averaged quantities correspond to a discrete number of volumes that are fixed in space (i.e., the mesh). In essence,

it is simply a control-volume numerical scheme developed for LES. The governing equations are integrated by parts to obtain discrete budget equations for the individual mesh cells. The modeling problem then reduces to how to represent accurately the unresolved surface fluxes in terms of the spatially averaged quantities that are available. An advantage of this method is that irregular or anisotropic meshes do not introduce fundamental errors. (For the classic approach with non-uniform meshes, filter commutativity becomes a problem [66].) Adopting Schumann's notation, the discrete momentum equation that would correspond to Eq. (2.7) above can be written as

$$\rho\frac{\partial\bar{u}_i}{\partial t} + \rho\delta_j(\overline{u_i u_j}^S) = -\delta_i\bar{p} + \delta_j\left[\mu\left(\overline{\frac{\partial u_i}{\partial x_j}}^S\right)\right] + \rho\bar{f}_i, \tag{2.9}$$

where δ denotes a numerical-difference operator, and the advective and diffusive flux terms (denoted by superscript S) are averages over surfaces, not volume averages.

2.5 An Introduction to Closure Models

As noted above, the LES closure problem centers around how to model the nonlinear advection term, i.e. the second term in Eq. (2.7). In the literature, this is usually done by first defining a subgrid-scale stress tensor (often denoted as τ_{ij}, as it will be here), and then casting the closure problem as one of modeling τ_{ij} in terms of the filtered velocities $\bar{u}_i$. However, the actual definition of τ_{ij} is not always the same, and so the reader is cautioned to be careful in distinguishing these differences when considering different LES models.

There are two related, but somewhat distinct approaches that are commonly used to define τ_{ij}. In the first approach τ_{ij} is simply defined as the difference between the true filtered nonlinear advection term $\overline{u_i u_j}$, and the filtered-velocity advection term $\bar{u}_i\bar{u}_j$, as

$$\tau_{ij} = \overline{u_i u_j} - \bar{u}_i\bar{u}_j. \tag{2.10}$$

With this definition, Eq. (2.7) can be rewritten as

$$\rho\frac{\partial\bar{u}_i}{\partial t} + \rho\frac{\partial}{\partial x_j}(\bar{u}_i\bar{u}_j) = -\frac{\partial\bar{p}}{\partial x_i} + \frac{\partial}{\partial x_j}\left[\mu\left(\frac{\partial\bar{u}_i}{\partial x_j}\right)\right] - \frac{\partial}{\partial x_j}\tau_{ij} \tag{2.11}$$

where body-forces have been neglected for simplicity.

A second definition for τ_{ij} is described only after first applying the decomposition of Eq. (2.4) to $\overline{u_i u_j}$, and then expanding.

$$\overline{u_i u_j} = \overline{(\bar{u}_i + u_i')(\bar{u}_j + u_j')} = (\overline{\bar{u}_i\bar{u}_j} + \overline{\bar{u}_i u_j'} + \overline{u_i'\bar{u}_j}) + \overline{u_i' u_j'}) \tag{2.12}$$

From these it is customary to define a 'Leonard stress tensor' L_{ij}, a 'Cross stress tensor' C_{ij}, and a 'SGS Reynolds stress tensor' R_{ij} as follows.

$$L_{ij} = \overline{\bar{u}_i \bar{u}_j} - \bar{u}_i \bar{u}_j \tag{2.13}$$

$$C_{ij} = \overline{\bar{u}_i u'_j} + \overline{u'_i \bar{u}_j)} \tag{2.14}$$

$$R_{ij} = \overline{u'_i u'_j} \tag{2.15}$$

An important point discussed by Speziale [73] is that L_{ij} and C_{ij} individually are not Galilean invarient which is an intrinsic property of the Navier-Stokes equations (although $L_{ij} + C_{ij}$ are). With these definitions the nonlinear advection term can now be expressed as

$$\overline{u_i u_j} = \bar{u}_i \bar{u}_j + L_{ij} + C_{ij} + R_{ij} \tag{2.16}$$

One can now see that what remains to be modeled are C_{ij} and R_{ij}, since each of the other terms can be computed explicitly. Thus, when applying the above decomposition and definitions, it is customary to define the sub-grid stress tensor as only associated with the portion that must be modeled, i.e.,

$$\tau_{ij} = C_{ij} + R_{ij} = (\overline{\bar{u}_i u'_j} + \overline{u'_i \bar{u}_j)) + \overline{u'_i u'_j} \tag{2.17}$$

which, when combined with Eq. (2.7), allows one to write

$$\rho \frac{\partial \bar{u}_i}{\partial t} + \rho \frac{\partial}{\partial x_j}(\bar{u}_i \bar{u}_j) = -\frac{\partial \bar{p}}{\partial x_i} + \frac{\partial}{\partial x_j}\left[\mu\left(\frac{\partial \bar{u}_i}{\partial x_j}\right)\right] - \frac{\partial}{\partial x_j} L_{ij} - \frac{\partial}{\partial x_j}\tau_{ij} \tag{2.18}$$

where the body-force term has again been dropped for simplicity. Comparing Eq. (2.18) with Eq. (2.11) one can see that the only difference is that the Leonard stress tensor L_{ij}, which can be modeled, has been pulled out explicitly in Eq. (2.18). In either case, what remains to be modeled is the sub-grid stress tensor (which ever way it is defined).

One final note that may be helpful to the reader. The subgrid stress tensor can be partitioned into an isotropic part (written as $\frac{1}{3}\delta_{ij}\tau_{kk}$) and an anisotropic part (written as $\tau_{ij} - \frac{1}{3}\delta_{ij}\tau_{kk}$). Because the isotropic part of the stress can be absorbed in the pressure, some authors define the subgrid stress tensor as only the anisotropic part of the SGS stress, so as to simplify some of the modeling equations that will follow. The reader is simply cautioned to be cognizant of these subtle differences so as to avoid any confusion that may arise when reading the literature on this subject.

Currently, almost all commonly-used LES subgrid models can be classified as either a "gradient diffusion" type model, a "scale similarity" based model, or some combination of the two, called a "mixed" model. These are specific examples of what Sagaut [66] more generally

classifies as "functional modeling" and "structural modeling," and the reader is referred to Chapters 3-6 of [66] for a more detailed discussion of LES subgrid closure modeling than the brief introduction that will follow here.

2.5.1 Gradient-Diffusion Closure

Gradient-diffusion models adopt the following hypothesis, which consists of assuming that the anisotropic part of the subgrid-scale stress tensor τ is proportional to the resolved (large scale) strain-rate tensor $\mathbf{S}$:

$$\tau_{ij} - \frac{1}{3}\delta_{ij}\tau_{kk} = -2\mu_S \bar{\mathbf{S}}_{ij} \tag{2.19}$$

$$\bar{\mathbf{S}}_{ij} = \frac{1}{2}\left(\frac{\partial \bar{u}_i}{\partial x_j} + \frac{\partial \bar{u}_j}{\partial x_i}\right), \tag{2.20}$$

where μ_S is a subgrid eddy viscosity, which must be computed from an appropriate model, and δ_{ij} is the Kronecker delta. By defining a modified pressure $\bar{P}$ that includes the isotropic part of τ_{ij} (i.e. $\frac{1}{3}\delta_{ij}\tau_{kk}$, which is the trace of τ, and which also defines the subgrid kinetic energy) and performing the appropriate algebraic substitutions and manipulations (for detail see for example ref. [11]), Eq. (2.11) can be expressed as

$$\rho\frac{\partial \bar{u}_i}{\partial t} + \rho\frac{\partial}{\partial x_j}(\bar{u}_i\bar{u}_j) = -\frac{\partial \bar{P}}{\partial x_i} + \frac{\partial}{\partial x_j}\left[(\mu + \mu_S)\left(\frac{\partial \bar{u}_i}{\partial x_j}\right)\right]. \tag{2.21}$$

Thus under these assumptions the modeling problem finally reduces to the question of how to compute the subgrid eddy viscosity as a function of other known quantities.

2.5.1.1 Smagorinsky

The first model to appear in the literature for the subgrid eddy viscosity was introduced by Smagorinsky (1963) and it remains, together with its variants, a widely applied model today. It can be written compactly as

$$\mu_S = \rho(C_S\Delta)^2(2\bar{\mathbf{S}}_{ij}\bar{\mathbf{S}}_{ij})^{1/2} \tag{2.22}$$

where C_S is called the Smagorinsky constant, and the characteristic filter width Δ is generally computed as the cube root of the local cell volume:

$$\Delta = (\Delta x_1 \Delta x_2 \Delta x_3)^{1/3}. \tag{2.23}$$

Substitution of Eq. (2.22) into Eq. (2.19) yields

$$\tau_{ij} - \frac{1}{3}\delta_{ij}\tau_{kk} = -2\rho(C_S\Delta)^2|\bar{\mathbf{S}}|\,\bar{\mathbf{S}}_{ij} \tag{2.24}$$

where $|\bar{\mathbf{S}}| = (2\bar{\mathbf{S}}_{ij}\bar{\mathbf{S}}_{ij})^{1/2}$.

2.5.1.2 Ksgs Simple eddy viscosity models, such as the Smagorinsky model, implicitly assume that energy production and dissipation are in instantaneous local equilibrium. However, this is not a necessary requirement of the gradient diffusion hypothesis. The so called Ksgs (short for subgrid scale kinetic energy) model is one successful model that has been designed to overcome this limitation.

To describe this model we begin by defining the subgrid kinetic energy k^{sgs} as the trace of the subgrid-scale stress tensor, τ_{ij}, i.e.

$$k^{sgs} \equiv \frac{1}{2}\tau_{kk}^{sgs} = \frac{1}{2}(\overline{u_k u_k} - \bar{u}_k \bar{u}_k). \tag{2.25}$$

An exact subgrid kinetic energy equation is obtained by a procedure that is similar to the procedure used in RANS modeling to obtain what is called the turbulent kinetic energy equation (the equation that is used as part of the well known $k-\varepsilon$ RANS model). Skipping the derivation we can write an "exact" subgrid kinetic energy equation in the following form.

$$\begin{aligned} &\frac{\partial k^{sgs}}{\partial t} + \bar{u}_i \frac{\partial k^{sgs}}{\partial x_i} + \tau_{ij}^{sgs}\frac{\partial \bar{u}_i}{\partial x_i} + [\overline{\frac{\partial u_i}{\partial x_j}\frac{\partial u_i}{\partial x_j}} - \frac{\partial \bar{u}_i}{\partial x_j}\frac{\partial \bar{u}_i}{\partial x_j}] \\ &= \nu \frac{\partial}{\partial x_j}\frac{\partial k^{sgs}}{\partial x_j} - \frac{\partial}{\partial x_j}[\overline{u_i p} - \bar{u}_i \bar{p}] - \frac{\partial}{\partial x_j}[\overline{u_i k} - \bar{u}_i \bar{k}] + \frac{\partial}{\partial x_j}\bar{u}_i \tau_{ij}^{sgs}. \end{aligned} \tag{2.26}$$

As can be seen, this equation contains several unclosed terms that must be modeled. A model equation for the subgrid kinetic energy was first proposed by Schumann [67], and can be written as follows:

$$\frac{\partial k^{sgs}}{\partial t} + \frac{\partial}{\partial x_i}(\tilde{u}_i k^{sgs}) = P^{sgs} - D^{sgs} + \frac{\partial}{\partial x_i}(\nu_T \frac{\partial k^{sgs}}{\partial x_i}). \tag{2.27}$$

where $P^{sgs} = -C_k \tau_{ij}^{sgs} \partial \bar{u}_i / \partial x_j$ is the production of subgrid kinetic energy, $D^{sgs} = C_\varepsilon (k^{sgs})^{3/2}/\bar{\Delta}$, represents the dissipation, and the eddy viscosity is determined from k^{sgs} as

$$\nu_T = C_\nu \bar{\Delta}(k^{sgs})^{1/2}. \tag{2.28}$$

In this model three constants must be prescribed, $C_\nu, C_k, C_\varepsilon$ (although typically the value of C_k is set equal to unity), and the effective model for the subgrid stresses becomes

$$\tau_{ij}^{sgs} = -2\nu_T \bar{S}_{ij} + \frac{1}{3}\delta_{ij}\tau_{kk}^{sgs} \tag{2.29}$$

where we remind the reader that $\tau_{kk}^{sgs} = 2k^{sgs}$.

Though this is an eddy viscosity model just as the Smagorinsky model is, no assumption about the equivalence of production and dissipation are made and therefore nonequilibrium effects are accounted for in this model.

2.5.1.3 Dynamic Smagorinsky A method for dynamically adjusting the Smagorinsky constant to the local features of the flow was first suggested by Germano *et al.* [24]. The basic

idea is to assume that the constant in the eddy-viscosity relationship is the same for a second filter of larger width $\widetilde{\Delta}$. Given this second filter, typically referred to as the test filter, we can define a second subgrid-scale stress tensor $\mathbf{T}_{ij}$ as follows,

$$\mathbf{T}_{ij} = \widetilde{\overline{u_i u_j}} - \tilde{\bar{u}}_i \tilde{\bar{u}}_j. \tag{2.30}$$

Tilde denotes the test filter, here applied to quantities that have already been subject to a filter of width Δ. We now note that the difference between this tensor $\mathbf{T}$ and the filtered value of τ (using the test filter) can be written in terms of quantities that can be computed, i.e.,

$$\mathbf{L}_{ij} = \mathbf{T}_{ij} - \tilde{\tau}_{ij} = \widetilde{\overline{u_i}\overline{u}_j} - \tilde{\bar{u}}_i \tilde{\bar{u}}_j. \tag{2.31}$$

If we apply the assumption that the Smagorinsky constant is the same at both filter widths, then we can write

$$\widetilde{\overline{u_i}\overline{u}_j} - \tilde{\bar{u}}_i \tilde{\bar{u}}_j = 2\rho(C_S\widetilde{\Delta})^2 |\tilde{\bar{\mathbf{S}}}|\, \tilde{\bar{\mathbf{S}}}_{ij} - 2\rho\widetilde{(C_S\Delta)^2}|\bar{\mathbf{S}}|\, \bar{\mathbf{S}}_{ij}, \tag{2.32}$$

where the wide tilde over the rightmost term indicates test filtering of the entire term. This is an overdetermined but closed system of equations for the Smagorinsky constant C_S. The most common method of dealing with the overdeterminancy is to use the least-squares solution described by Lilly [44]. However, the fact that C_S appears inside the filtering operation (second term on the right-hand side of Eq. (2.32)) introduces some additional mathematical and practical problems for which various solutions have been proposed. These are discussed by Ghosal *et al.* [26], and a dynamic localization procedure is proposed which uses a constrained variational formulation.

For flows with two homogeneous directions, such as fully developed turbulent flow between parallel plates, the following formula is obtained:

$$(C_S(y,t))^2 = \left[\frac{\langle \mathbf{m}_{ij}\mathbf{L}_{ij}\rangle_{xz}}{\langle \mathbf{m}_{kl}\mathbf{m}_{kl}\rangle_{xz}} \right]_+, \tag{2.33}$$

where $\mathbf{m}_{ij} = 2\rho(wt\Delta)^2 |\tilde{\bar{\mathbf{S}}}|\, \tilde{\bar{\mathbf{S}}}_{ij} - 2\rho\widetilde{(\Delta)^2}|\bar{\mathbf{S}}|\, \bar{\mathbf{S}}_{ij}$, $\langle\rangle_{xz}$ denotes averaging over a layer of finite thickness in the xz plane, and the brackets with a + subscript denote the operation of taking the positive part, i.e., $[x]_+ = \frac{1}{2}(x + |x|)$ for any real number x.

2.5.1.4 Dynamic Ksgs This model was first proposed by Kim and Menon [40] and later extended to compressible flows by Nelson [56]. The test-scale level resolved turbulent kinetic energy is defined as

$$k^{test} = \frac{1}{2}(\widehat{\overline{u_k}\overline{u}_k} - \hat{\bar{u}}_k \hat{\bar{u}}_k) = L_{kk}/2 \tag{2.34}$$

where here we denote the second filter with a "hat" symbol $\hat{}$. Scale similarity between L_{ij} and τ^{sgs} is assumed. Evidence of this scale similarity was obtained by Liu et al. [45] in the

fully developed region of a circular jet. The resolved dissipation, denoted "e", is

$$e = (\nu + \nu_T) \left(\widehat{\overline{\frac{\partial u_i}{\partial x_j} \frac{\partial u_i}{\partial x_j}}} - \frac{\partial \hat{\bar{u}}_i}{\partial x_j} \frac{\partial \hat{\bar{u}}_i}{\partial x_j} \right) \tag{2.35}$$

At the subgrid scale level the subgrid stress tensor is modeled as

$$\tau_{ij}^{sgs} = -2C_\nu \Delta (k^{sgs})^{1/2} \bar{S}_{ij} + \frac{1}{3} \delta_{ij} \tau_{kk} \tag{2.36}$$

and at the test scale level L_{ij} is modeled as

$$L_{ij} = -2C_\nu \hat{\Delta} (k^{test})^{1/2} \hat{\bar{S}}_{ij} + \frac{1}{3} \delta_{ij} L_{kk} \tag{2.37}$$

These two expressions contain just one unknown, C_ν and so the least squares procedure is employed to solve this over determined system for the coefficient C_ν,

$$C_\nu = \frac{L_{ij} \sigma_{ij}}{\sigma_{ij} \sigma_{ij}} \tag{2.38}$$

where

$$\sigma_{ij} = -\hat{\Delta} (k^{test})^{1/2} \hat{\bar{S}}_{ij}. \tag{2.39}$$

One point worth mentioning is that C_ν no longer exists inside the filtering operation and so Eq. (2.38) is now consistent. Thus there is no need for ensemble averaging, and the model coefficients are truly localized. The dissipation model coefficient C_ε is obtained through

$$e = C_\varepsilon \frac{(k^{test})^{3/2}}{\hat{\Delta}} \tag{2.40}$$

and, finally,

$$C_\varepsilon = (\nu + \nu_T) \hat{\Delta} \left(\widehat{\overline{\frac{\partial u_i}{\partial x_j} \frac{\partial u_i}{\partial x_j}}} - \frac{\partial \hat{\bar{u}}_i}{\partial x_j} \frac{\partial \hat{\bar{u}}_i}{\partial x_j} \right) / (k^{test})^{3/2} \tag{2.41}$$

2.5.2 Scale Similarity Based Closure

The conceptual idea behind scale similarity based closure models is the notion that the behavior of the smallest resolved scales of motion can be used to approximate the behavior of the un-resolved scales. As proposed by Bardina *et al.* [3, 4] and articulated by Sagaut [66], this method is based on the hypothesis that "the statistical structure of the tensors constructed on the basis of the subgrid scales is similar to that of their equivalents evaluated on the basis of the smallest resolved scales."(cf. [66], pg. 177)

Variations on this general theme have led to a variety of models (e.g. [45],[30]). Here we provide a brief description of how Bardina's original model, which leads to the following approximation (see Eq. (2.7) above)

$$\tau_{ij} = \overline{u_i u_j} - \bar{u}_i \bar{u}_j \approx \overline{\bar{u}_i \bar{u}_j} - \bar{\bar{u}}_i \bar{\bar{u}}_j \tag{2.42}$$

can be derived.

We begin by applying the decomposition of Eq. (2.4) to the Cross stress (Eq. (2.14)) and SGS Reynolds stress (Eq. (2.15)) tensors, and then make the following approximations:

$$C_{ij} = \overline{\bar{u}_i(u_j - \bar{u}_j)} + \overline{\bar{u}_j(u_i - \bar{u}_i)} \approx \bar{\bar{u}}_i(\bar{u}_j - \bar{\bar{u}}_j) + \bar{\bar{u}}_j(\bar{u}_i - \bar{\bar{u}}_i) \tag{2.43}$$

and

$$R_{ij} = \overline{(u_i - \bar{u}_i)(u_j - \bar{u}_j)} \approx (\bar{u}_i - \bar{\bar{u}}_i)(\bar{u}_j - \bar{\bar{u}}_j). \tag{2.44}$$

When these two approximations are added, several terms can be subtracted out, yielding

$$C_{ij} + R_{ij} \approx \bar{u}_i\bar{u}_j - \bar{\bar{u}}_i\bar{\bar{u}}_j. \tag{2.45}$$

When these are added to the Leonard stress tensor (Eq. (2.13), we can finally write

$$\tau_{ij} = L_{ij} + C_{ij} + R_{ij} \approx \overline{\bar{u}_i\bar{u}_j} - \bar{\bar{u}}_i\bar{\bar{u}}_j. \tag{2.46}$$

2.5.3 Mixed Models

An advantage of the scale similarity models is that energy transfer between large (resolved) scales and small (modeled) scales is bi-directional, providing a mechanism for modeling "backscatter" — i.e. the backward flux of energy that occurs intermittently during real turbulent flows. Unfortunately, scale similarity models by themselves do not adequately dissipate the energy from the resolved scales. In other words, the model does not ensure a net energy transfer to the small scales, which can lead to an unphysical build-up of energy in the resolved scales. This problem has motivated researchers to try combining scale similarity models with gradient diffusion (eddy viscosity) models to ensure the proper dissipation of energy. These models are now commonly called "mixed models", and can be written in the following general form;

$$\tau_{ij} - \frac{1}{3}\delta_{ij}\tau_{kk} = -2\mu_S\bar{\mathbf{S}}_{ij} + (\mathcal{L}_{ij} - \frac{1}{3}\delta_{ij}\mathcal{L}_{kk}) \tag{2.47}$$

where the subgrid eddy viscosity is found from a gradient diffusion model and the tensor $\mathcal{L}_{ij}$ is evaluated using a scale similarity model.

For example, the mixed "Smagorinsky-Bardina model" [4] is obtained when using Equation (2.22) for the eddy viscosity, and defining the tensor $\mathcal{L}_{ij}$ as per Equation (2.46), i.e.

$$\mathcal{L}_{ij} = L_{ij} + C_{ij} + R_{ij} = \overline{\bar{u}_i\bar{u}_j} - \bar{\bar{u}}_i\bar{\bar{u}}_j. \tag{2.48}$$

Other examples of mixed models are summarized in reference [66].

2.5.4 Comments on Closure Models and Effective Filtering

Based on the methodology used to develop the LES equations, one is naturally inclined to think of developing an LES model in the following sequential manner:

(1) choose a particular filter (e.g. box or gaussian filter),

(2) apply the filter to the NS equations, and

(3) develop or choose a subgrid closure model.

However, in some respects this is probably **not** the best way to view the process. Since the LES equations are valid for any homogeneous filter, in fact, it is the subgrid model which defines the effective filter (assuming the solution is numerically well resolved). For example, it can be shown that a Smagorinsky model corresponds to the application of a smooth (in spectral space) filter that is "gaussian-like" in shape (see [66] and [1]).

An interesting way to better understand this issue is presented by Sagaut ([66] pg. 207), who reinterprets the LES equations as exact equations describing a "non-Newtonian fluid of the generalized Newtonian type," which he calls a "Smagorinsky fluid" when a Smagorinsky model is applied.

This illustrates one of the important complexities of LES which must be clearly understood in order to understand and interpret any results obtained. Unfortunately, the issue of effective filters in LES is further complicated by a host of numerical issues, which will be briefly discussed later in Section 2.7.

2.6 Statistical Analysis of Turbulent Flows

An important characteristic of the velocity field in turbulent flows is its "random" nature (here we use the term random as defined by Pope [61]), and thus the statistical description of turbulent flows has become a fundamental aspect of turbulence simulation and analysis. Probably the most important statistical quantities of interest (and the most physically revealing) are the mean values of the flow variables, some times referred to as moments. The first two moments are called the mean and the variance. These moments are routinely measured in experiments and form the basis of the RANS solution approach for turbulent flows. There are several techniques used to obtain these moments from raw data. To present these techniques first requires a few definitions.

A stationary flow is one in which the mean values are independent of the initial time from which the means are determined. Stationary flows are also referred to as statistically steady. In other words, the mean values do not change with time. An example of a stationary flow is a jet flow issuing from the nozzle of a pipe at high Reynolds number with a constant mass flow rate. After some time, the flow settles down and a stationary flow is achieved. A probe designed to measure the velocity field placed at some location within the jet would measure a fluctuating velocity that if examined closely would seem to be oscillating randomly about

a steady mean.

An example of a non-stationary or transient flow is the flow in the same jet at start-up. Just after the flow from the pipe escapes the pipe nozzle for the first time, the jet issues into a quite medium and the flow structures are quite different than those observed at a later time after the flow has settled down. If one is interested in the mean values of these transient dynamics, they could be measured by repeating the start-up many times and accumulating the flow data for variables of interest at the desired location and the same time elapsed from the start. This is an example of ensemble averaging; repeating the experiment over and over until the mean values are independent of the number of experiments performed. At this point the mean values are said to have converged.

A homogeneous flow is one in which the properties of the flow do not vary with spatial location. Since the statistics of the flow do not vary with spatial location, all mean quantities for the flow are independent of location. If in addition, the flow is isotropic then the properties of the flow do not vary with direction. In other words, the flow is invariant to a rotation in coordinate system. Homogeneous flow is an idealization because boundary conditions such as walls introduce inhomogeneities to the flow. The best example of homogeneous flow is the flow behind a mesh in a wind tunnel. In the central region away from the tunnel walls, the flow approaches homogeneous and isotropic conditions. Even in this case the turbulent kinetic energy decays in the streamwise direction slowly so that the region of homogeneous isotropic flow is confined to a small streamwise distance in the central region of the tunnel.

For incompressible flow, the turbulence is entirely determined from the velocity and pressure fields in the domain of interest at an instant in time. We define a realization of turbulence as being the entire velocity and pressure fields at an instant of time. The fields at a later instant would represent a different realization. Now if the flow is homogeneous the mean values could be obtained from a single realization of the flow instead of averaging at a single point in space over a long duration as was discussed earlier. The two techniques for measuring mean values are expected to be equivalent in a homogeneous flow.

At this point three techniques for determining mean values of turbulence have been described. Reynolds averaging describes the time invariant mean quantities of a stationary flow as a function of position. Spatial averaging describes the spatial invariance of mean values in a homogeneous flow that may or may not be stationary. Ensemble averaging is well suited for transient flows and describes the mean values as a function of both space and time.

The fourth technique for determining mean values is through the use of probability densities of stationary processes. If the probability density of the flow variables is known for the entire domain of interest, then all of the moments of the flow properties can be obtained from the probability density. In practice, this probability density is difficult to determine and contains more information than is desired. There are examples of where the probability density is symmetric about its mean and an approximate normal distribution can be assumed. In

this case all the moments of the flow can be determined from the first two moments.

This section summarizes the equations used to define statistical averages and quantities relevant to the analysis of turbulent flows and quantities that facilitate the evaluation of turbulent flow simulations. A more comprehensive presentation may be found in [61].

2.6.1 Mean and Fluctuating Quantities

Consider the temporally and spatially varying quantity $\phi(x_i, t)$. Its Reynolds time average is defined as

$$< \phi(x_i) >= \lim_{\Delta T \to \infty} \frac{1}{\Delta T} \int_{t_o}^{t_o + \Delta T} \phi(x_i, t')dt'. \tag{2.49}$$

The variable $\phi(x_i, t)$ is said to be stationary if its mean values are independent of the starting time t_o. In this case, the mean values of $\phi(x_i, t)$ are independent of time altogether.

With this definition any variable can be decomposed into its mean and fluctuating component as follows;

$$\phi(x_i, t) =< \phi(x_i) > +\phi'(x_i, t) \tag{2.50}$$

and obeys the following Reynolds averaging rules,

$$< \phi' > = 0 \tag{2.51}$$

$$<< \phi >> = < \phi > \tag{2.52}$$

$$< \phi\psi > = < \phi >< \psi > + < \phi'\psi' > \tag{2.53}$$

$$< \phi' < \psi >> = < \psi' < \phi >>= 0. \tag{2.54}$$

In practice, time averages are approximated by the discrete summation,

$$< \phi(x_i) >= \lim_{N \to \infty} \frac{\sum_{n=1}^{N} \phi_n(x_i, t_n)\Delta t_n}{\sum_{n=1}^{N} \Delta t_n} \tag{2.55}$$

where Δt_n is the time step increment for the nth time integration step and $t_n = \sum_{m=1}^{n} \Delta t_m$.

Let ϕ represent a scalar quantity and let u_i, $(i = 1, 2, 3)$ represent the ith Cartesian component of the instantaneous velocity field. The variance of a scalar is obtained by

$$\sigma =< (\phi - < \phi >)^2 >=< \phi^2 > - < \phi >^2 \tag{2.56}$$

and the root mean square (r.m.s.) by $\sigma^{1/2}$. Similarly, the Reynolds stress tensor is obtained by

$$R_{ij} =< u_i' u_j' >=< u_i u_j > - < u_i >< u_j > \tag{2.57}$$

and the turbulent kinetic energy is simply

$$k' = \frac{1}{2} < u_k' u_k' >= \frac{1}{2}(< u_k u_k > - < u_k >< u_k >). \tag{2.58}$$

The turbulent scalar flux vector is

$$< \phi' u_i' >=< \phi u_i > - < \phi >< u_i > . \tag{2.59}$$

The triple correlation between three independent scalars is obtained by

$$< \phi'\psi'\lambda' >=< \phi\psi\lambda > - < \phi >< \psi >< \lambda > \tag{2.60}$$
$$-(< \phi >< \psi'\lambda' > + < \psi >< \phi'\lambda' > + < \lambda >< \phi'\psi' >).$$

2.6.2 Higher Order Statistics

Higher-order moments of velocity differences and velocity derivatives have been used to analyze isotropic turbulence. For homogeneous isotropic turbulence with zero mean velocity, the velocity fluctuations have a Gaussian probability distribution. Since this distribution is symmetric, odd moments are all equal to zero. The nonzero moment higher than the variance is the flatness which obtains a value of roughly 3.0. The equations for skewness and flatness are (no summation of indices);

$$S_{i,0} = \frac{\langle u_i^3 \rangle}{\langle u_i^2 \rangle^{3/2}} \tag{2.61}$$

$$F_{i,0} = \frac{\langle u_i^4 \rangle}{\langle u_i^2 \rangle^2}. \tag{2.62}$$

Derivative skewness and flatness are defined as

$$S_{i,1} = \frac{\left\langle \left(\frac{\partial u_i}{\partial x_i}\right)^3 \right\rangle}{\left\langle \left(\frac{\partial u_i}{\partial x_i}\right)^2 \right\rangle^{3/2}} \tag{2.63}$$

$$F_{i,1} = \frac{\left\langle \left(\frac{\partial u_i}{\partial x_i}\right)^4 \right\rangle}{\left\langle \left(\frac{\partial u_i}{\partial x_i}\right)^2 \right\rangle^2}. \tag{2.64}$$

Derivative skewness $\sim -0.3 - -0.5$ and flatness $\sim 3 - 4$ have been observed [5]. Analysis of derivative statistics reveal behaviors of the numerical scheme and subgrid models associated with the smallest resolved scales. Skewness and flatness of velocity differences have also been measured [5],

$$S_{i,\Delta} = \frac{\langle (\Delta u_i)^3 \rangle}{\langle (\Delta u_i)^2 \rangle^{3/2}} \tag{2.65}$$

$$F_{i,\Delta} = \frac{\langle (\Delta u_i)^4 \rangle}{\langle (\Delta u_i)^2 \rangle^2} \tag{2.66}$$

where $\Delta u_i = u_i(x_i + r_i, t) - u_i(x_i, t)$ and $r_i = x_i + r$.

2.6.3 Anisotropic Stress Tensor

An intrinsic distinction exists between isotropic and anisotropic stresses. The isotropic stress is $\frac{2}{3}k'\delta_{ij}$ and the deviatoric isotropic part is

$$a_{ij} =< u_i' u_j' > -\frac{2}{3}k'\delta_{ij}. \tag{2.67}$$

The normalized anisotropic tensor is defined as

$$b_{ij} = \frac{a_{ij}}{2k'} \tag{2.68}$$

where $k' = \frac{1}{2} < u_k' u_k' >$ is the turbulent kinetic energy. It is readily seen that for isotropic turbulence $a_{kk} = 0$.

2.6.4 Two-Point Correlations

The two-point one-time autocovariance of the fluctuating velocity is defined as

$$R_{ij}(r_i, x_i, t) =< u_i'(x_i, t) u_j'(x_i + r_i, t) > . \tag{2.69}$$

This is also referred to as a two-point correlation. From this, various integral length scales can be defined. In particular the longitudinal integral length scale is

$$L_{11} \equiv \frac{1}{R_{11}(0, x_i, t)} \int_0^\infty R_{11}(r_1, x_i, t) dr_1. \tag{2.70}$$

For homogeneous isotropic turbulence assuming periodic boundary conditions, two-point correlations are calculated and used to estimate the integral length scales L_{ii} which are the longitudinal integral length scales in the x_i directions respectively. These quantities are determined from

$$L_{11} = \frac{1}{\overline{u_1'^2}} \int_{-\infty}^{\infty} \overline{\left[u_1(x_1, x_2, x_3, t) - \overline{u_1(t)}\right] \left[u_1(x_1 + r, x_2, x_3, t) - \overline{u_1(t)}\right]} dr \tag{2.71}$$

where the over line denotes a spatial average over the entire domain and L_{ii} are functions of time. For isotropy $L_{11} \approx L_{22} \approx L_{33}$ and so $l_t = (L_{11} + L_{22} + L_{33})/3$. The transverse integral scale is estimated in a similar manner,

$$L_{12} = \frac{1}{\overline{u_1'^2}} \int_{-\infty}^{\infty} \overline{\left[u_1(x_1, x_2, x_3, t) - \overline{u_1(t)}\right] \left[u_1(x_1, x_2 + r, x_3, t) - \overline{u_1(t)}\right]} dr \tag{2.72}$$

In LES simulations, l_t can be used to calculate the turbulent Re_t, and the large-eddy turnover time τ_t. Assuming the flow is homogeneous and isotropic, L_{11}, L_{22} and L_{33} can be calculated at each grid cell and then averaged over all grid cells to obtain a single value for each direction.

For homogeneous turbulence, $R_{ij}(r_i,t)$ is independent of x_i and the spatial information contained in $R_{ij}(r_i,t)$ can be re-expressed in spectral space using Fourier transforms. The Fourier transform is,

$$\Phi_{ij}(k_i,t) = \frac{1}{(2\pi)^3}\int_{-\infty}^{\infty}\int_{-\infty}^{\infty}\int_{-\infty}^{\infty} e^{-ik_i r_i} R_{ij}(r_i,t)dr_1,dr_2,dr_3 \tag{2.73}$$

and the inverse transform is

$$R_{ij}(r_i,t) = \int_{-\infty}^{\infty}\int_{-\infty}^{\infty}\int_{-\infty}^{\infty} e^{ik_i r_i}\Phi_{ij}(k_i,t)dk_1dk_2dk_3. \tag{2.74}$$

Setting $r_i = 0$ yields the Reynolds stress tensor,

$$R_{ij}(0,t) =< u_i'u_j' >= \int_{-\infty}^{\infty}\int_{-\infty}^{\infty}\int_{-\infty}^{\infty}\Phi_{ij}(k_i,t)dk_1dk_2dk_3. \tag{2.75}$$

The turbulent kinetic energy as a function of the wave number amplitude is

$$E(k,t) = \int_{-\infty}^{\infty}\int_{-\infty}^{\infty}\int_{-\infty}^{\infty}\frac{1}{2}|\Phi_{ii}(k_i,t)|\delta(|k_i|-k)dk_1dk_2dk_3 \tag{2.76}$$

and its physical space representation is just

$$k' = \frac{1}{2} < u_i'u_i' >= \frac{1}{2}R_{ii}(0,t) = \int_0^{\infty} E(k,t)dk. \tag{2.77}$$

2.6.5 The One Dimensional Turbulent Energy Spectra

For spatially-evolving non-homogeneous flows it is appropriate to work in the frequency domain. If the flow is stationary and mean velocity field is constant and much larger than the velocity fluctuations (i.e. $< u >\gg u'$), Taylor's hypothesis may be used to relate the frequency content of the fluctuating signal to a length scale content,

$$< u_1'u_1' >= \int_0^{\infty} E_{11}(\omega)d\omega \tag{2.78}$$

and $E_{11}(k_1) =< u_1 > E_{11}(\omega)$.

In spatially-evolving flows where the flow is no longer homogeneous it is more convenient to estimate an integral length scale from the time history of a single velocity component at a point in the flow field. The length scales can be estimated from the single point auto-correlation function defined such as follows

$$R_{11}(\tau) = \frac{< u_1(x_i,t)u_1(x_i,t+\tau) >}{< u_1'^2 >}. \tag{2.79}$$

The Eulerian integral scale is then determined by

$$\mathcal{T}_{11} = \int_0^{\infty} R_{11}d\tau \tag{2.80}$$

and assuming Taylor's hypothesis is valid, $L_{11} \approx \mathcal{T}_{11} < u_1'^2 >^{1/2}$ [74].

2.6.6 Favre Averaged Statistics

Analysis of flows with significant fluctuations in density whether caused by compressibility or a rise in temperature are simplified by introducing the Favre (mass weighted) average as

$$\widetilde{\phi(x_i)} = \frac{\overline{\rho(x_i,t)\phi(x_i,t)}}{\overline{\rho(x_i)}} = \lim_{\Delta T\to\infty} \frac{1}{\Delta T \overline{\rho(x_i)}} \int_t^{t+\Delta T} \rho(x_i,t')\phi(x_i,t')dt'. \tag{2.81}$$

The instantaneous variables are decomposed into average and fluctuations

$$\phi(x_i,t) = \widetilde{\phi(x_i)} + \phi''(x_i,t). \tag{2.82}$$

Similar to the incompressible case, Favre-averages obey the following rules

$$\widetilde{\phi''} = 0 \tag{2.83}$$

$$\tilde{\tilde{\phi}} = \tilde{\phi} \tag{2.84}$$

$$\overline{\rho\phi''} = 0 \tag{2.85}$$

$$\bar{\tilde{\phi}} = \tilde{\phi} \tag{2.86}$$

$$\overline{\phi''} = \bar{\phi} - \tilde{\phi}. \tag{2.87}$$

The relationships between Reynolds-averaged and Favre-averaged quantities are

$$\tilde{\phi} = \bar{\phi} + \frac{\overline{\rho'\phi'}}{\bar{\rho}} = \bar{\phi} + \frac{\overline{\rho'\phi''}}{\bar{\rho}}. \tag{2.88}$$

In order calculate the Favre-averaged scalar flux of scalar c, $\overline{\rho u''c''}$, the following identity is used

$$\overline{\rho u''c''} = \overline{\rho}\widetilde{u''c''} = \overline{\rho uc} - \overline{\rho}\tilde{c}\tilde{u} \tag{2.89}$$

This is an important closure term in combustion modeling. The Reynolds-averaged expression becomes much more complicated due to the fluctuating density component

$$\overline{\rho}\overline{u'c'} = \overline{\rho uc} - \bar{\rho}\bar{u}\bar{c} - \overline{u}\overline{\rho'c'} - \overline{c}\overline{\rho'u'} - \overline{\rho'u'c'}. \tag{2.90}$$

2.7 A Brief Discussion of Numerical Issues

No analytical solutions to the continuum form of the LES equations for any problems of interest are known to the authors. All LES results are in fact solutions to some discrete numerical representation of Eqs. (2.7) and (2.8) (e.g., finite difference, control volume, finite element, etc.) on a specified mesh, coupled with a particular closure model. Thus all of the standard issues associated with numerical methods become intimately involved in any LES calculation.

Our purpose here is not to provide a comprehensive description of the problems, as this is entirely beyond the scope of this work. However, some introductory comments intended to acquaint the reader with some of the key issues is felt to be important to provide the proper context to the research and results described herein.

2.7.1 Mesh Refinement, Explicit "prefiltering", and Computational Cost

In discussing LES, it is useful to distinguish between the discretization length scale h, and the filter cutoff length scale Δ. If the ratio h/Δ is small, than the numerical error associated with the solution decreases approximately as $(\frac{h}{\Delta})^n$, where n is the order of the numerical method. Because of this relationship between these two scales, there are two different approaches to LES mesh refinement which can be pursued in order to obtain the "best" possible solution for a given problem when one has finite computational resources.

The first approach is to let $h = \Delta$, and simply refine the mesh as much as possible for a given problem. The rationale here is to resolve as much as possible on the mesh — thereby minimizing the subgrid contributions to the overall global dynamics. Of course, as shown above, under these conditions the numerical error at the smallest resolved scales is at its maximum and, as will be discussed below, has been shown to be quite large. This leads to serious questions about how valid the results are, or even how to interpret them. A rationale sometimes given for accepting this ambiguity is that even if the smallest resolved scales are poorly represented, they will (hopefully) contain only a small portion of the total kinetic energy, and thus relatively large errors in the subgrid stress model may be acceptable.

The second approach is to use some means to control and reduce the ratio $\frac{h}{\Delta}$. The most common method is usually called "prefiltering" or "explicit filtering". As explained by Lund [50], the key step in this approach is to use an alternative definition of τ_{ij} (see Eq. 2.10) as follows. Let

$$\tau_{ij} = \overline{u_i u_j} - \widetilde{\bar{u}_i}\widetilde{\bar{u}_j}. \tag{2.91}$$

where $\widetilde{()}$ denotes a discrete approximation to the primary filter, and where by implication, the nonlinear advection terms has been decomposed as

$$\overline{u_i u_j} = \widetilde{\bar{u}_i \bar{u}_j} + (\overline{u_i u_j} - \widetilde{\bar{u}_i \bar{u}_j}). \tag{2.92}$$

Lund demonstrates that filtering the nonlinear advection term in this way achieves an explicit filtering of the velocity field that limits the frequency content for all time to the discrete filter width.

Another method is effectively suggested by Mason *et al.* [52, 53] in the context of the Smagorinsky model and the interesting interpretation they give for the Smagorinsky constant C_s. They demonstrate that larger values of C_s correspond to indirectly imposing a filter of increasing larger length scale on the flow field.

In either case, if a sufficient separation between the mesh and the filter lengths is achieved, than a mesh independent solution can, in theory, be obtained for any consistent numerical method. Of course, the cutoff length scale must still be very small relative to the integral length scale of the turbulent flow so that the "large" eddies are being resolved by the LES.

Unfortunately, the cost of doing prefiltered LES on numerical grids sufficiently refined to assure full numerical convergence is usually prohibitive. The cost of mesh refinement in LES can be illustrated by considering an LES of fixed filter width Δ, and constant grid spacing h. Because the number of nodes in each direction, as well as the time step (due to CFL accuracy and stability factors) each scale approximately as h^{-1}, the computational cost can be thought of as roughly proportional to $(h/\Delta)^{-4}$. Thus cutting the mesh size h in half increases the computational cost by a factor of approximately 16!

Because of this enormous computational cost penalty for mesh refinement, practitioners almost always seek to strike a balance between accepting some degree of error, so as to afford the calculations, while at the same time controlling its magnitude, so that the solution remains meaningful. How best to achieve this balance remains a topic of great interest and much current research.

2.7.2 Numerical Error and LES Closure

Since all numerical methods introduce errors, it is important to understand the nature of the different kinds of approximation errors that are introduced and how they can affect an LES. Three different types of numerical error, and how they impact the effective LES model are briefly discussed next.

Dissipation error. Numerical dissipation acts to artificially (i.e. not due to physics) reduce gradients along the coordinate direction where the numerical differencing is being performed. As is discussed in most texts on numerical methods, it can be shown to be a direct result of the even derivative terms in the truncation error, and is associated with what is called numerical or artificial viscosity. It can also be thought of as a means of imposing a

one-dimensional filter in each coordinate direction.

When a subgrid model is used in LES but the mesh is not fine enough to resolve the velocity scales near the filter cutoff length-scale, then the effective subgrid model and its associated effective filter are in fact due to the combined effects of the specified model and the numerical dissipation. This introduces problems as to how to interpret the results. From a practical standpoint, this problem is usually addressed by attempting to determine how important the affected scales are to the overall solution. For example, if one can demonstrate that a large portion of the kinetic energy is contained within the scales that are well resolved (i.e. not polluted by the numerical errors) then even if the smaller scales are corrupted, the overall simulation should be valid. However, if a dynamic subgrid closure model is used that is based on using information from the smallest resolved scales (those most affected by the numerical errors), then the entire simulation can become suspect.

Because the effect of numerical dissipation has similarities to the eddy viscosity generated by a subgrid model, some authors have proposed and tested LES models based entirely on the artificial dissipation associated with specific numerical schemes (e.g. [58, 22, 23]). However, this approach is controversial because of the one-dimensional nature of the effective filters applied. Since each term in the Navier-Stokes equations is acted on by a distinctly different one-dimensional filter, the basic assumptions associated with deriving the LES equations are not satisfied, leading to ambiguities concerning the meaning of the results.

Finally, we note that dissipation errors are not confined to spatial difference operators only. Lower order time integration schemes can also contribute significantly to the numerical error introduced into an LES.

Dispersion error. Numerical dispersion acts to distort spatial and temporal phase relationships — which typically show up as "wiggles" near regions of under-resolved sharp gradients. Dispersion errors are a result of the odd derivative terms in the truncation error of a given approximation. Numerical dispersion is obviously undesirable in LES simulations as this would corrupt the turbulent fluctuations of the real flow.

Spectral aliasing error. When the nonlinear convective term in the LES equations (i.e. the 2nd term in Eq. (2.11)) is numerically computed in discrete physical space (as compared to Fourier space) of finite dimension, spurious high frequency information is generated which can corrupt the resolved frequency response. This error is called an aliasing error. As suggested by Sagaut [66], this error can be by illuminated by considering two discrete functions u and v represented by N degrees of freedom. At the point of subscript j, the expansions can be expressed as:

$$u_j = \sum_{n=-N/2}^{N/2-1} \hat{u}_n e^{(i(2\pi/N)jn)}, \qquad v_j = \sum_{m=-N/2}^{N/2-1} \hat{v}_m e^{(i(2\pi/N)jm)} \quad j = 1, N \quad . \tag{2.93}$$

The Fourier coefficient of the product $w_j = u_j v_j$ (no sum on j) separates into the form:

$$w_k = \sum_{n+m=k} \hat{u}_n \hat{v}_m + \sum_{n+m=k\pm N} \hat{u}_n \hat{v}_m \quad . \tag{2.94}$$

The last term on the right-hand side represents the spectrum aliasing error.

2.7.2.1 Discussion In an effort to better quantify the relative magnitude of the the error terms as compared to the SGS stress, Ghosal [25] performed a non-linear analysis of the numerical error for isotropic homogeneous turbulent flow where the energy spectrum was approximated by the Von Karman model. The numerical error was defined as the difference between a given numerical solution and an "optimum" discrete solution — defined as the solution obtained using a full spectral method. In the analysis, both the subgrid models and the time integration were assumed to be exact so as to clearly distinguish the numerical error.

The results of this analysis are somewhat discouraging in that they suggest that numerical discretization errors dominate the subgrid terms for mesh resolutions and numerical methods typically used. Only when using very high order numerical schemes and or a prefiltering technique (to decouple the filter cutoff length from the discretization length scale) does the SGS stress govern the solution dynamics. Ghosal's analysis is often quoted in the literature (e.g. [21]) and has stirred significant discussion because, in some ways, its results seem at odds with the experiences of many LES practitioners. In this context the following statement made by Sagaut concerning this analysis is useful as it probably typifies the current somewhat cautious view of the community with respect to these issues:

". . . It should be noted here that practical experience leads us to less pessimistic conclusions than the theoretical analyses: large eddy simulations performed with a scheme accurate to second order show a dependency with respect to the subgrid model used. The effects of these models are not entirely masked, which justifies using them. However, no precise qualifications exists today of the information loss due to the use of a given scheme. These observations are made empirically, case by case". ([66] pg. 218)

2.7.3 Comments on LES with Unstructured, Irregular Grids

Up to the present, most LES calculations have been performed on regular "structured" grids. There are both numerical and theoretical reasons why this is so. From a numerical standpoint, codes based on structured meshes can (more easily) be made computationally very efficient (i.e. they run fast), they are typically easier to write and debug, and high-order numerical schemes are available and well understood for these types of meshes. From a theoretical standpoint, unless special steps are taken, an irregular mesh implicitly imposes a non-uniform filter which does not commute with differentiation, and therefore invalidates the assumptions used in deriving the LES equations themselves.

Despite these challenges, in order to do LES of turbulent flows in complex 3-D geometries, the ability to use unstructured, irregular meshes may be unavoidable. As both the computational speed of computers and the desire to do such problems has increased (see [27]), a number of researchers have begun actively working in this area [75, 51]. Interestingly, an additional motivation for this work is the potential cost savings associated with adaptive mesh refinement, which for LES may be especially useful near walls [31]. We note that this work is of particular interest to the finite element community where improved methods for CFD and the use of unstructured grids has made possible the calculation of flows in very complex geometries with relative ease.

Later in this report, we discuss the implementation and testing of a variety of LES models into MPSalsa, a finite element code which is designed to use unstructured grids. In some applications described the actual grid used in the simulations will be a regular, uniform grid which could have been used with an structured-grid code. However, in some cases it is not. Thus an important aspect of the work described herein relates to the development of numerical implementations and LES utilities that can be used on irregular grids. Of particular note is the problem of discrete filtering, which is discussed next.

2.7.4 Discrete Filtering

As has been previously noted, a variety of LES models require a secondary filtering operation, which must be performed numerically on the resolved mesh. These include the dynamic LES models (Sec.s 2.5.1.3 and 2.5.1.4), scale similarity models (Sec. 2.5.2), any approach that explicitly models the Leonard stress terms (Eq. 2.13), and certain prefiltering techniques (Sec. 2.7.1). In each case we have the problem of numerically approximating the filtering (see Eq. 2.3) of a filtered quantity, i.e.

$$\tilde{\bar{\phi}}(\mathbf{x},t) = \int_D \bar{\phi}(\mathbf{x},t) G(\mathbf{x}-\mathbf{z},\tilde{\Delta})\, d\mathbf{z}, \tag{2.95}$$

where $\tilde{\Delta}$ denotes the filter width of the second filter.

Many well understood numerical techniques are available for doing numerical quadrature. However, in the context of LES we typically desire to evaluate this integral when $\tilde{\Delta}$ is approximately twice the value of Δ (the primary filter width), use only an absolute minimum number of quadrature points (to minimize cost), and assure that the discrete filter commutes with differentiation (at least to some known order). These constraints require careful consideration and lead to special challenges when the numerical mesh is irregular in shape and when the integral must be evaluated near boundaries.

Marsden *et al.* [51] provide a discussion of very recent work in this area. Here, we develop a different method that is based on reproducing kernel particle methods (RKPM). We also discuss our implementation of a lumped mass projection (LMP) technique for filtering that

has been used in the finite element LES literature [31].

2.7.4.1 Filtering based on Reproducing Kernel Particle Methods We begin by describing discrete filtering in the context of the multiple scale decompositions work of Lui *et al.* [47, 48, 46]. For simplicity, we begin the discussion with the simpler one-dimensional case (the formulation can be extended to multi-dimensions). In one dimension, the discrete filtering operation may be written as,

$$u^{2a}(x) = \sum_{i=1}^{Nnp} u^a(x_i) w_i^{2a}(x) \tag{2.96}$$

where $w_i^{2a}(x)$ is the filter (kernel) function centered at grid point i and evaluated at location x. The dilation parameter, $2a$, describes the width of (and hence scale represented by) the filter, Nnp is the number of filter functions, w_i^{2a}, which have x in their support, and u^{2a} is the filtered approximation to u^a at scale $2a$.

In general, it is necessary that the filtering operation described in Eq. (2.96) commute with the spatial differential operators of the Navier-Stokes equations for explicit filtering of these equations to be successful. Although it is not generally possible to reduce these commutative errors to zero, they can be controlled by enforcing "moment conditions" when generating the kernel functions. We consider a class of filters that satisfy the following moment conditions,

$$m_0(x) = 1 \tag{2.97}$$

$$m_k(x) = 0, k = 1, ..., n-1, \tag{2.98}$$

$$m_k(x) \neq 0, k \geq n. \tag{2.99}$$

imposed over the domain Ω. In Eq. (2.97)–(2.99), n is the order of the commutation error associated with filtering of the spatial first-derivative operator, and the moments are calculated as,

$$m_k(x) = \sum_{i=1}^{Nnp} (x - x_i)^k w_i^{2a}(x). \tag{2.100}$$

It remains to determine $w_i^{2a}(x)$ such that Eq. (2.97)– (2.98) are satisfied. Liu and co-workers have developed a methodology (the Reproducing Kernel Particle Method - RKPM) to generate kernel functions that satisfy the moment conditions to any order $(n-1)$ for an arbitrary placement of nodes as typified by unstructured grids on finite domains, Ω, with complex geometry.

The RKPM formulation begins with the notion of a continuous kernel approximation of a function, U^R, on a domain $\Omega_{\mathbf{y}}$,

$$U^{R,a}(\mathbf{x}) = \int_{\Omega_y} U(\mathbf{y}) \phi^a(\mathbf{x} - \mathbf{y}) d\Omega_{\mathbf{y}}, \tag{2.101}$$

where ϕ^a is the kernel function and $U^{R,a}$ is a continuous approximation to U at some scale a [49, 47]. A wide variety of kernel functions have been used including cubic B-splines and gaussian distributions, though ideally, the kernel has compact support. Kernel functions in multiple dimensions may be generated by taking the tensor product of the one-dimensional forms, producing functions with rectangular (two-dimensional) or cubic (three-dimensional) support.

In order to address discrete problems, numerical quadrature (e.g., trapezoidal or particle integration) is used to evaluate Eq. (2.101) as

$$U^{h,a}(\mathbf{x}) = \sum_{i=1}^{n} d_i \phi^a(\mathbf{x} - \mathbf{x}_i) V_i = \sum_{i=1}^{n} d_i \phi_i^a(\mathbf{x}) V_i, \tag{2.102}$$

where n is the total number of nodes whose kernel functions incorporate $\mathbf{x}$ within their support, $U^{h,a}$ is the (continuous) analogue of $U^{R,a}$ arising from the discretization, and d_i and V_i are the coefficients and volumes respectively associated with particle i [47]. In general, the coefficients, d_i are different from the value of the function at particle i because the RKPM basis is non-nodal (i.e., it does not posses the Kronecker-delta property).

The remaining presentation requires a choice of domain dimensionality. For clarity, we consider a two-dimensional space, although results may be expanded to higher (or lower) dimensions. Consideration of two-dimensional space allows inclusion of details not obvious in a one-dimensional space.

In general, Eq. (2.102) will not exactly reproduce an arbitrary polynomial. To allow for accurate reproduction of polynomials to degree p, a modified kernel function $\overline{\phi}_i^a$ is introduced which satisfies the reproducing conditions,

$$\sum_{i=0}^{n} x_i^k y_i^l \overline{\phi}_i^a(\mathbf{x}) V_i = x^k y^l \quad 0 \le k, l \le p \tag{2.103}$$

Application of Eq. (2.103) with $p = 1$ results in *bi-linear* reproducing conditions. That is $[1, x, y, xy]$ are reproduced. In many cases reproduction of xy is not enforced and only *linear* consistency is considered (this is the approach taken in the discussion which follows). The motivation for giving up the xy term will become clear later.

The modified kernel function, $\overline{\phi}_i^a$, for linear consistency ($p = 1$) in a two-dimensional spatial domain, may be generated by assuming its form to be an expansion of the original kernel function ϕ_i^a,

$$\overline{\phi}_i^a(\mathbf{x}) = \sum_{k+l=0}^{p} \beta_{k,l}(\mathbf{x}) \phi_i^a(\mathbf{x}) (x - x_i)^k (y - y_i)^l \quad 0 \le k, l \le p \tag{2.104}$$

where $\beta_{k,l}(\mathbf{x})$ is a set of correction functions that vary continuously within the domain [47, 48]. This modified kernel function replaces $\phi_i^a(\mathbf{x})$ in Eq. (2.102) yielding

$$U^{h,a}(\mathbf{x}) = \sum_{i=1}^{Nnp} d_i \overline{\phi}_i^a(\mathbf{x}) V_i. \tag{2.105}$$

Substituting Eq. (2.104) into Eq. (2.105) and requiring the resulting equation to satisfy the desired reproducing conditions of Eq. (2.103) results in,

$$\beta_{0,0}(\mathbf{x})\sum_{i=1}^{n}\phi_i^a(\mathbf{x})\Delta V_i + \beta_{1,0}(\mathbf{x})\sum_{i=1}^{n}\phi_i^a(\mathbf{x})\Delta V_i + \beta_{0,1}(\mathbf{x})\sum_{i=1}^{n}\phi_i^a(\mathbf{x})\Delta V_i = 1, \tag{2.106}$$

$$\beta_{0,0}(\mathbf{x})\sum_{i=1}^{n}x_i\phi_i^a(\mathbf{x})\Delta V_i + \beta_{1,0}(\mathbf{x})\sum_{i=1}^{n}x_i\phi_i^a(\mathbf{x})\Delta V_i + \beta_{0,1}(\mathbf{x})\sum_{i=1}^{n}x_i\phi_i^a(\mathbf{x})\Delta V_i = x \tag{2.107}$$

and,

$$\beta_{0,0}(\mathbf{x})\sum_{i=1}^{n}y_i\phi_i^a(\mathbf{x})\Delta V_i + \beta_{1,0}(\mathbf{x})\sum_{i=1}^{n}y_i\phi_i^a(\mathbf{x})\Delta V_i + \beta_{0,1}(\mathbf{x})\sum_{i=1}^{n}y_i\phi_i^a(\mathbf{x})\Delta V_i = y. \tag{2.108}$$

It is apparent from Eq. (2.106) through (2.108) that determination of $\overline{\phi}_i^a(\mathbf{x})$ is dependent upon finding the set of β's which enforce the reproducing conditions Eq. (2.103). We begin by defining the moments of the original kernel functions as,

$$m_{k,l}(\mathbf{x}) = \sum_{i=1}^{n}\phi_{k,l}(\mathbf{x})(x-x_i)^k(y-y_i)^l\Delta V_i. \tag{2.109}$$

Substituting Eq. (2.109) into Eq. (2.106) yields,

$$\beta_{0,0}(\mathbf{x})m_{0,0}(\mathbf{x}) + \beta_{1,0}(\mathbf{x})m_{1,0}(\mathbf{x}) + \beta_{0,1}(\mathbf{x})m_{0,1}(\mathbf{x}) = 1. \tag{2.110}$$

Multiplying the RHS of Eq. (2.107) and Eq. (2.108) by the LHS of Eq. (2.106) and incorporating Eq. (2.109) yields,

$$\beta_{0,0}(\mathbf{x})m_{1,0}(\mathbf{x}) + \beta_{1,0}(\mathbf{x})m_{2,0}(\mathbf{x}) + \beta_{0,1}(\mathbf{x})m_{1,1}(\mathbf{x}) = 0, \tag{2.111}$$

and,

$$\beta_{0,0}(\mathbf{x})m_{0,1}(\mathbf{x}) + \beta_{1,0}(\mathbf{x})m_{1,1}(\mathbf{x}) + \beta_{0,1}(\mathbf{x})m_{0,2}(\mathbf{x}) = 0. \tag{2.112}$$

Thus, the β's may be found by solving the matrix system,

$$\mathbf{M}(\mathbf{x})\mathbf{b}(\mathbf{x}) = \mathbf{P}(0) \tag{2.113}$$

where,

$$\mathbf{M}(\mathbf{x}) = \begin{bmatrix} m_{0,0}(\mathbf{x}) & m_{1,0}(\mathbf{x}) & m_{0,1}(\mathbf{x}) \\ m_{1,0}(\mathbf{x}) & m_{2,0}(\mathbf{x}) & m_{1,1}(\mathbf{x}) \\ m_{0,1}(\mathbf{x}) & m_{1,1}(\mathbf{x}) & m_{0,2}(\mathbf{x}) \end{bmatrix}, \tag{2.114}$$

$$\mathbf{P}^{\mathbf{T}}(0) = [1,0,0] \tag{2.115}$$

and,

$$\mathbf{b}^{\mathbf{T}}(\mathbf{x}) = [\beta_{0,0}(\mathbf{x}), \beta_{1,0}(\mathbf{x}), \beta_{0,1}(\mathbf{x})]. \tag{2.116}$$

The matrix system of Eq. (2.113) must be solved at every discrete point for which the reproduced function, $U^{h,a}$, is desired. In the context of LES filtering, solution to Eq. (2.113) is required for all nodal points in the domain.

Appendix A provides a description of the spectral behavior of RKPM filters.

2.7.4.2 Filtering based on Lumped Mass Projection A natural explicit test filter for unstructured finite element codes (such as MPSalsa [68, 69]) is what can be called a lumped mass projection to the nodes. This has been used elsewhere in the literature [31], and is convenient in that it uses the finite element basis functions already coded. Given some scalar quantity $\bar{\phi}$ which is resolved on the mesh at each grid point, $\tilde{\bar{\phi}}$ can be computed as the L_2-projection of $\bar{\phi}$ at node point i by

$$\tilde{\bar{\phi}}_i = \frac{\sum_e \int_{\Omega_e} \mathbf{\Phi_i} \bar{\phi} \mathbf{d\Omega}}{\sum_e \int_{\Omega_e} \mathbf{\Phi_i} \mathbf{d\Omega}}. \tag{2.117}$$

Here, $\mathbf{\Phi_i}$ is the standard polynomial finite element basis function, the summation is over all elements that contain node i, and integration is over each element that supports node i.

The authors are not aware of any analysis evaluating the commutation errors associated with this filter for nonuniform or irregular meshes. However, it appears to be commonly assumed that if the mesh size changes smoothly over the domain and changes between neighboring elements are small (of order a few percent), then the errors introduced are acceptably small.

2.8 The Near-wall Resolution and Modeling problem

LES typically works well when the mesh resolution used on a given flow problem is such that the kinetic energy associated with the resolved eddies is a large fraction of the total kinetic energy in the flow. Unfortunately, in turbulent wall-bounded flows the large, energy containing eddies (from a local perspective) typically scale as the distance from the wall. As the Reynolds number increases and the viscous sub-layer shrinks, the number of grid points required to resolve the near-wall eddies increases dramatically. This near-wall resolution requirement is possibly the most severe bottleneck in applying LES to turbulent flows of practical interest. As a result, a variety of modeling approaches have been developed.

The ideal case of a steadily forced turbulent boundary layer over a flat wall exhibits a universal structure embodied in the 'law of the wall,' and has provided the basis for many early modeling approaches. Because several authors, including Cabot [8], Ciofalo [11], and Sagaut [66], provide excellent reviews of the variety of near-wall models that have been proposed, an additional review will not be provided here. However, as explained by Baggett [2], these approaches typically replace the no-slip boundary condition with an approximate boundary condition, such as the specification of the wall stress. Unfortunately, complex flows of practical interest often do not conform well to idealized near-wall behavior. Near-wall flows are subject to unsteady forcing and (potentially) multiphysics processes (thermally induced property variations, gravitational and other body forces, multiphase couplings, etc.) whose dynamic interactions with the bulk flow are not captured by currently available wall

treatments. Thus, it is not surprising that current modeling approaches are considered inadequate for many problems of interest to the community [32].

A more recent class of modeling approaches is based on the idea of merging LES with RANS to model the near-wall region [2, 57]. This is basically an extension of the idea Schumann [67] suggested some years ago, but instead of using a simple mixing-length eddy viscosity, these models use more sophisticated procedures to compute the near-wall eddy viscosity. In essence, these models apply an anisotropic near-wall filter in which the wall-normal filter width becomes very small, but the wall-parallel filter width remains large. Near-wall turbulent transport is then incorporated primarily through a modified diffusion mechanism. A disadvantage of this approach is that near-wall turbulent fluctuations are suppressed, and the proper dynamic coupling between the wall and the bulk flow is difficult to achieve.

Later in this report we will discuss our work to explore an approach that, from a filtering standpoint, can be thought of as similar to the LES/RANS approach just mentioned, where the wall-normal filter width becomes small, but the wall-parallel filter width remains large. However, instead of coupling to a time/ensemble averaged RANS model, this approach is based on the idea of coupling to the ODT model of Kerstein [35], a fundamentally unsteady model. In the near-wall region, finely resolved ODT lines are embedded within a coarse LES mesh and the ODT evolution equations capture fine-scale temporal and spatial variations (in one direction) of the three-component velocity field. Near-wall turbulent transport is modeled through the combined effect of a sequence of fluid-element rearrangements (called eddy events), without the introduction of an eddy viscosity. LES/ODT coupling is bi-directional and occurs both through the direct calculation of the subgrid turbulent stress by temporally and spatially filtering the ODT-resolved momentum fluxes (up-scale coupling), and through the LES-resolved mean pressure and velocities impacting the ODT behavior (down-scale coupling). The overall goal of this work is to develop and demonstrate a method that avoids the overwhelming computational expense of a finely resolved 3-D mesh in the near-wall region, and yet provides well-resolved near-wall dynamic behavior for high-Reynolds number wall-bounded flows.

3 Implementation and Testing of LES Models and Utilities in MPSalsa

Because of the large scale computational cost of LES, most LES codes have been written using data structures that assume a structured grid type of computational domain. Although useful for model development and evaluation, such codes cannot treat the complex geometries that may occur in many engineering problems of interest. Furthermore, many LES models in use today implicitly assume uniform meshes in order to preserve the property that the filtering operation commute with differentiation. Irregular meshes violate this assumption, introducing the need for using more general LES models and filtering techniques.

MPSalsa [68, 69] is an unstructured-grid finite-element code developed at Sandia for simulating both reacting and non-reacting flow. Unfortunately, the code has not yet been optimized for performing LES. However, the code is written to efficiently use Sandia's large massively parallel computers, and thus is a suitable code for testing a variety of unstructured grid LES concepts and models. In this project, significant revisions and modifications have been made in MPSalsa to incorporate a range of LES subgrid models, unstructured grid filters, statistics gathering routines and new boundary conditions necessary for model testing and development.

Models and utilities that have been incorporated to date include the following.

(1) Two constant coefficient subgrid models, the Smagorinsky model and the Ksgs model, were implemented. The Ksgs model requires the solution of an additional transport equation for the "sub-grid-scale" turbulent kinetic energy (i.e. Ksgs).

(2) Dynamic coefficient versions of the two LES subgrid models (Smagorinsky, Ksgs) were implemented. These models require explicit filtering of the resolved field in order to dynamically compute the local values of the model coefficients as they evolve in time and space.

(3) Two different filtering approaches have been implemented: the "lumped mass projection" (LMP) filter, and a filter based on "reproducing kernel particle method" (RKPM) ideas. The LMP filter has been used in other unstructured grid LES codes but does not control commutivity errors on irregular meshes. The RKPM filter is a new filtering approach which allows one to control commutivity errors on irregular meshes.

(4) A new "conserved scalar - laminar flamelet" LES turbulent combustion model has been implemented and tested that has the unique feature of not assuming statistical independence between mixture fraction and scalar dissipation. This model compliments the EDC model of Magnussen that had been previously coded in MPSAlsa.

(5) A set of routines were written to compute and store the important time-averaged statistical quantities necessary to evaluate the results of the LES simulations after they are completed.

(6) A set of routines were written to compute and store at nodes (as auxiliary variables) gradient-based quantities needed for LES. For example, the eddy viscosity is typically computed based on the shear stress tensor (whose components are all velocity gradients).

(7) Code revisions were completed to treat 3-D periodic boundary conditions (non-trivial for unstructured grid, parallel code). These boundary conditions are required to simulate the classic experiment of Comte-Bellot and Corrsin [12] on the decay of isotropic turbulence.

In addition to the MPSalsa code infrastructure work described above, a set of separate LES post-processing utilities compatible with the EXODUS II database standard were written and tested. They include the following.

(1) NODAL_STATS: A code for computing time avg. moments for stationary data (16 different quantities, stored in 3-D or 2-D as appropriate),

(2) ISO_STATS: A code for computing the statistics for spatially homogeneous flows, and

(3) EXO_PERIODIC: A code for adding the redundant node data to the special EXODUS files set up for periodic boundary conditions. Without this post processing, flows with periodic boundary conditions cannot be visualized with available tools such as AVS express or TECPLOT.

With the MPSalsa LES model infrastructure in place, and the post processing utilities written, numerical experiments were begun to test and evaluate the performance of different models and filters. To date, all models and filters have been tested by doing simulations of the classic experiment of Comte-Bellot and Corrsin on the decay of isotropic turbulence. This experiment allows one to check how well a particular model and filter, on a mesh of a given resolution, captures two important things, (1) the correct overall decay of turbulent kinetic energy, and (2) the evolution of energy at different length scales (i.e., the energy spectrum in wave number space). Mesh refinement studies have been performed by varying the grid from 16^3 to 128^3. These results have demonstrated the improved predictive capabilities of the dynamic models (over the constant coefficient models) and illustrated the degrading effects of under-resolved numerical grids. This problem has also demonstrated the difference in effective filter width between the LMP filter and the RKPM filter.

A model for simulating non-premixed turbulent combustion based on the flamelet approach and scale-similarity mixing models has been developed and implemented. An 2-D axisymmetric simulation of a buoyant plume fire (burning methanol) was conducted and comparisons were made with experiments and other Sandia codes. The results demonstrate the ability to capture the instabilities that lead to flame "puffing", the code's ability to simulate flows with very high density ratios, and ability to simulate complex unsteady coupled physics problems using the finite element method on unstructured grids. A fully three dimensional simulation is planned.

Details of this work are given in the following subsections.

3.1 LES Subgrid Models in MPSalsa

3.1.1 Standard Smagorinsky

The standard Smagorinsky model as described in Section 2.5.1.1 of this report has been implemented into MPSalsa. The Smagorinsky constant C_S is a compiled value set at 0.1. The model is activated by inserting the following lines in the MPSalsa input file under the "Turbulence Model Specifications" section:

Turbulence Model = SM

The model does not require any special boundary conditions, and output is specified in the standard way.

3.1.2 Standard Ksgs

The Ksgs model as described in Section 2.5.1.2 of this report has been implemented into MPSalsa. In this model the following three constants must be prescribed, $C_\nu, C_k, C_\varepsilon$. The compiled values for these three constants are currently set to
$C_\nu = 0.0854$,
$C_k = 1.0$, and
$C_\varepsilon = 0.916$.
The model is activated by inserting the following lines in the MPSalsa input file under the "Turbulence Model Specifications" section:

Turbulence Model = LES-k

Since an additional transport equation for Ksgs is being solved, appropriate boundary conditions for this equation, and any desired output must be specified in the input file in the standard way.

3.1.3 Dynamic Smagorinsky

The dynamic Smagorinsky model as described in Section 2.5.1.3 of this report has been implemented into MPSalsa. The model is activated by inserting the following lines in the MPSalsa input file under the "Turbulence Model Specifications" section:

Turbulence Model = DYN-SM

The model does not require any special boundary conditions, and output is specified in the standard way. However, because the dynamic model requires an explicit filtering operation (in order to compute the dynamic constant), the user may add the following line to specify the use of lumped mass projection type filter

LES Filter Type = LMP

or may specify filtering based on the RKPM approach with

LES Filter Type = RKPM

Based on the analysis of Lund [50], the ratio of the test filter width $\widetilde{\Delta}$ to the implicit filter Δ is 2.0 and $\sqrt{12}$ for the LMP and RKPM filters respectively.

The default value used in the MPSalsa is the LMP filter. Both of these filtering approaches are described below in Section 3.2.

3.1.4 Dynamic Ksgs

The Ksgs model as described in Section 2.5.1.4 of this report has been implemented into MPSalsa. The model is activated by inserting the following lines in the MPSalsa input file under the "Turbulence Model Specifications" section:

Turbulence Model = DYN-LES-k

Since an additional transport equation for Ksgs is being solved, appropriate boundary conditions for this equation, and any desired output must be specified in the input file in the standard way. Also, because the dynamic model requires explicit filtering operations, the user may add the following line to specify the use of lumped mass projection type filter

LES Filter Type = LMP

or may specify filtering based on the RKPM approach with

LES Filter Type = RKPM

Based on the analysis of Lund [50], the ratio of the test filter width $\widetilde{\Delta}$ to the implicit filter Δ is 2.0 and $\sqrt{12}$ for the LMP and RKPM filters respectively.

The default value used in MPSalsa is the LMP filter. Both of these filtering approaches are described below in Section 3.2.

3.2 Explicit LES Filtering options in MPSalsa

As described in Section 2, there are a variety of LES models which require a secondary filtering operation. Currently in MPSalsa, the two dynamic LES models (Sec.s 2.5.1.3 2.5.1.4 are the only models requiring a second filter.

Two different discrete filters have been implemented; the "lumped mass projection" (LMP) filter, and a filter based on "reproducing kernel particle method" (RKPM) ideas.

3.2.1 Lumped Mass Projection (LMP) Filtering

As explained in 2.7.4.2, the LMP filter is a natural explicit test filter for unstructured finite element codes in that it is based on the finite element basis functions already coded.

This filter has been implemented into MPSalsa and two point gauss quadrature is used evaluate the integrals in Eq. 2.117. LMP is the default filter for the dynamic LES subgrid models if nothing is specified by the user in the input file. It can be directly specified by the user by adding the following line to the MPSalsa input file under the "Turbulence Model Specifications" section:

LES Filter Type = LMP

3.2.2 Reproducing Kernel Particle Method (RKPM) Filters

The RKPM filter described in Section 2.7.4.2 has been coded into MPSalsa. When activated, this requires a special preprocessing step where the local weights are calculated based on the neighbor node locations (see Eqs. 2.111 - 2.116). It is specified by the user by adding the following line to the MPSalsa input file under the "Turbulence Model Specifications" section:

LES Filter Type = RKPM

3.3 Conserved Scalar - Laminar Flamelet SGS Combustion Model

In chemically reacting flows, additional transport equations need to be solved in order to specify the thermochemical state of the mixture. Depending upon the assumptions of the particular combustion model being used different quantities may be solved for. Here we provide a brief description of a conserved scalar - laminar flamelet subgrid combustion model for turbulent nonpremixed flames that was implemented and tested in MPSalsa as part of this work.

3.3.1 Model Description

In this model additional transport equations are numerically solved for the filtered temperature $\bar{T}$ and the filtered mixture fraction $\bar{Z}$. The filtered temperature equation can be written as

$$\frac{\partial(\overline{\rho C_p}\bar{T})}{\partial t} + \frac{\partial}{\partial x_j}(\overline{\rho C_p}\bar{T}\bar{u}_j) = \frac{\partial}{\partial x_j}\left[(k + \frac{\mu_s}{Pr_t})\left(\frac{\partial \bar{T}}{\partial x_j}\right)\right] + \sum_{s=1}^{Ns} h_s W_s \overline{\dot{\omega}}_s + \overline{\dot{Q}} \tag{3.1}$$

where C_p is the specific heat, k is the thermal conductivity, Pr_t is a turbulent Prandtl number, h_s is the specific enthalpy of of formation of species s, W_s is the molecular weight of species s, $\overline{\dot{\omega}}_s$ is the volumetric production of species s, and $\overline{\dot{Q}}$ a volumetric energy source term.

The filtered mixture fraction equation can be written as

$$\frac{\partial(\bar{\rho}\bar{Z})}{\partial t} + \frac{\partial}{\partial x_j}(\bar{\rho}\bar{Z}\bar{u}_j) = \frac{\partial}{\partial x_j}\left[(D_m + \frac{\mu_s}{Sc_t})\left(\frac{\partial \bar{Z}}{\partial x_j}\right)\right]. \tag{3.2}$$

where D_m is the species diffusivity and Sc_t is a turbulent Schmidt number.

The mixture fraction, which is the mass fraction of elemental fuel species in a given flow sample, is this model's "conserved scalar", in what is more generally called a conserved scalar approach. This approach is useful under conditions when chemical reaction rates are much faster than the rate at which reactants are mixed.

The particular model described here is based on experimental observations of laminar flames [6] which showed that major species concentrations collapsed to a single curve when plotted versus mixture fraction. These relationships between species mass fractions and the mixture fraction are called state relationships, and are written in the form

$$Y_s = Y_s(Z) \tag{3.3}$$

where Y_s and Z are the mass fraction of species s and the mixture fraction, respectively. For modeling purposes, simple polynomial curve fits are used to approximate the experimental data.

If species diffusivities are assumed equal, then Eqs. 3.3 can be substituted into transport equations for Y_s (not shown here) to obtain the following expression for the reaction rate of each species s:

$$\dot{\omega}_s = -\frac{1}{2}\rho\chi\frac{d^2Y_s}{dZ^2} \tag{3.4}$$

where the scalar dissipation rate χ is defined as

$$\chi = 2D_m\frac{\partial Z}{\partial x_j}\frac{\partial Z}{\partial x_j} \tag{3.5}$$

and D_m is the species diffusivity.

In LES, the flame is typically not spatially resolved. Therefore, in order to incorporate a conserved scalar approach it is assumed that at the subgrid level there exists a statistical ensemble of laminar diffusion flamelets each satisfying the universal state relationships. The average chemical production rate of this ensemble may then be found by integrating Eq. (3.4) over the joint PDF of mixture fraction and scalar dissipation rate, $P_{Z\chi}$.

$$\overline{\dot{\omega}_s} = -\frac{1}{2}\int_0^{\chi max}\int_0^1 P_{Z\chi}\rho(\zeta)\chi\frac{d^2Y_s(\zeta)}{d\zeta^2}d\zeta d\chi \tag{3.6}$$

This joint PDF represents the probability of finding Z and χ in a subgrid volume weighted by a filtering function at a particular point in space and time.

In contrast to an earlier model initially tested that assumed statistical independence between the mixture fraction and the scalar dissipation rate [15, 16] the current model does not make this assumption. Details of its derivation are presented elsewhere [16] and yield the following analytical expression for the mean reaction rate:

$$\overline{\dot{\omega}_s} = -\frac{1}{2}C_s\bar{\rho}(z_{st})\frac{DF(Z_{st})}{Dt} \tag{3.7}$$

where $\frac{DF(Z_{st})}{Dt}$ is a Lagrangian derivative that requires explicit calculation locally in both time and space for the LES.

In addition, the filtered mass fraction is required for computation and found by simply integrating the state relationships over the PDF of mixture fraction, i.e.

$$\tilde{Y}_s = \int_0^1 P_Z(\zeta)Y_s(\zeta)d\zeta. \tag{3.8}$$

In MPSalsa the assumed shape of the PDF was chosen to be a beta function, which leads to an equation of the following form

$$\overline{\dot{\omega}_s} = \frac{1}{2}(b_2 - b_1)\bar{\rho}(z_{st})\frac{D}{Dt}\int_0^{Z_{st}} I_\beta(\xi, \beta_1, \beta_2)d\xi \tag{3.9}$$

for the filtered chemical production rate.

The assumed beta PDF (see [14, 16] for details) requires the specification of the the subgrid variance $\widetilde{z''^2}$ in addition to the mean mixture fraction. In this model a scale similarity model is used to compute $\widetilde{z''^2}$ as follows:

$$\widetilde{z''^2} = \sigma_z^2 = (\widetilde{\tilde{z}\tilde{z}} - \tilde{\tilde{z}}\tilde{\tilde{z}}). \tag{3.10}$$

3.3.2 Model Activation in MPSalsa

When performing an LES calculation in MPSalsa, the conserved scalar - laminar flamelet model can be activated by inserting the following lines in the MPSalsa input file under the "Turbulence Model Specifications" section:

Turbulent Combustion Model = flamelet
Number of Flamelet Species = 5

The first line specifies the turbulent combustion model. If the name specified is "flamelet", then the second line must be included in order to specify the number of flamelet species (which in this example is five). Appropriate material properties, boundary conditions, and output is specified in the standard way.

3.4 Gradient Based Auxiliary Variables in MPSalsa

Vorticity and strain rate tensor are two examples of auxiliary variables that are important to the analysis of turbulent flows. Since these variables are functions of gradients, and gradients are undefined at the nodes, a special procedure is required to estimate these quantities. Volume (area in 2-D) average approximations to the gradients are reconstructed by integrating over all the elements that support a given node,

$$\overline{\nabla u_i} = \frac{\sum_e \int_{\Omega_e} \mathbf{\Phi_i} \nabla \mathbf{u} d\mathbf{\Omega}}{\sum_e \int_{\Omega_e} \mathbf{\Phi_i} d\mathbf{\Omega}} \tag{3.11}$$

Here, $\mathbf{\Phi_i}$ is the standard polynomial finite element basis function (linear in MPSalsa), the summation is over all elements that contain node i, and integration is over each element that supports node i. In MPSalsa, evaluation of the volumetric integrals is performed by standard two-point Gaussian quadrature.

This weighted average is sometimes referred to as a lumped mass projection [31], and is similar to the spatial filter described above in Section 2.7.4.2. When gradient based auxiliary variables are requested this procedure is conducted and these variables are output in the auxiliary output file. A list of all gradient based auxiliary variables that MPSalsa recognizes appears in the file rf_salsa.inp, which is part of the MPSalsa distribution.

3.5 Statistics Gathering in MPSalsa

It should not be understated that turbulent flows are non-deterministic and the "solutions" from DNS and LES are most meaningful in the form of statistical quantities derived from the numerical solutions. Indeed, the amount of data created from simulations is enormous and one would quickly become overwhelmed if not for meaningful data reduction techniques.

Two methods have been developed for generating statistics from data obtained from simulations run with MPSalsa . The first method is designed for stationary (in time) and ensemble averaged transient flows, having zero, one or two periodic boundaries. A postprocessing code called NODAL_STATS is used to compute the final moments. Moments of the "raw" data are generated using Eqs 2.55 - 2.60. In MPSalsa, stationary data is stored in an auxiliary variable file. The file is created prior to the simulation using a utility called "add_var". The auxiliary variable file contains the desired summations (eg. $< u >$, and $< u * u >$) to compute the stationary moments of the data. MPSalsa recognizes strings and stores the data associated with a particular string as a running sum. The summations are computed at each node after every time step. The data is output at a user defined frequency, and the variable is set to zero in order that a new summation can begin. At the end of a simulation, NODAL_STATS is run to combine the output and divide by the time duration. NODAL_STATS queries the data and automatically determines what moments can be calculated. It then calculates all the moments, creates a new EXODUSII file and writes all the moments to the new file. In other words, all time step data is reduced to a single field on the same mesh, independent of time. This file can then be manipulated to produce line plots, for example. A list of the summation variables that MPSalsa recognizes appears in the rf_salsa.inp file which is part of the MPSalsa distribution.

The second method for generating statistics from unsteady MPSalsa data is designed for spatially homogeneous flows where all three boundaries are periodic. In this case, the data is assumed to be stationary in space, but evolving in time. Therefore, no auxiliary variables and no auxiliary variable file need to be defined. Instead, all statistical quantities are derived from the nodal unknowns that define the problem, (i.e. pressure, velocity) Nodal unknowns are output at a user defined frequency. Then a postprocessing step is run using ISO_STATS. ISO_STATS reads from the nodal data file, one time plane at a time, generates homogeneous statistics, and writes the statistics as a function of time to various ASCII files. It also computes homogeneous energy and dissipation spectrums for each time level. The user can easily modify ISO_STATS to compute additional quantities of interest. Gradients are computed at the centroid of elements only. Only eight node hexahedra gradient calculations have been implemented. It is assumed that since the data is homogeneous, it is acceptable to compute the gradients at the centroid instead of the nodes. This effectively shifts the statistics calculation by one half the element dimension in each coordinate direction compared to other non-gradient based nodal statistics. The ASCII data files have a common

form where the columns are; time data1 data2 etc, and the rows represent the evolution in time.

3.6 Visualization utilities for problems with 3-D Periodic Boundary Conditions

In order to impose periodic boundary conditions on a problem being solved with MPSalsa, a special type of EXODUS file must be created with a mesh generator such as CUBIT [20]. The special aspect is that a set of extra element blocks must be created to effectively link nodes on one side of the domain to the appropriate nodes on the other side of the periodic direction. For one periodic direction, only one additional element block is created. For two periodic directions, three additional element blocks are created. And for periodic boundary conditions in all three dimensions, seven additional element blocks are needed (for a total of eight in the mesh). These extra element blocks are designed so that no new nodes are created, they simply provide the required connectivity between nodes on opposite sides of the domain.

Because the elements contained within the extra element blocks spatially overlap the primary elements in the mesh, visualization software cannot properly display the results. The solution to this problem is to post process the output file, creating a new file that contains the redundant node data consistent with the periodic conditions, and revising the element-node connectivity.

A simple utility called EXO_PERIODIC was been written that performs this postprocessing on unstructured grid EXODUS II based output files. It is available from the first author of this report, and works for both uniform as well as irregular meshes.

By comparing Figures 1 and 2, one can see the additional nodes and revised elements blocks that are created when using the EXO_PERIODIC utility on a 10x10x10 randomized mesh of a cubic region with 3-D periodic boundary conditions.

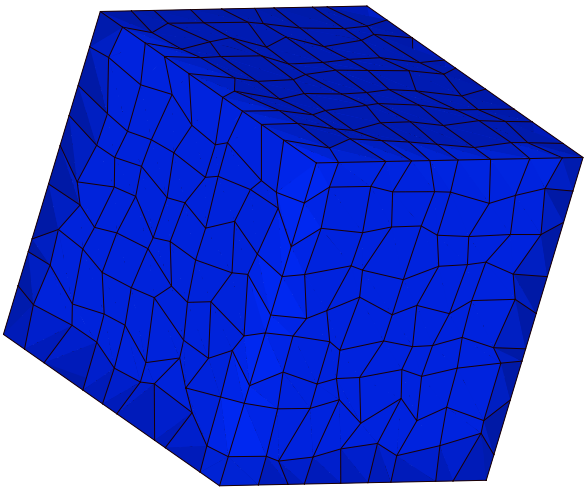

Figure 1: Element block 1 of a cubic region specially meshed to handle periodic boundary conditions.

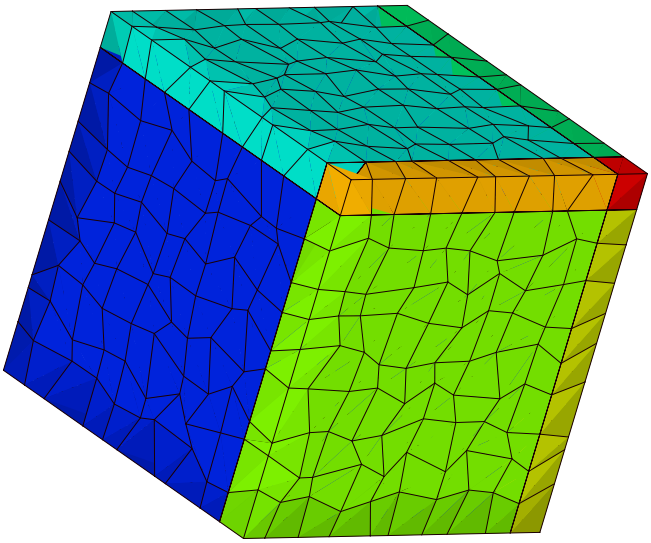

Figure 2: The revised mesh, element blocks and redundant nodes created by the EXO_PERIODIC utility of a cubic region specially meshed to handle periodic boundary conditions.

3.7 Calculations of Turbulence Decay in a Box

A standard test problem for LES is the simulation of decaying isotropic turbulence. The classic experiment by Comte-Bellot and Corrsin [12] provides data of adequate detail to reproduce the experiment numerically. In the actual experiment a wire mesh is placed in a wind tunnel. In the wake of the mesh turbulence is generated that is convected down stream becoming isotropic in the center of the tunnel. The mean velocity in the tunnel was 10 m/s and the mesh spacing was 5.08 cm. Measurements were taken at three locations down stream of the mesh. The mean velocity was large compared to the fluctuating velocity and so Taylor's hypothesis was used to relate the three down stream locations to three evolution times relative to a datum located at the mesh.

Numerical experiments are constructed by initializing a three-dimensional Cartesian mesh, shaped like a cube with equal mesh spacing in all three directions, with a random velocity field at time $t = 0$, having periodic boundary conditions in all three directions. The flow then evolves in time. The initial field is matched as closely as possible with the first measurement point in the tunnel and the goal of the simulation is to match the flow statistics for the subsequent two time levels. The initial conditions can not match the experiment exactly, however, they must contain similar turbulence properties. For example, we seek to match the initial energy spectrum, rms velocities (u'), longitudinal and transverse integral length scales (L_{11}, L_{12}), and turbulence Reynolds number ($Re_t = \frac{u' L_t}{\nu}$). In addition the discrete velocity field must be divergence free. The initial velocity field is generated by specifying an isotropic energy spectrum. In spectral space, random phase angles are assigned to the velocity components and then the field is transformed back to physical space.

Because the LES is only computing the resolved energy, the subgrid energy is subtracted from the total energy by truncating the experimental spectrum, and the initial field is generated from this truncated energy spectrum.

Since the initial field contains random phases, certain statistics are not properly reproduced, such as derivative skewness, and two-point correlations such as the transverse integral scale L_{12}. In order to remedy this problem, initial conditions are generated by a two-step process. In the first step, the simulation is run with the initial field containing random phases. At some arbitrary time, the simulation is halted. In the second step the energy spectrum is computed. This energy spectrum is compared to the target spectrum and the difference in energy is added to the velocity field to create a new initial field with the desired energy spectrum. The phase information is not altered in this process so the new initial field contains phase information that is closer to what real turbulence contains. The full simulation is then run.

In Figure 3, the energy decay of 32^3 and 64^3 simulations using the dynamic Ksgs and dynamic Smagorinsky model and no model, are compared to the experimental data. The lumped mass filter was used. While significant differences are observed, the dynamic model

clearly predicts the trends and nearly the correct rates of decay. Without a subgrid model, the predicted energy decay is clearly wrong.

In Figure 4, the resolved energy spectrums for 64^3 simulations using both dynamic models with the LMP filter are compared to experiments. In this case the LES contains a truncated spectrum due to the finite resolution. The first time level serves to provide initial conditions. The second and third time levels are then predicted and as can be seen, correct trends in shape of the spectrums are produced. The energy at the highest resolved wave numbers are dissipated at about the correct rate and the mid-wave numbers are somewhat over predicted. For the lowest wave numbers it should be noted that there are probably not enough samples to produce an accurate representation because there are only a few large eddies in the box. These results are consistent with other authors using similar numerical algorithms ([31]).

Figures 5 and 6 compare solutions using the LMP and RKPM discrete filters with both dynamic models. The two filters produce similar results on this uniformly gridded problem, as expected. Also shown in Figure 6 are the resolved energy spectrums for the no-model case. These results demonstrate the unphysical build-up of energy in the high wave numbers that is produced when a subgrid model is not activated.

As an additional test of the overall model, a highly resolved 128^3 simulation was performed. Under these conditions, the subgrid model accounts for only a very small fraction of the energy, and the overall solution should be very accurate. In Figure 7, the decay of the resolved TKE is plotted verses time and compared to the experimental data. The agreement is within experimental error, confirming our expectations.

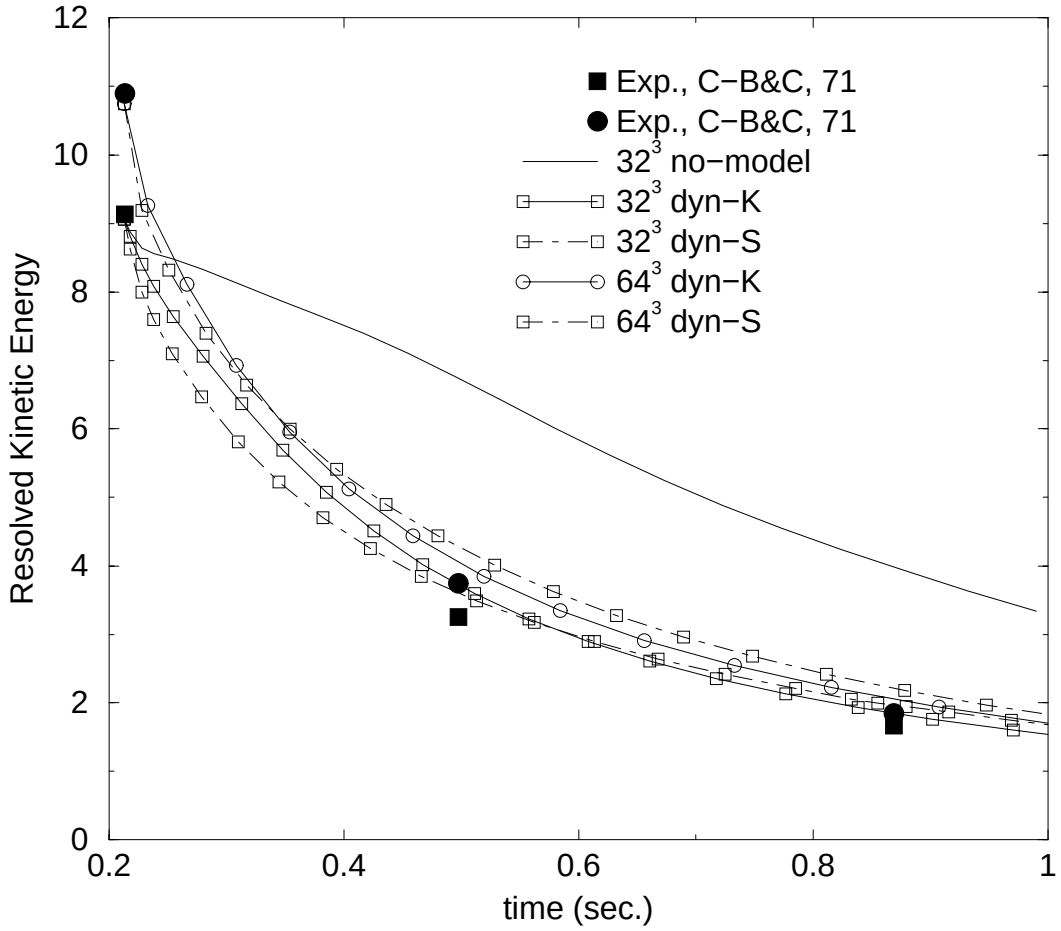

Figure 3: Decay of resolved TKE for 32^3 and 64^3 simulations using the dynamic Ksgs, dynamic Smagorinsky, and no model

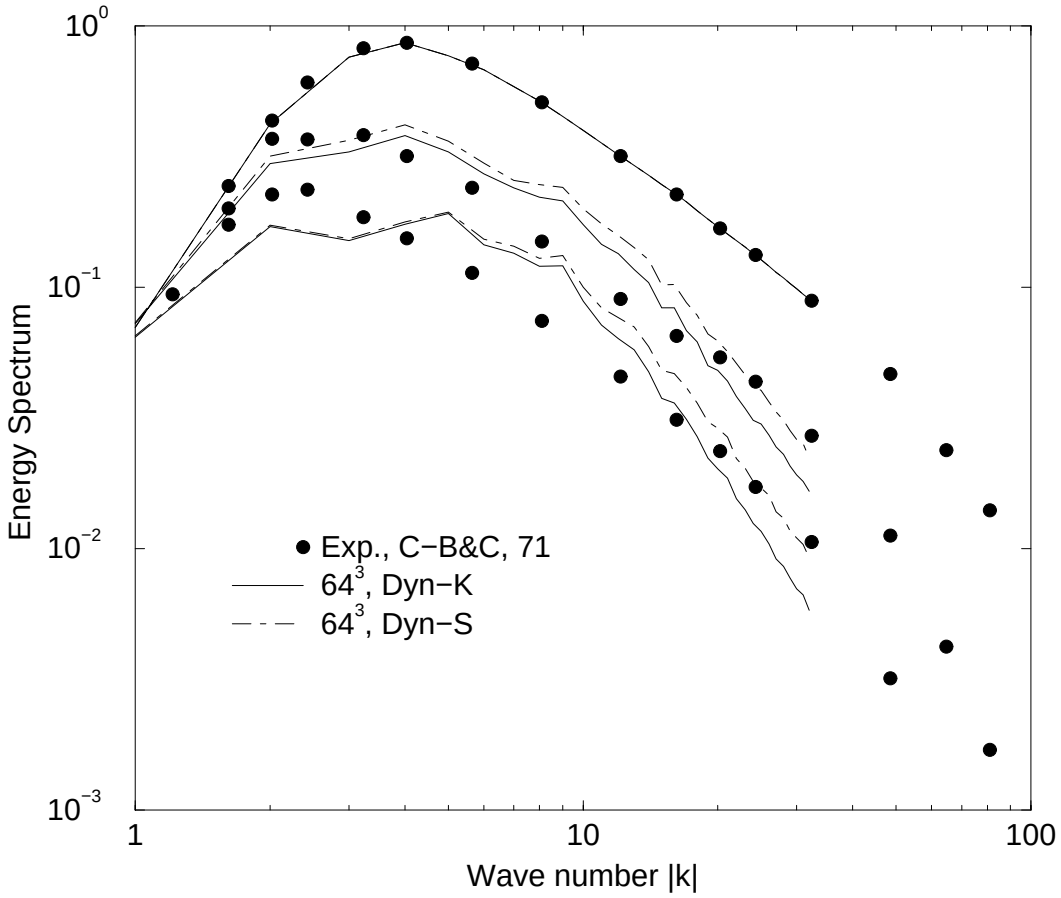

Figure 4: Resolved energy spectrums for the two dynamic models with a 64^3 grid compared to experiment.

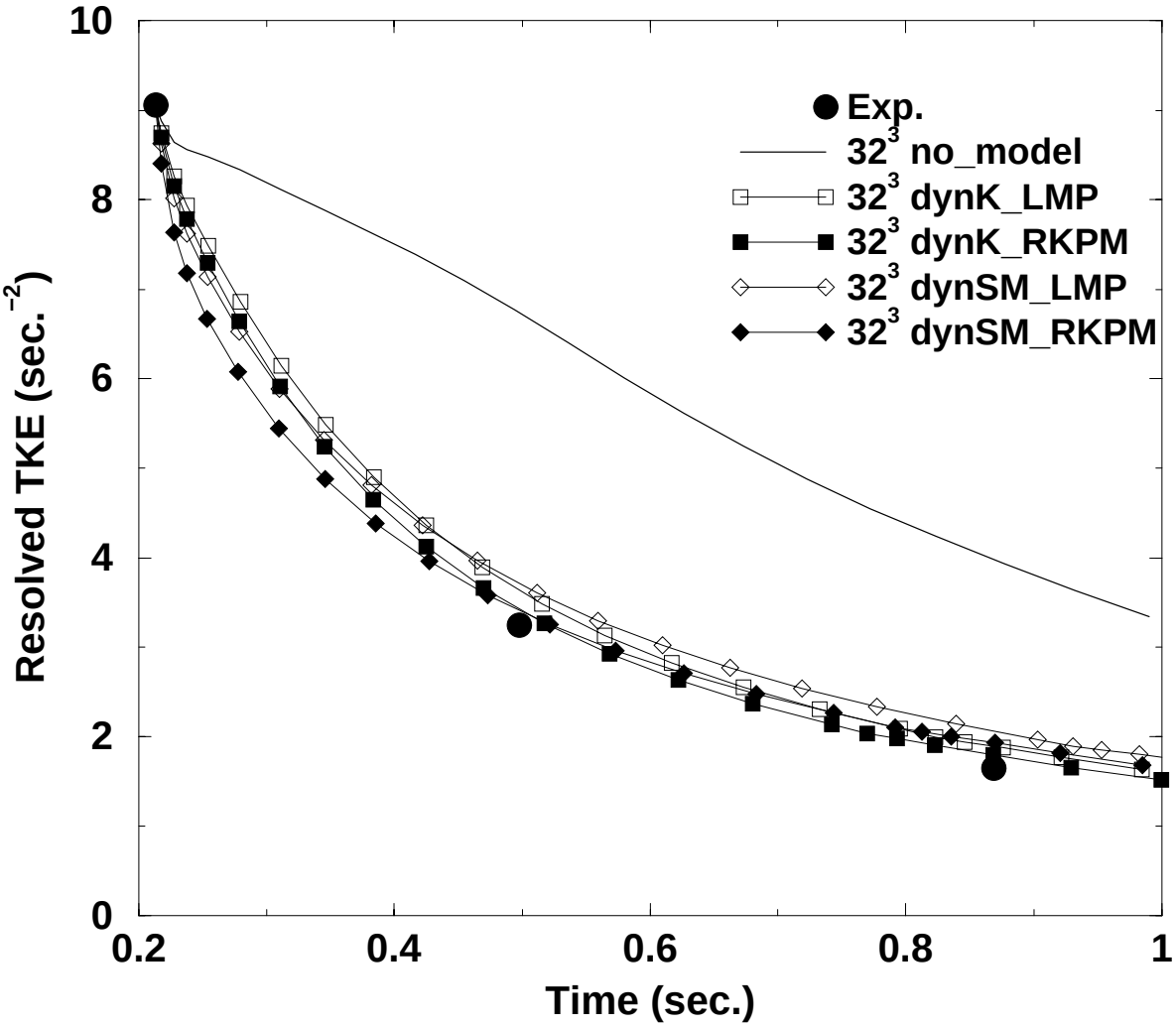

Figure 5: Decay of resolved TKE (32^3 grid) for two dynamic models with both LMP and RKPM filters compared to experiment.

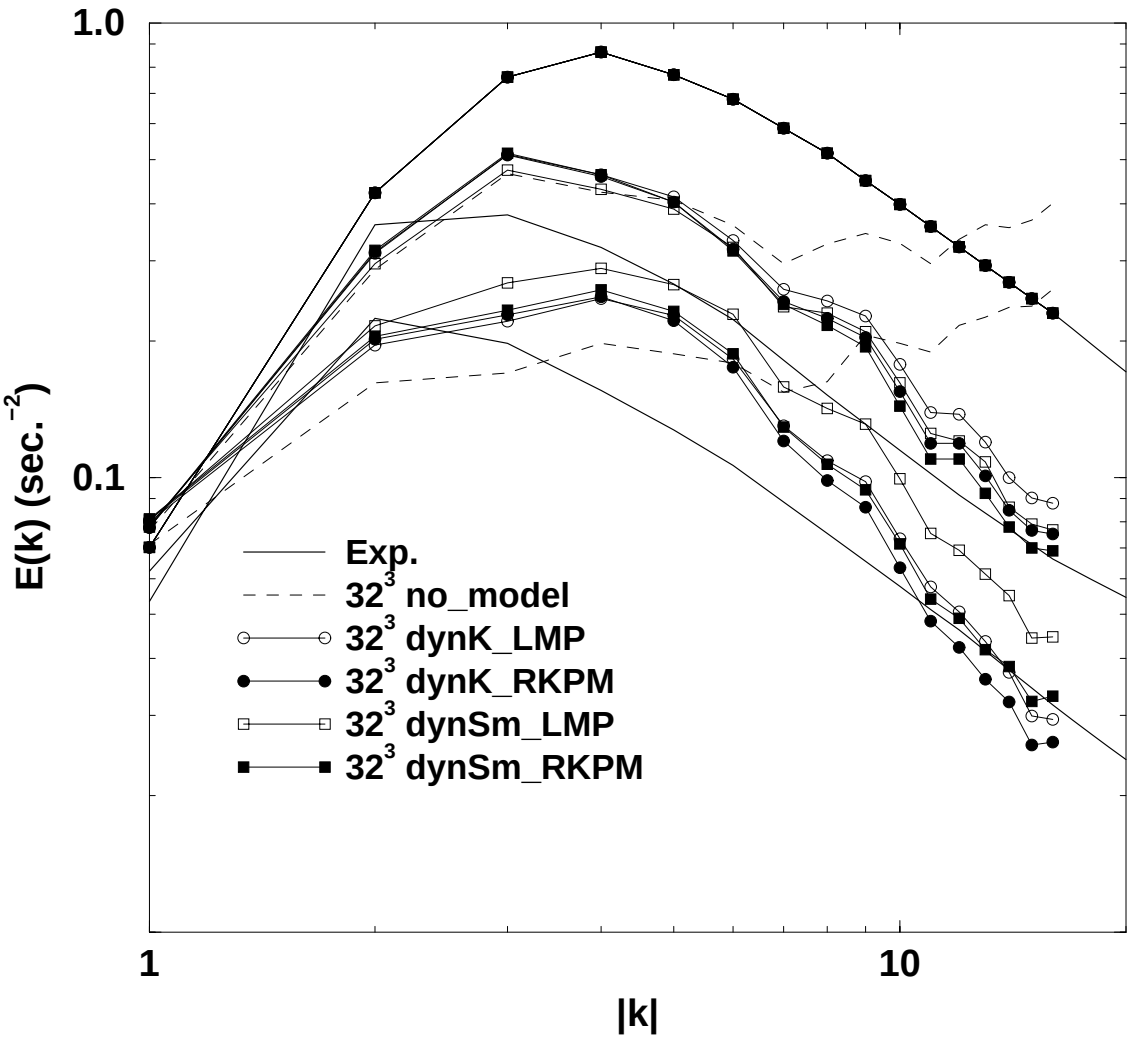

Figure 6: Resolved energy spectrums (32^3 grid) for two dynamic models with both LMP and RKPM filters compared to experiment.

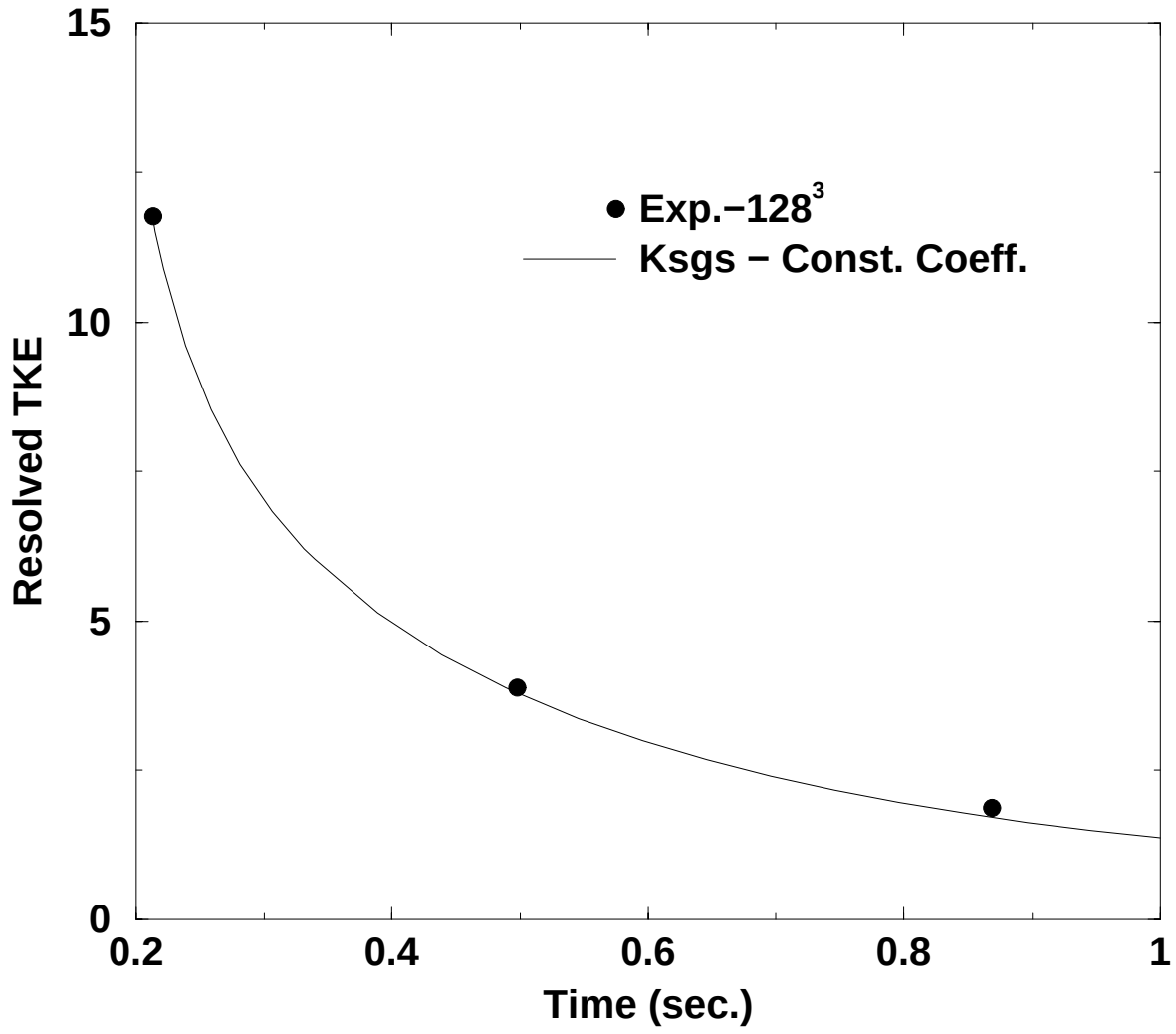

Figure 7: Decay of resolved TKE (128^3 grid) for a constant coefficient Smagorinsky model compared to experiment.

3.8 Simulations of a Methanol Pool Fire

LES calculations were performed with MPSalsa on an unstructured, 2-D mesh of a methanol pool fire, and compared to results from a 3-D LES with a structured code and a simpler RANS code calculation [16]. Two simple conserved scalar flamelet-based combustion models with assumed PDF are developed and implemented. The first model assumes statistical independence between mixture fraction and its variance and results in poor predictions of time-averaged temperature and velocity. The second combustion model makes use of the PDF transport equation or mixture reaction and does not employ the statistical independence assumption. Results using this model show good agreement with experimental data for both the 2-D and 3-D LES, indicating that the use of statistical independence between mixture fraction and its dissipation is not valid for pool fire simulations. Lastly, finger-like flow structures near the base of the plume, generated from stream-wise vorticity, are shown to be important mixing mechanisms for accurate prediction of time-averaged temperature and velocity.

We note that this work was motivated by efforts at Sandia to develop computational tools capable of modeling the heat transfer from large-scale pool fires. Large scale pool fires might occur after an aviation fuel spill or an aircraft accident, and have direct safety implications for nuclear weapons systems that could be immersed in the extreme thermal environment of such a fire.

3.8.1 Test Problem Description

The data set used for preliminary model validation is the 24.6 kW methanol pool fire of Weckman and Strong [76]. The pool has a diameter of 31 cm and is fed by a liquid pumping system which provides a volumetric flow rate at the pool surface of 1.35 cm^3/s . This data set includes point laser doppler velocimetry and thermocouple measurements of both time-averaged and fluctuating velocity and temperature. The methanol pool is located at least 1 m from the floor and is enclosed by a wire mesh to minimize disturbances. The local mixing of the flow field is controlled by the large scale stretched toroidal vorticies that are emitted at a puffing frequency fo 2.8 Hz. In addition, smaller scale finger-like structures that lie near the base of the plume are clearly visible.

3.8.2 Numerical Formulations

In addition to the MPSalsa calculations and model, two other numerical models were investigated in order to provide a comparison. The following three subsections summarize each of the three numerical models investigated here. Finally, the boundary conditions imposed on the simulations are briefly described.

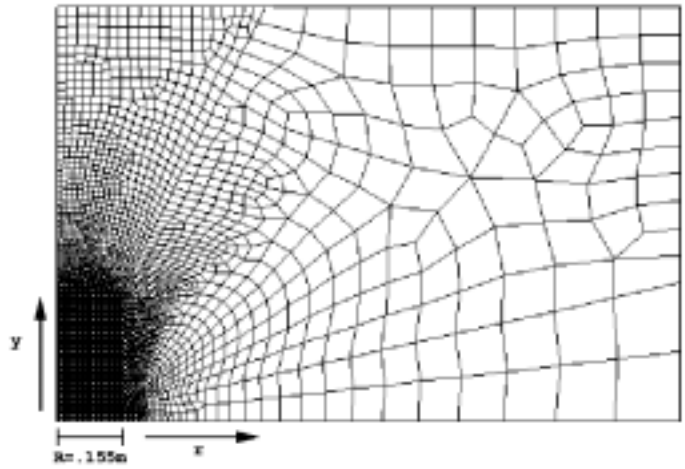

Figure 8: 2-D unstructured LES grid (5774 quadrilateral elements).

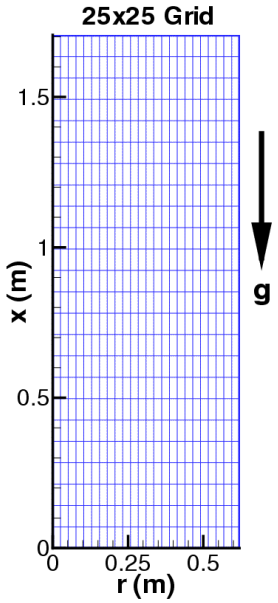

Figure 9: RANS grid (24x24 cells).

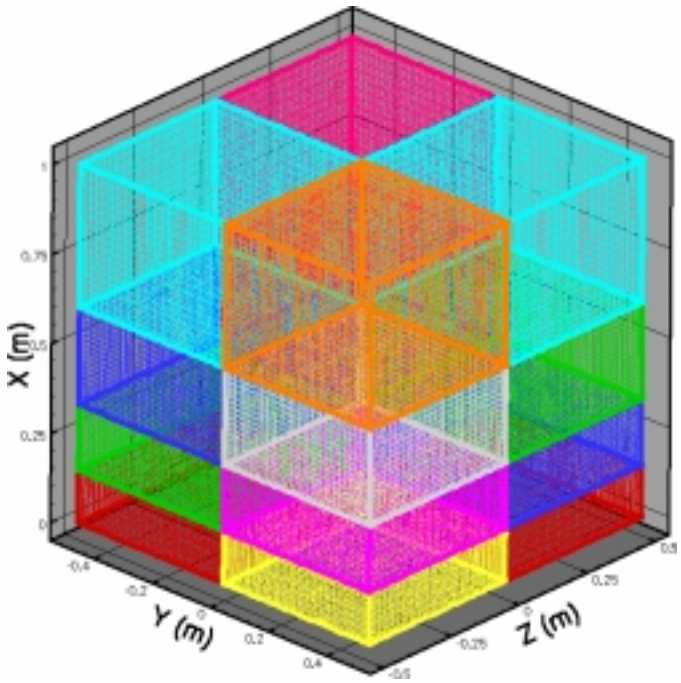

Figure 10: 3-D structured LES grid (80x65x65) with 16 processor domain decomposition.

3.8.2.1 2-D (Axisymmetric) MPSalsa LES Model The axisymmetric MPSalsa LES model uses a Galerkin Least-Squares finite element method to solve the filtered Navier-Stokes equations on an unstructured grid shown in Figure 8. MPSalsa [69] uses equal order pressure and velocity interpolation and provides SUPG-type stabilization. A second order Adams-Bashforth/trapezoidal rule time integration is used. The axisymmetric equations are solved in a fully coupled manner using an inexact Newtons method. The grid consists of 5774 quadrilateral elements and uses linear basis functions. The simulations were run in parallel using either 8 or 32 processors.

3.8.2.2 2-D (Axisymmetric) RANS Model The RANS model solves the Navier-Stokes equations in finite volume form using the standard high-Reynolds number k-ϵ model to provide turbulence closure. The convective terms are discretized with the second order LDFSS upwind flux-difference splitting scheme of Edwards [18], while the diffusion terms are discretized with central differences. First-order time accuracy is used to advance the solutions to a steady-state. This model uses a fully compressible formulation with local time-derivative preconditioning [19] to alleviate the stiffness due to disparity between acoustic and convective time scales. Characteristic-based boundary conditions are used at the inflow and outflow boundaries. Solutions are obtained on three mesh levels (24x24,48x48,and 96x96 cells) in order to assess grid convergence. In order to achieve a steady-state solution, the spatial accuracy of the RANS simulations was reduced from second order to first order. Richardson

Extrapolation was used for the fine and medium grid levels in order to provide nominally second order accurate temperature and stream-wise velocity profiles. Unsteady RANS solutions were not attempted in this paper. The coarse grid is shown in Fig. 3.

3.8.2.3 3-D LES Model The 3-D LES model solves the filtered Navier-Stokes equations on a structured finite volume grid. A fifth-order upwind biased stencil is used for momentum [43], while a fifth order Essentially Non-Oscillatory (ENO) scheme [70] is used for the energy and species equations. The equations are integrated in time with a fourth order Runge-Kutta scheme. Pressure gradient scaling [65] is used to provide temporal stability for these low mach number flows. Sub-Grid Scale (SGS) modeling of momentum is achieved with the dynamic Smagorinsky model [24] while the SGS diffusion of mass and energy uses a dynamic gradient diffusion model [13]. The size is 80x65x65 grid cells or approximately 340,000 grid nodes. The simulations were run on 16 processors using MPI and domain decomposition. The grid and domain decomposition is shown in Fig. 5

3.8.2.4 Boundary Conditions The liquid fuel flow rate in the experiment was measured to be 1.35x10^{-6} m/s (1.35 cm^3/s), which corresponds to an effective average gas-phase velocity of 0.0164 m/s (1.64 cm/s). This time-averaged value was applied over the entire pool surface, thus local variations in the fuel vaporization rate were neglected. The axial velocity in the air stream (x = 0) was chosen as 0.001 m/s (0.1 cm/s) to provide a small co-flow stream for numerical stability. The time-averaged temperature specified from the experimental data in the fuel and air streams is 723.15 K and 300 K, respectively, and atmospheric pressure was imposed on all boundaries.

3.8.3 Combustion Models

The combustion models used in the current work are based on simple strained laminar flamelet models (SLFM) using assumed probability distribution functions (PDF). The chemistry is based on using an infinitely fast single-step methanol reaction of the form:

$$\nu_F CH_3OH + \nu_{O_2}(3.76N_2 + O_2) \rightarrow \nu_{CO_2} CO_2 + \nu_{H_2O} H_2O + \nu_{O_2} 3.76N_2 \tag{3.12}$$

The motivation for using infinitely fast chemistry is to obtain simple analytical expressions (i.e. computationally efficient) for combustion that will predict the overall heat release and products of major gas species. These approximations are considered reasonable for pool fire simulations where strong extinction and reignition events are rare. Under these assumptions the species may be written as functions of the mixture fraction only, i.e. $Y_s = Y_s(z)$. This expression can then be substituted in for the transport equation for Y_s leading to the following expression for reaction rate:

$$\dot{\omega}_s = -\frac{1}{2}\rho\chi\frac{d^2Y_s}{dz^2} \tag{3.13}$$

where χ is defined as the scalar dissipation rate. For a turbulent flow field the subgrid scale combustion environment is envisioned as an ensemble of smaller laminar flames or flamelets. The average chemical production rate may then be found by integrating Eq. (3.13) over the joint PDF of mixture fraction and scalar dissipation rate, $P_{Z\chi}$.

$$\overline{\dot{\omega}_s} = -\frac{1}{2}\int_0^{\chi_{max}}\int_0^1 P_{Z\chi}\rho(\zeta)\chi\frac{d^2Y_s(\zeta)}{d\zeta^2}d\zeta d\chi \tag{3.14}$$

The interpretation of $P_{Z\chi}$ for RANS calculations is different than it is for LES. For RANS, $P_{Z\chi}$ represents the probability of finding a value of Z and χ at a particular point in space over all time. For LES, the joint PDF represents the probability of finding Z and χ in a subgrid volume weighted by a filtering function at a particular point in space and time.

Two different assumed PDF approaches to evaluating Eq. (3.14) were explored in this study. In the first approach, (denoted as SLFM1) statistical independence is assumed between the mixture fraction and the scalar dissipation rate. In this case, the time averaged (for RANS) or filtered (for LES) chemical production rate becomes:

$$\overline{\dot{\omega}_s} = -\frac{1}{2}\bar{\chi}\int_0^1 P_Z(\zeta)\rho(\zeta)\frac{d^2Y_s(\zeta)}{d\zeta^2}d\zeta \tag{3.15}$$

Experience showed that the predictions using the SLFM1 model tended to underpredict the extent of heat release (and subsequently the temperatures and stream-wise velocities are too low), and it was believed that this was a consequence of the statistical independence assumption (as will be discussed more below). To address this shortcoming, a second model (denoted as SLFM2) was developed and applied in which statistical independence is not assumed. The model is derived by starting with the PDF transport equation for mixture fraction and assuming constant density flows with equal and constant diffusivities. Details of the derivation are given in [16], and yield the following analytical expression for the mean reaction rate:

$$\overline{\dot{\omega}_s} = -\frac{1}{2}C_s\bar{\rho}(z_{st})\frac{DF(Z_{st})}{Dt} \tag{3.16}$$

where $\frac{DF(Z_{st})}{Dt}$ is a Lagrangian derivative that requires explicit calculation locally in space for the RANS and both time and space for the LES.

In addition, the filtered mass fraction is required for computation and found by simply integrating the state relationship over the PDF of mixture fraction, i.e.:

$$\tilde{Y}_s = \int_0^1 P_Z(\zeta)Y_s(\zeta)d\zeta. \tag{3.17}$$

In this study, the assumed shape of the PDF was chosen to be a beta function, which leads to

$$\overline{\dot{\omega}_s} = -\frac{\bar{\rho}\bar{\chi}}{2}\frac{\Gamma(\beta_1+\beta_2)}{\Gamma(\beta_1)\Gamma(\beta_2)}(b_2-b_1)z_{st}^{\beta_1-1}(1-z_{st})^{\beta_2-1} \tag{3.18}$$

for the filtered chemical production rate in case SLFM1, and

$$\overline{\dot{\omega}_s} = \frac{1}{2}(b_2-b_1)\bar{\rho}(z_{st})\frac{D}{Dt}\int_0^{Z_{st}} I_\beta(\xi,\beta_1,\beta_2)d\xi \tag{3.19}$$

for the filtered chemical production rate in case SLFM2.

The assumed beta PDF requires the specification of the mean mixture fraction and the subgrid variance. For the LES approach, a scale similarity model is used [14]:

$$\widetilde{z''^2} = \sigma_z^2 = (\widetilde{\tilde{z}\tilde{z}} - \tilde{\tilde{z}}\tilde{\tilde{z}}) \tag{3.20}$$

For the RANS calculations, a transport equation is solved for the mixture fraction variance

$$\frac{\partial\sigma_z^2}{\partial t} = \frac{\partial}{\partial x_j}(\bar{\rho}\tilde{u}_j\sigma_z^2) = P - D - \bar{\rho}\bar{\chi_f} \tag{3.21}$$

where P is a production term and D represents diffusion due to turbulent fluctuations.

3.8.4 Results and Discussion

The mean reaction rate models based on Eqs. (3.18) and (3.19) are run for both the axisymmetric and 3D LES while just the former is used in the RANS calculations. Predictions of time-averaged temperature and stream-wise velocity are compared to experimental data at heights of 0.02, 0.14 and 0.30 m above the pool surface to assess code (i.e. 2D versus 3D and RANS versus. LES) and combustion model(i.e. SLFM1 versus SLFM2) performance. For the LES cases, time-averaged quantities are obtained by first allowing for initial time dependent transients to wash out of the computational domain and then statistics are collected over several (5-10) puff cycles for which the flow is considered statistically stationary.

3.8.4.1 Time-averaged Temperature using SLFM1 Figures 8 through 10 present comparisons of time-averaged temperature for the three specified heights using SLFM1. At 0.02 m above the surface (Fig.8) the time-averaged temperature is under-predicted in all cases. At 0.14 m both LES approaches essentially give a mixing solution with very little heat release. The RANS approach shows good agreement with the data at the x=0.14 m location, but under-predicts the mixing and hence the combustion at the centerline.

Fig.10 shows time-averaged temperature at 0.30 m above the pool surface. The RANS approach greatly over-predicts the temperature while the LES cases greatly underpredict by almost a half.

3.8.4.2 Time-averaged Velocity using SLFM1 Time-averaged profiles of axial velocity are extracted from the simulations and compared with experimental data at all three heights and presented in Figs. 11 through 13. At 0.02 m, the axial velocities are very near to the inflow values. At 0.14 m above the pool surface, the RANS model shows better agreement with the data, while LES approaches under-predict the stream-wise velocity, consistent with the temperature profile at the same location. The velocity trends in Fig.13 (0.30 m) are consistent with the temperature profiles from Fig. 10. The RANS model over-predicts the axial velocity, while the 2D and 3D LES cases greatly underpredict by as great as a factor of 10.

In general,the behavior of the velocity field is closely linked to that of the temperature field. Temperature pro- files from the LES model using the standard form of the flamelet model fall significantly below the experimental values, which then leads to an under-prediction of the stream-wise velocity. The heat release from the RANS model is larger than that seen in the experiment, leading to an over-prediction of the axial flow velocity. These discrepancies indicate that the assumptions used to develop SLFM1 are not well founded for this class of flows and an alternative model needs to be developed.

One of the main weaknesses in SLFM1 is the assumption of statistical independence between Z and X. This assumption is generally valid for highly turbulent flows but breaks down in transitionally turbulent flows such as the very near field of a turbulent jet [23] and so is also questionable for the transitionally turbulent pool fire flows in this study. In order to explore this assumption, a second combustion model is developed based on using the PDF transport equation of mixture fraction and makes no assumption regarding the statistical independence of Z and X outlined previously in the Combustion Models section. Results using this new model are presented next for the 2D and 3D LES.

3.8.4.3 Time-averaged Temperature using SLFM2 Figures 14 through 16 present results of time-averaged temperature profiles at all three downstream locations from the 2D and 3D LES. The results show significant improvement using the new combustion model (SLFM2). The axisymmetric LES tends to underpredict the temperature near the centerline at all downstream locations and overpredict for $r > 0.04$ m at the $x = 0.3$ m location. The 3D LES overpredicts near the toe of the pool fire flame (i.e. $r = 0.15$ m) at $x = 0.0$ m but agrees reasonably well with the experiment at the other further downstream locations.

The most notable difference between the 2D-axisymmetric LES and the 3D LES is the strong bimodal shape of the 2D LES at the 0.0 and 0.30 m downstream locations that do not appear in either the 3D LES nor the experimental data. The reason for this can be attributed to the axisymmetric assumption that doesnt allow for any stream-wise vorticity to be generated. This is evident by comparing Figs. 17 and 18 showing representative snapshots of temperature contours from 2D and 3D LES flow fields, respectively. In the axisymmetric LES, two distinct flow regions are observed near the base of the plume. The first region,

Source	Frequency (Hz)
Experiment	2.8
Correlation [10]	2.7
2D LES, SLFM1	3.1
2D LES, SLFM2	2.9
3D LES, SLFM1	1.8
3D LES, SLFM2	2.5

Table 1. Computed and Experimental Puffing Frequencies.

near the plume centerline, consists of relatively high velocity that is being drawn upwards due to a previous puffing event. The second region is located away from the centerline and consists of slower moving fluid and a large toroidal vortical structure that was formed due to the presence of baroclinic torque. These two predominant flow features give rise to the bimodal shape observed in the time-averaged temperature profiles. In contrast, these structures are not as distinct in 3D LES of Fig. 18 due to the generation of stream-wise vorticity that rapidly mixes the flow. The generation of stream-wise vorticity gives rise to finger-like instabilities often observed in pool fires and shown in the experimental images of Fig. 2. These structures are also observed in the 3D LES as illustrated in Fig. 19 showing an isocontour plot of vorticity magnitude.

3.8.4.4 Time-averaged Velocity using SLFM2 Figures 20 through 22 present time-averaged stream-wise velocity comparisons using SLFM2. Good agreement is shown with comparison to experiment for both the 2D and 3D LES. Consistent with the temperature profiles, the 2D LES exhibits a strong bi-modal behavior at the 0.14 m and 0.30 m downstream locations due to the lack of secondary mixing previously noted.

3.8.4.5 Puffing Frequency Lastly, the puffing frequencies were determined from the unsteady LES calculations using both combustion models and presented in Table 1. Frequencies reported from the experiment and from simple Richard number based correlations of Ref [10] are also tabulated. In all of the LES cases, better agreement to the experimental data and correlation were obtained using SLFM2, consistent with the improved time-averaged velocity and temperature predictions.

3.8.5 Summary and Conclusions

For pool fires, the velocity and temperature fields are tightly coupled. If the net amount of heat release is under-predicted, then the buoyant forces which drive the flow will be reduced leading to a subsequent reduction in the stream-wise velocity. This strong coupling between the temperature and velocity fields requires accurate predictions of the subgrid combustion processes. In this study, two different SLFM-based combustion models with assumed PDF were explored using 2D RANS, 2D LES and 3D LES codes. The use of SLFM1 resulted in poor predictions of time-averaged temperature and stream-wise velocity for all cases. This behavior is attributed to the assumption of statistical independence between mixture fraction and its dissipation rate. This realization resulted in the development of a second combustion model (SLFM2) that does not make use of the statistical independence assumption. The use of this model resulted in substantiality better predictions of time-averaged temperature and velocity as well as puffing frequency for both the 2D and 3D LES. Lastly, a bimodal distribution is observed in the 2D LES and is attributed to the absence of stream-wise vorticity generation in the axisymmetric formulation that enhances secondary mixing.

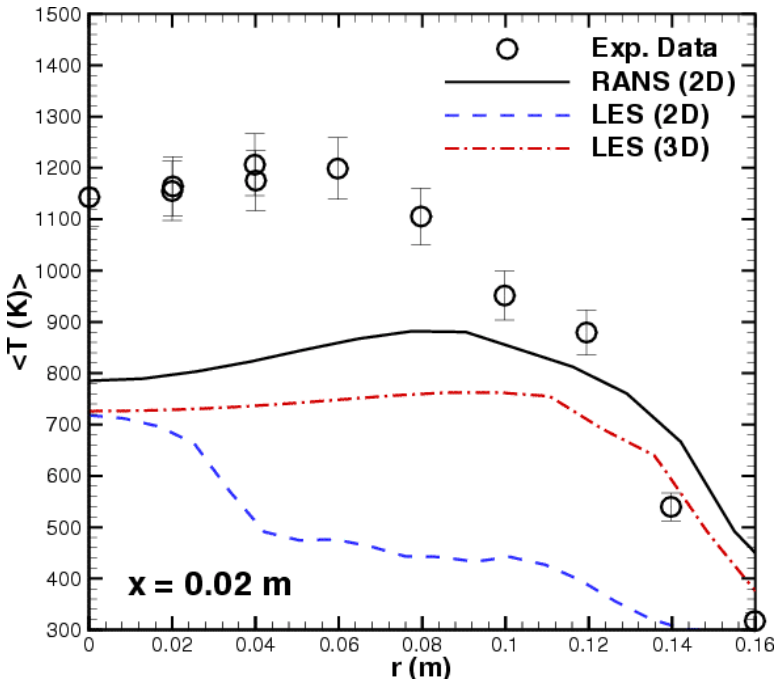

Figure 11: Time-averaged temperature profiles 0.02 m above the pool.

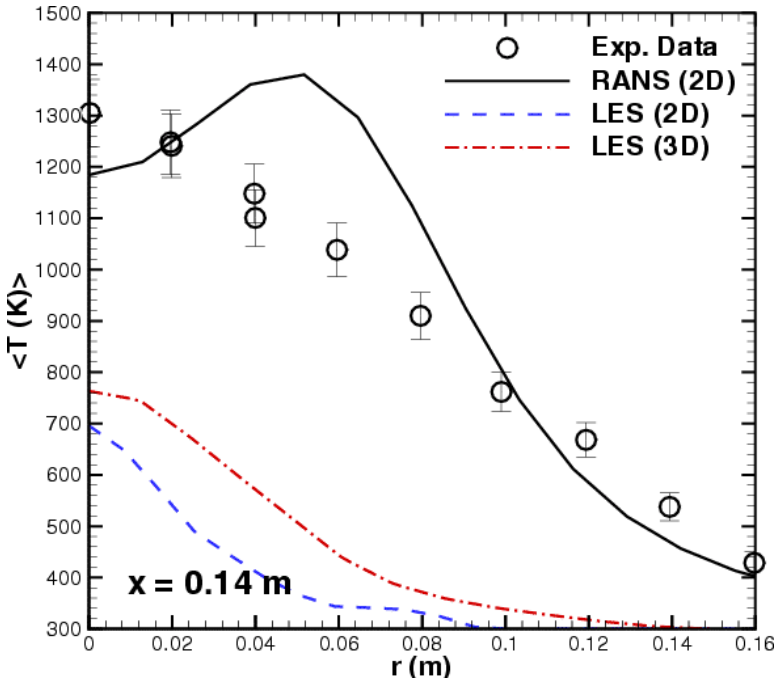

Figure 12: Time-averaged temperature profiles 0.14 m above the pool.

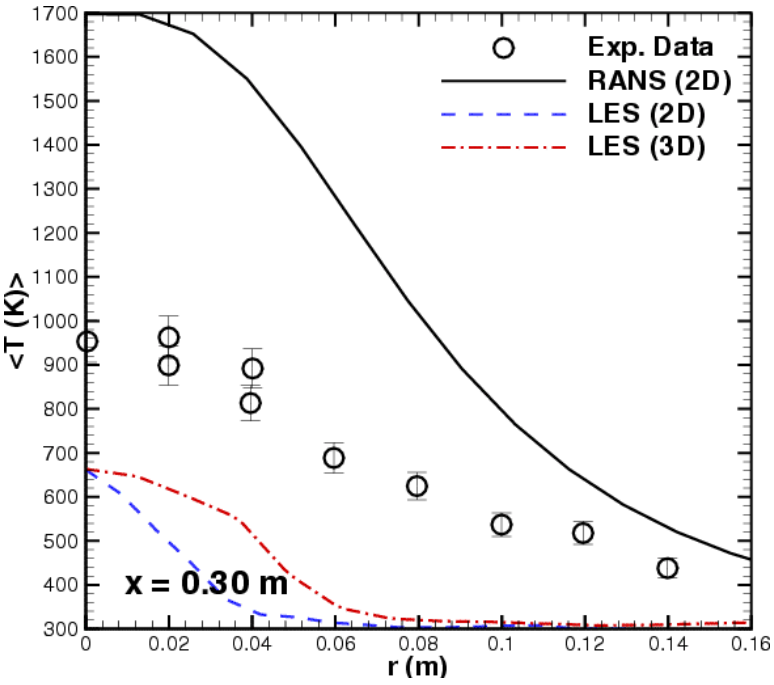

Figure 13: Time-averaged temperature profiles 0.30 m above the pool.

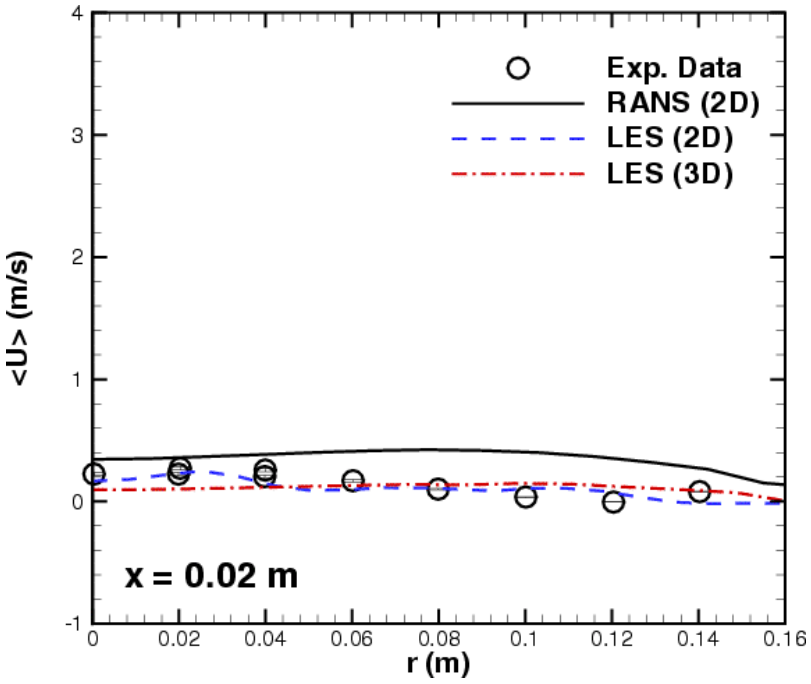

Figure 14: Time-averaged axial velocity profiles 0.02 m above the pool.

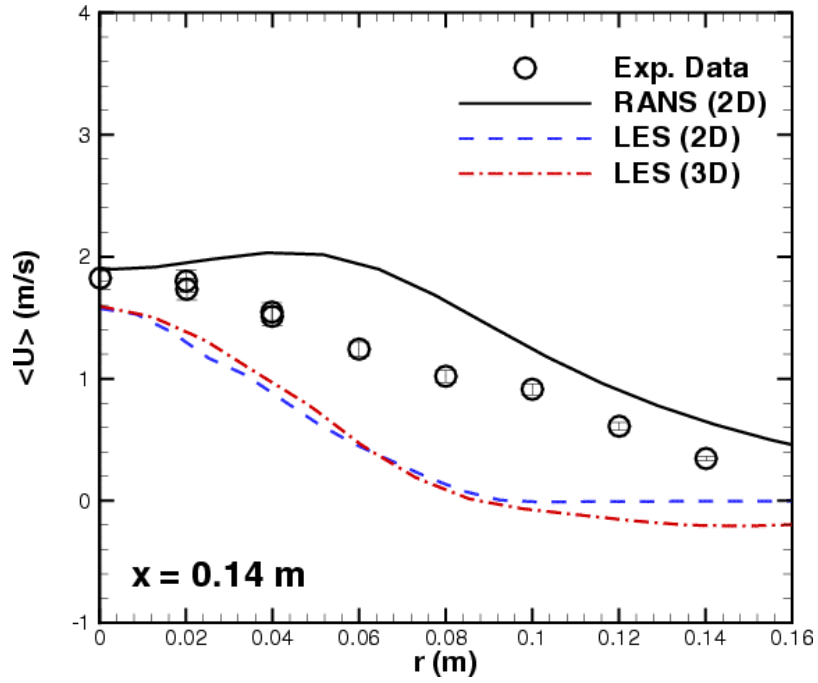

Figure 15: Time-averaged axial velocity profiles 0.14 m above the pool.

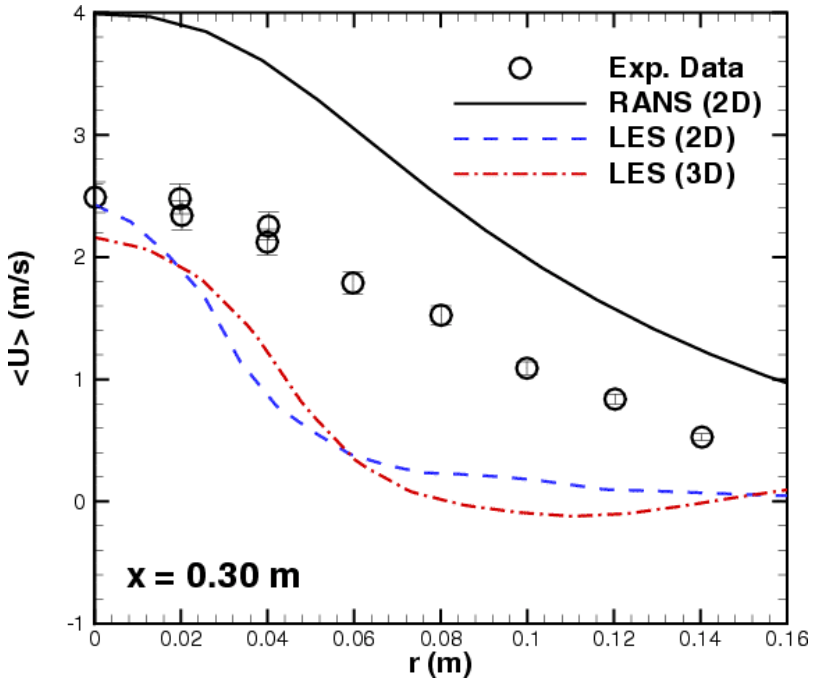

Figure 16: Time-averaged axial velocity profiles 0.30 m above the pool.

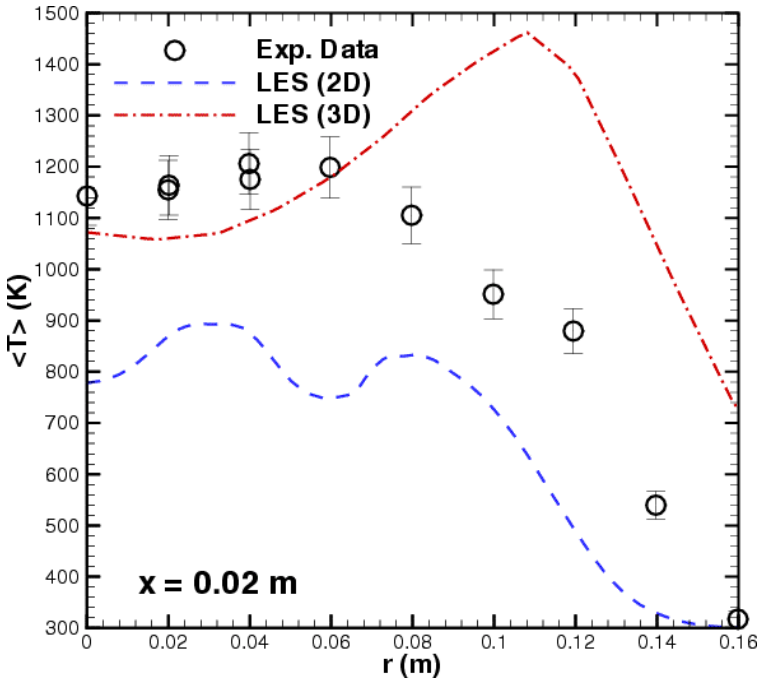

Figure 17: Time-averaged temperature profiles 0.02 m above the pool for SLFM2.

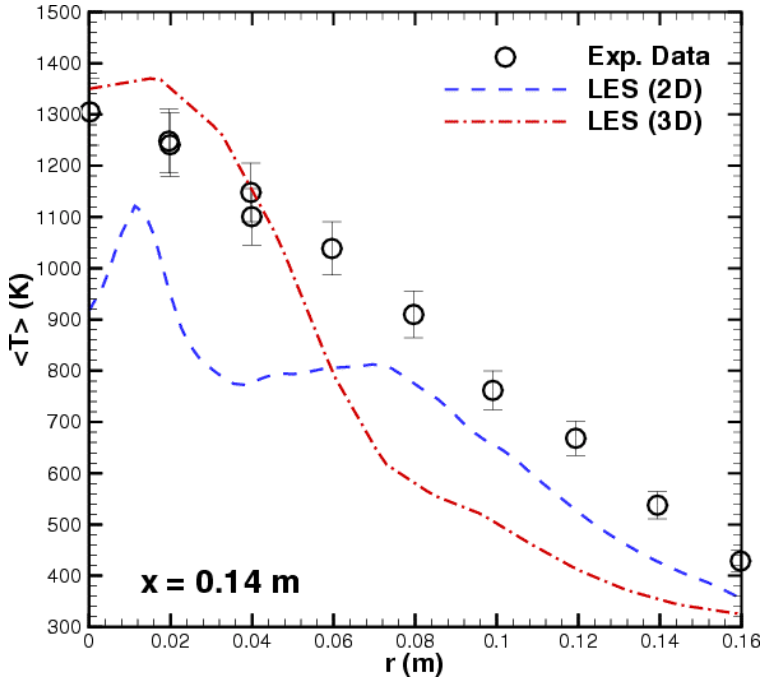

Figure 18: Time-averaged temperature profiles 0.14 m above the pool for SLFM2.

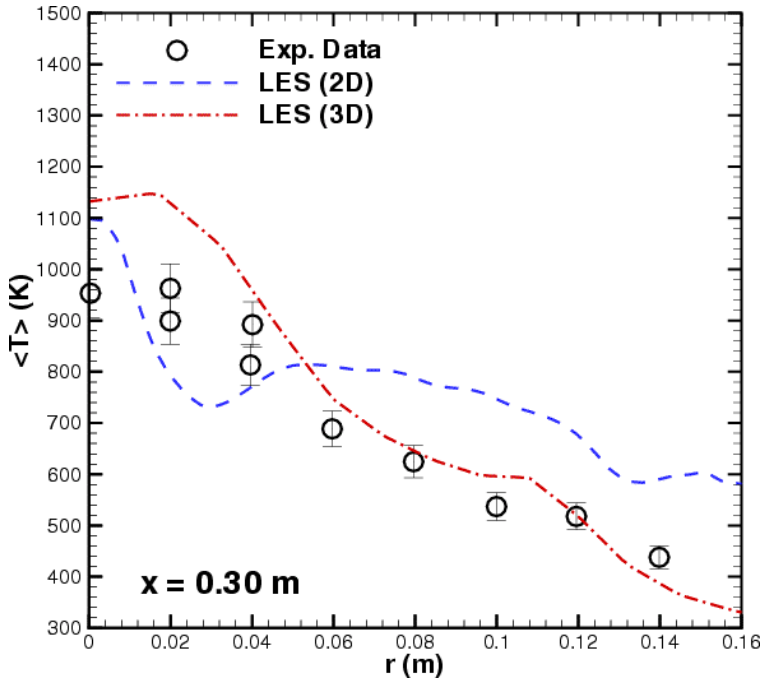

Figure 19: Time-averaged temperature profiles 0.30 m above the pool for SLFM2.

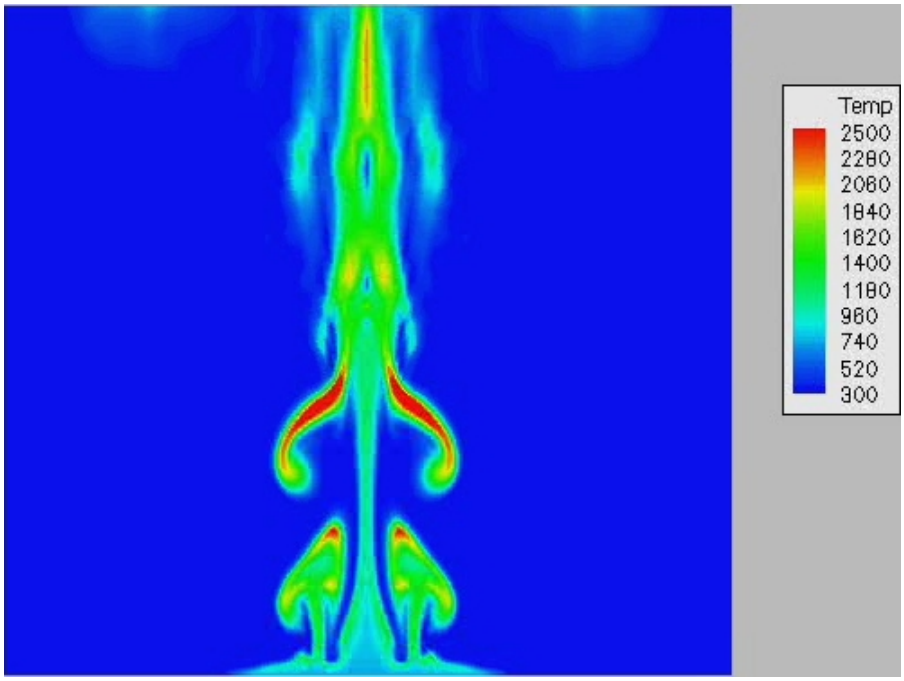

Figure 20: Instantaneous snapshot showing temperature contours from 2D axisymmetric LES.

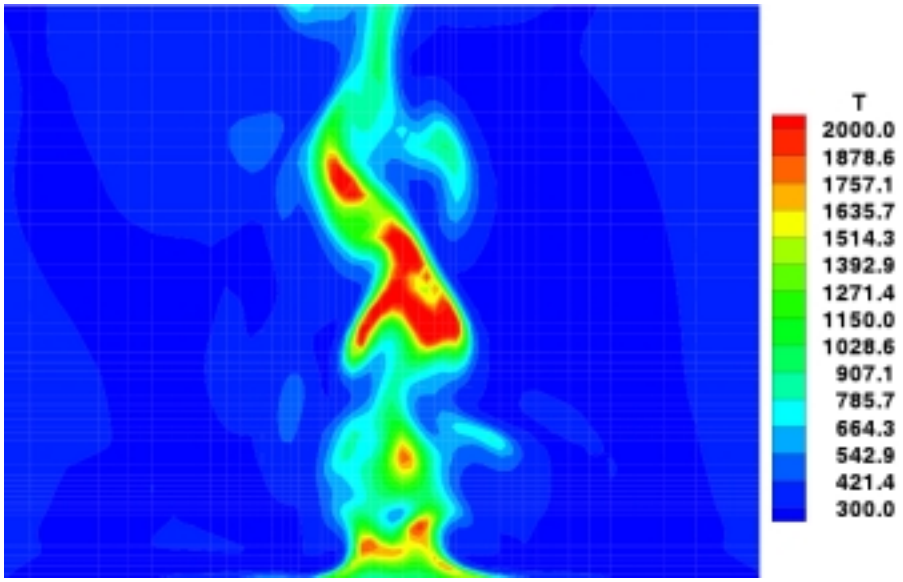

Figure 21: Instantaneous snapshot showing temperature contours from 3D LES at a slice through the centerline.

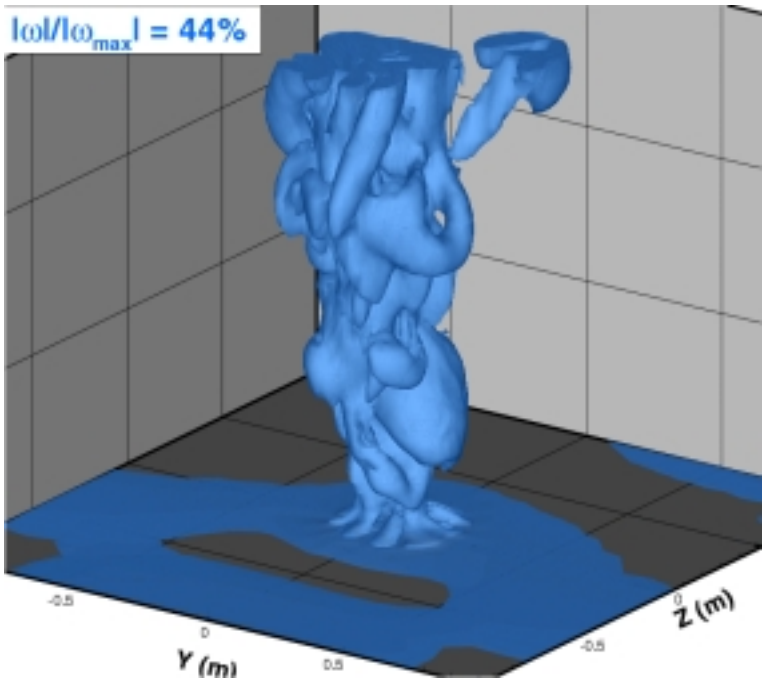

Figure 22: Instantaneous snapshot showing vorticity magnitude at 44 percent of maximum from 3D LES.

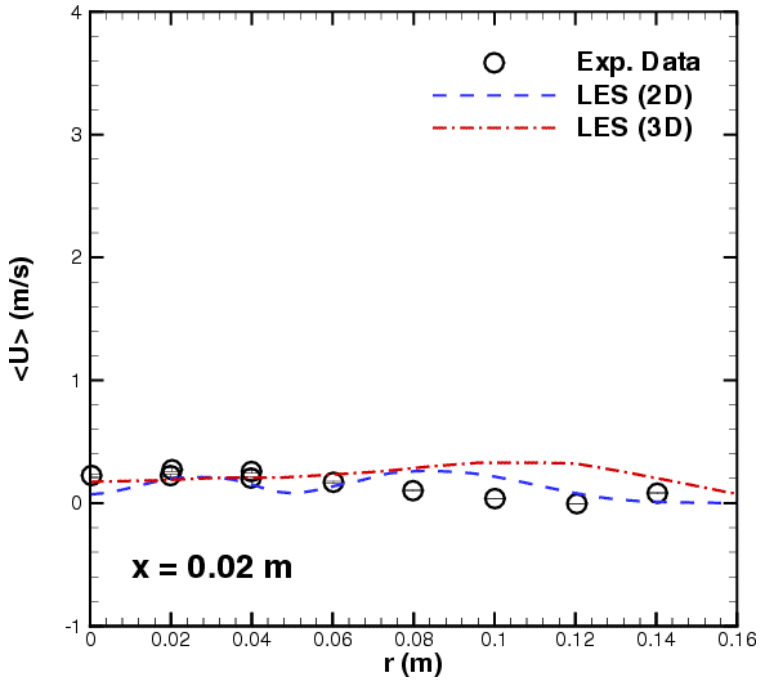

Figure 23: Time-averaged axial velocity profiles 0.02 m above the pool for SLFM2.

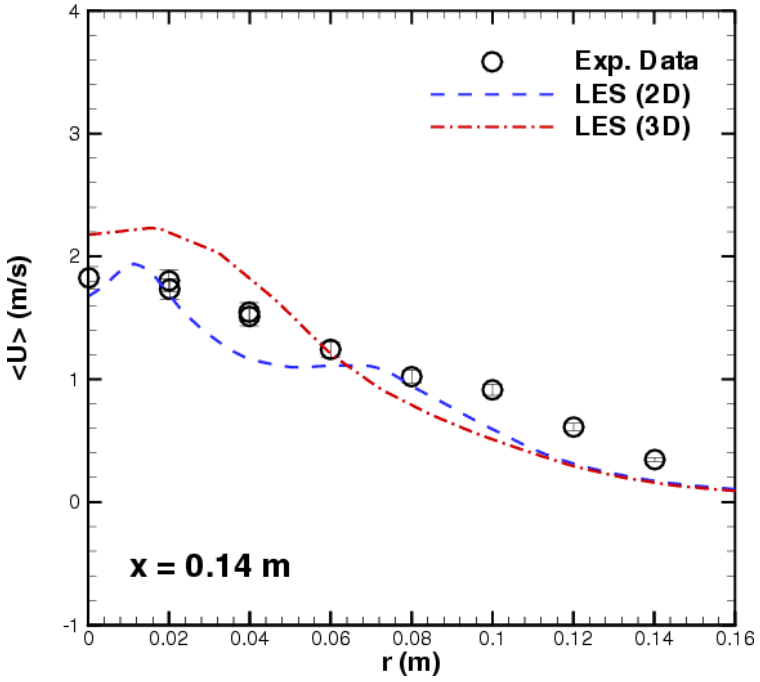

Figure 24: Time-averaged axial velocity profiles 0.14 m above the pool for SLFM2.

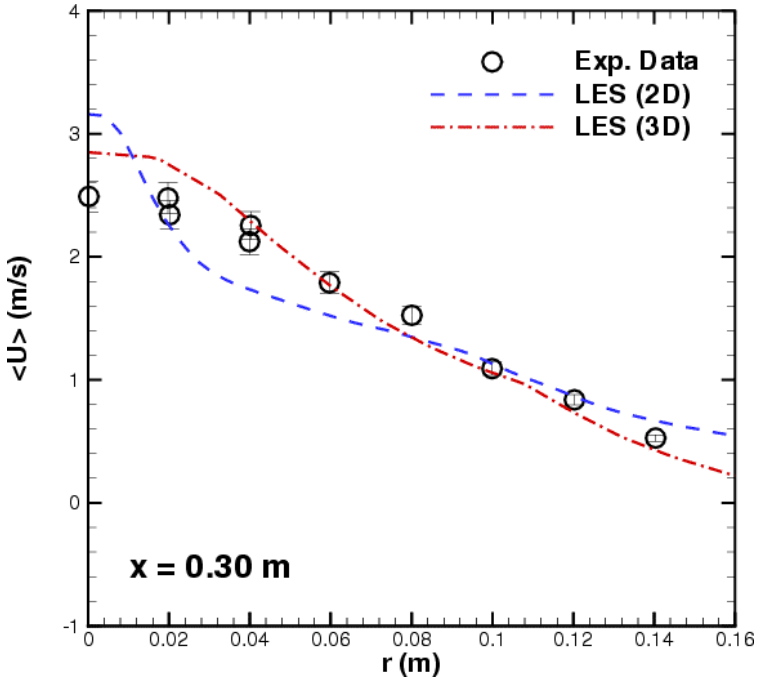

Figure 25: Time-averaged axial velocity profiles 0.30 m above the pool for SLFM2.

4 An LES near-wall subgrid model based on ODT

In section 2.7, a brief description of the near-wall resolution problem was given, and it was noted that although various models have been proposed, significant limitations remain. In this section we describe the development and testing of a novel new approach to the near-wall LES closure problem that is based on coupling the ODT model of Kerstein to LES. In the near-wall region, finely resolved ODT lines are embedded within a coarse LES mesh and the ODT evolution equations capture fine-scale temporal and spatial variations (in one direction) of the three-component velocity field. Near-wall turbulent transport is modeled through the combined effect of a sequence of fluid-element rearrangements (called eddy events), without the introduction of an eddy viscosity. LES/ODT coupling is bi-directional and occurs both through the direct calculation of the subgrid turbulent stress by temporally and spatially filtering the ODT-resolved momentum fluxes (up-scale coupling), and through the LES-resolved mean pressure and velocities impacting the ODT behavior (down-scale coupling). The overall goal of this research is to develop and demonstrate a method that avoids the overwhelming computational expense of a finely resolved 3D mesh in the near-wall region, and yet provides well-resolved near-wall dynamic behavior for high-Reynolds number wall-bounded flows.

4.1 Overview of ODT

ODT can be viewed as a method for simulating, with spatial and temporal resolution comparable to direct numerical simulation (DNS), the evolution of the velocity vector and fluid properties along a one-dimensional (1D) line of sight through a 3D turbulent flow. ODT is an outgrowth of the linear-eddy model [34], in which fluid motions are prescribed without explicit introduction of a velocity field. The first ODT formulation [35] involved simulation of a single velocity component evolving on a line. A more recent formulation [36] introduced the evolution of the three-component velocity vector on the 1D domain. Generalization to treat variable-density effects dynamically is in progress. For the work described in this paper the formulation described in [36] is adopted as a starting point. Only an abbreviated description of the model is included here, with constant density assumed for simplicity, and the emphasis is on those aspects most relevant to the LES subgrid model described later. In addition, the numerical implementation of ODT for stand-alone calculations (i.e. no multi-dimensional grid, a single ODT line spanning the channel) of turbulent channel flow is briefly described, together with representative results, in order to give context to its more restricted use as a subgrid model.

4.1.1 Modeling Approach

The version of ODT utilized here describes the evolution of a three-component vector velocity field $v_i(y,t)$ defined on a one-dimensional domain (parameterized by the spatial coordinate y, corresponding to the direction $i = 2$). Additional scalar fields $\theta(y,t)$ may also be defined in the model, but are not implemented here.

The fields defined on the 1D domain evolve by two mechanisms, molecular evolution and a stochastic process (probabilistically driven by a simple physical model) representing turbulent stirring. The stochastic process consists of a sequence of events, each of which involves an instantaneous transformation of the velocity and scalar fields. During the time interval between each event and its successor, molecular evolution occurs, governed by the equations

$$\left(\partial_t - \nu\partial_y^2\right) v_i(y,t) = 0 \tag{4.1}$$

$$\left(\partial_t - \kappa\partial_y^2\right) \theta(y,t) = 0, \tag{4.2}$$

where ν is the kinematic viscosity and κ is the scalar diffusivity.

The events representing turbulent stirring may be interpreted as the model analog of individual turbulent eddies. In what follows, these events are termed 'eddy events' or simply eddies. This terminology reflects the fact that each event is characterized by three properties, a length scale, a time scale, and a measure of kinetic energy, and that a key physical input to the model is a postulated relationship among these quantities that is analogous to the usual dimensional relationship applied to individual turbulent eddies.

The turbulent stirring submodel is specified by defining the mathematical operations performed during an eddy event and by formulating the rules that govern the selection of events. Conceptually, the eddy definition is the model representation of flow kinematics (i.e., fluid advection and flow-field response to forcings), while rules governing the stochastic selection of events reflect the dynamics that drive the eddy motions. Because turbulent stirring is implemented as an event sequence rather than a continuous process, the velocity field does not directly prescribe the fluid motions. Motions and velocities are nevertheless closely linked through the dynamics embodied in the event selection rules.

In the current formulation, an eddy event consists of two mathematical operations. One is a measure-preserving map representing the fluid motions associated with a notional turbulent eddy. The other is a modification of the velocity profiles in order to implement energy transfers prescribed by the dynamical rules. These operations are represented symbolically as

$$\begin{aligned} v_i(y) &\rightarrow v_i(f(y)) + c_i K(y) \\ \theta(y) &\rightarrow \theta(f(y)). \end{aligned} \tag{4.3}$$

According to this prescription, fluid at location $f(y)$ is moved to location y by the mapping operation, thus defining the map in terms of its inverse $f(y)$, which is convenient for present

purposes. This mapping is applied to all fluid properties. The additive term $c_i K(y)$, affecting only the velocity components, is used to capture pressure-induced energy redistribution among velocity components.

The functional form chosen for $f(y)$, called the 'triplet map,' is the simplest of a class of mappings that satisfy the physical requirements of measure preservation (the nonlocal analog of vanishing velocity divergence), continuity (no introduction of discontinuities by the mapping operation), and scale locality (at most order-unity changes in property gradients). The first two requirements are fundamental properties. The requirement of scale locality is based on the well-established empirical principle that length-scale reduction in a turbulent cascade occurs by a sequence of small steps (corresponding to notional turbulent eddies), causing down-scale energy transfer to be effectively local in wavenumber.

Mathematically, we can define the triplet map as

$$f(y) \equiv y_0 + \begin{cases} 3(y-y_0) & \text{if } y_0 \le y \le y_0 + \frac{1}{3}l, \\ 2l - 3(y-y_0) & \text{if } y_0 + \frac{1}{3}l \le y \le y_0 + \frac{2}{3}l, \\ 3(y-y_0) - 2l & \text{if } y_0 + \frac{2}{3}l \le y \le y_0 + l, \\ y - y_0 & \text{otherwise.} \end{cases} \tag{4.4}$$

This mapping takes a line segment $[y_0, y_0 + l]$, shrinks it to a third of its original length, and then places three copies on the original domain. The middle copy is reversed, which maintains the continuity of advected fields and introduces the rotational folding effect of turbulent eddy motion. Property fields outside the size-l segment are unaffected.

In Eq. (4.3), K is a kernel function that is defined as $K(y) = y - f(y)$, i.e., its value is equal to the distance the local fluid element is displaced. It is non-zero only within the eddy interval, and it integrates to zero so that energy redistribution does not change the total (y-integrated) momentum of individual velocity components (here assuming constant density).

The amplitudes c_i in Eq. (4.3) are determined for each eddy individually according to a model (designed to capture pressure-scrambling effects) that changes the kinetic energy of individual velocity components, defined by

$$E_i \equiv \frac{1}{2}\rho \int v_i^2(y)\,\mathrm{d}y, \tag{4.5}$$

while keeping the total kinetic energy $E \equiv \sum_i E_i$ constant. (The density ρ, assumed constant, is defined here as mass per unit length.) Consider the change in the kinetic energy of component i due to the implementation of an eddy event. According to Eq. (4.3), the energy change is

$$\Delta E_i = \frac{1}{2}\rho \int \left[(v_i(f(y)) + c_i K(y))^2 - v_i(y)^2\right] \mathrm{d}y = \rho l^2 c_i \left(v_{i,K} + \frac{2}{27} l c_i\right), \tag{4.6}$$

where we have used the identity $\int K^2(y)\,\mathrm{d}y = \frac{4}{27}l^3$ and the definition

$$v_{i,K} \equiv \frac{1}{l^2}\int v_i(f(y))K(y)\,\mathrm{d}y = \frac{4}{9l^2}\int_{y_0}^{y_0+l} v_i(y)[l-2(y-y_0)]\,\mathrm{d}y. \tag{4.7}$$

The rightmost expression in Eq. (4.7) follows from the definitions of $f(y)$ and $K(y)$. The requirement $\sum_i \Delta E_i = 0$ implies only one constraint on the three amplitudes c_i.

Further modeling to determine the three amplitudes is based on the following observation. c_i for given i can be chosen so as to add an arbitrarily large amount of kinetic energy to component i, but the maximum amount that can be removed is a finite value,

$$Q_i \equiv \frac{27}{8}\rho l v_{i,K}^2. \tag{4.8}$$

The amounts Q_i available for removal by the kernel mechanism are the basis of an energy-redistribution procedure motivated by the tendency of turbulent eddies to drive the flow toward isotropy. Namely, the energy changes

$$\Delta E_i = \frac{\alpha}{2}(Q_j + Q_k - 2Q_i) \tag{4.9}$$

are applied, where α is a model parameter and (i,j,k) is any permutation of the component indices $(1,2,3)$. The value $\alpha = \frac{2}{3}$ corresponds to equipartition of the available energy among velocity components and is used to obtain the results presented here. Ref. [36] considers the effect of setting $\alpha = 1$, which maximizes the intercomponent energy transfer. Although this choice has an impact on some velocity statistics, it is found that properties of interest here are not very sensitive to the choice of α.

With Q_i given by Eq. (4.8), the exchange amplitudes c_i are evaluated by solving Eq. (4.6) and using Eqs. (4.8) and (4.9) to obtain

$$c_i = \frac{27}{4l}\left(-v_{i,K} + \mathrm{sgn}(v_{i,K})\sqrt{(1-\alpha)v_{i,K}^2 + \frac{\alpha}{2}(v_{j,K}^2 v_{j,K}^2)}\right), \tag{4.10}$$

where the sign ambiguity in solution to the quadratic equation for c_i is resolved by requiring that $c_i \to 0$ as $\alpha \to 0$. Where necessary, initial conditions are seeded with small random perturbations to resolve the sign ambiguity in a manner that does not bias the flow evolution.

4.1.2 Eddy Selection

The final ingredient required in the model is the determination of the time sequence of eddy events, individually parameterized by position y_0 and size l, that are implemented. In ODT, eddy events are implemented instantaneously, but should occur with frequencies comparable to the turnover frequencies of corresponding turbulent eddies. Events are therefore determined by sampling from an event rate distribution that reflects the physics governing eddy turnovers. A key feature of this distribution is that it is based on the instantaneous state of the flow, and thus evolves in time as the flow evolves.

At each instant in time, the event rate distribution is defined by first associating a time scale $\tau(y_0, l)$ with every possible eddy event. (Note that $\tau(y_0, l)$ is analogous to the eddy turnover time as usually defined, but is based on the instantaneous velocity profiles $v_i(y, t)$.) To this end, the quantity l/τ is interpreted as an eddy velocity and $\rho l^3/\tau^2$ is interpreted as a measure of the energy of eddy motion. To determine τ, this energy is equated to an appropriate measure of the eddy energy based on the current flow state. For reasons explained elsewhere [36], the energy measure that is used is the available energy of the $i = 2$ velocity component upon completion of eddy implementation, minus an energy penalty that reflects viscous dissipation effects. The energy penalty introduces a threshold Reynolds number that must be exceeded for eddy turnover to be allowable.

Based on these considerations, we use the relationship

$$\left(\frac{l}{\tau}\right)^2 \sim (1-\alpha)v_{2,K}^2 + \frac{\alpha}{2}(v_{1,K}^2 + v_{3,K}^2) - Z\frac{\nu^2}{l^2} \tag{4.11}$$

to determine τ, where the coefficient Z in the viscous penalty is an order-unity parameter of the model.

Given Eq. (4.11), the time scales τ for all possible eddies can be translated into an event rate distribution λ, defined as

$$\begin{aligned}\lambda(y_0, l; t) &\equiv \frac{C}{l^2\tau(y_0, l; t)} \\ &= \frac{C\nu}{l^4}\sqrt{(1-\alpha)\left(\frac{v_{2,K}l}{\nu}\right)^2 + \frac{\alpha}{2}\left[\left(\frac{v_{1,K}l}{\nu}\right)^2 + \left(\frac{v_{3,K}l}{\nu}\right)^2\right] - Z},\end{aligned} \tag{4.12}$$

where C is an adjustable parameter that controls the overall event frequency. If the right-hand side of Eq. (4.11) is negative, the eddy is deemed to be suppressed by viscous damping and λ is taken to be zero for that case. In the square root term of Eq. (4.12), the quantities preceding Z involve groups that have the form of a Reynolds number. Z can be viewed in this context as a parameter controlling the threshold Reynolds number for eddy turnover.

The foregoing construction of the event rate distribution involves three free parameters: C, α, and Z. The overall rate constant C determines the relative strength of the turbulent stirring in the model. The transfer coefficient α determines the degree of kinetic energy exchange among velocity components. The viscous cutoff parameter Z determines the smallest eddy size for given local strain conditions. What remains in order to completely specify an ODT flow simulation are the physical properties of the fluid (density, viscosity, etc.) and the proper definition of initial and boundary conditions. Of these, only the boundary conditions for enclosed turbulent flows require further discussion here.

The boundary condition for molecular evolution, Eq. (4.1), is simply the standard no-slip condition, i.e., the velocity components are set equal to the wall values. In enclosed flows, the turbulent stirring model also feels the effect of boundaries through the implicit limitation

they place on where eddies can occur and their maximum length scale, $L_{\max}$. For example, in an ODT simulation of turbulent channel flow, the largest mathematically realizable eddy event is equal to the channel width. However, since an eddy event is simply a model for turbulent mixing, it should not be surprising that the behavior of real 3D flow is better represented by setting $L_{\max}$ to a somewhat smaller value. Although not significant to the LES/ODT submodel introduced here (where the LES/ODT coupling limits the physical size of the maximum eddy length), this interesting detail is illustrated in example calculations of channel flow using stand-alone ODT in Section 4.1.4.

Finally, we briefly note that an additional step is typically introduced in stand-alone calculations in order to suppress unphysically large eddies that may otherwise occasionally occur. Like other multiscale models, ODT has a low-wavenumber divergence that must be suppressed by introducing a cutoff mechanism [35]. For the example stand-alone calculations presented below, the "median method" described in [36] is used. However, this detail is also unimportant to the LES/ODT coupling developed here because in this context the ODT eddy event size is restricted, by construction, to only those length scales unresolved by the LES.

4.1.3 Numerical Implementation

Neglecting data-gathering procedures, the numerical implementation of an ODT simulation involves three subprocesses: molecular evolution, eddy selection, and eddy implementation.

Molecular evolution according to Eq. (1) can be computed numerically using any conventional approach. In the calculations performed here the molecular evolution is computed each time the eddy event rate distribution is sampled, leading to very small time steps. Thus first order explicit time integration coupled with second order central differencing of the diffusion term is employed.

As explained above, the sequence of eddy events implemented during a simulated realization is determined by sampling from the rate distribution λ. However, each event, as well as the viscous evolution, Eq. (4.1), between events, changes the velocity profiles v_i and therefore modifies the rate distribution. From a computational viewpoint this is a problem because it causes explicit construction of, and sampling from, the rate distribution to be unaffordable owing to the need to repeatedly reconstruct this distribution.

To overcome this problem, an indirect but mathematically equivalent procedure is employed. This procedure is implemented once per eddy time step Δt_{eddy}. A candidate eddy is chosen by random sampling of y_0 and l values from a joint probability density function $g(y_0, l; t)$ (called the trial PDF) that can be arbitrary, subject to some weak constraints (though the procedure is most efficient if it approximates the true distribution). The remainder of the procedure is a determination of whether or not this candidate eddy should be implemented.

The implementation decision is based on the model (described in Section 2.2) that determines the 'turnover time' τ for the chosen eddy based on the instantaneous state of the simulated flow (for present purposes, the v_i profiles). τ is used to determine a physically based value of the probability density of the sampled values of y_0 and l. By comparing this probability density and the probability density given by the trial PDF $g(y_0, l; t)$ used for sampling, an acceptance probability is assigned such that the event statistics resulting from the combined process of sampling and subsequent acceptance or rejection of a candidate eddy closely approximate the event statistics specified by the physical model. The indirect procedure reproduces the statistics of the direct procedure to any desired accuracy by choosing a small enough sampling time step Δt_{eddy}.

As further explanation we note that $\lambda(y_0, l; t)$ can be viewed as the product of an overall rate, $R = \int \lambda(y_0, l; t)\, \mathrm{d}y_0 \mathrm{d}l$, of eddy events and a probability density function, $R^{-1}\lambda(y_0, l; t)$, from which eddy parameters y_0 and l are sampled. On this basis, the probability of acceptance of a candidate eddy is the product of $R\Delta t_{\text{eddy}}$ (the ratio of the model-prescribed event rate and the numerically implemented eddy-sampling rate) and $\lambda(y_0, l; t)/[Rg(y_0, l; t)]$ (the ratio of the model-prescribed probability density of the sampled parameter values and the probability density according to the trial PDF $g(y_0, l; t)$ that is sampled to select the parameters of the candidate eddy). $R\Delta t_{\text{eddy}} \ll 1$ is a necessary condition for the select-and-decide procedure to approximate closely the eddy statistics that would be obtained by direct random sampling of the rate distribution $\lambda(y_0, l; t)$ [35].

Eddy implementation on a discretized domain requires the definition of the discrete triplet map. For conservative implementation, the discrete triplet map is defined as a permutation of the cells of the discrete domain. The eddy interval is taken to be an integer multiple of three cells. The smallest consistently defined permutation involves six cells. Continuous and discrete representations of the triplet map are illustrated in Fig. 26(a) and (b) respectively. In Fig. 26(c), the discrete implementation of Eq. (4.3), including the kernel function, on a three component velocity field is illustrated. For this example, the initial values of v and w are uniform, but u has a linear profile. This highlights the transfer of kinetic energy among velocity components using the kernel function.

4.1.4 Stand-alone ODT Simulations of Channel Flow

The application of ODT as a stand-alone model for turbulent channel flow is demonstrated because it illustrates the method for determining the ODT model constants. This application is also used as an initial benchmark for the coupled LES/ODT model.

Fully-developed turbulent flow in a planar channel of width $2h$ is simulated by applying the boundary conditions $v_i = 0$ to all velocity components, and introducing a fixed source term $-\frac{1}{\rho}\frac{\partial P}{dx}$ on the right-hand side of Eq. (4.1) for $i = 1$. This term introduces an imposed mean pressure gradient in the streamwise (x) direction, but does not include pressure fluctuations.

(Pressure fluctuations are not modeled explicitly, but their effects are represented in the implementation of eddy events.)

ODT results for statistically steady flow are compared to corresponding DNS results of Moser *et al.* [55], who report results for $Re_\tau = 180$, 395, and 590. Here, $Re_\tau = u_\tau h/\nu$, where $u_\tau = \sqrt{\nu dv_2/dy|_{y=0}}$ is the friction velocity. Grid independent results were obtained for uniformly discretized meshes with $\Delta y^+ < 1$ ($y^+ = y u_\tau/\nu$).

To perform the simulations, values of C, Z, α and $L_{\max}$ must be specified. The friction law is sensitive mainly to C, which controls the turbulence intensity. By controlling the frequency of small eddies (i.e. the viscous cutoff), Z mainly affects the transition of the mean velocity profile from the near-wall viscous sublayer to the log-law region, thus defining the nature of the buffer layer. The effect of neglecting Z (by setting Z to a very small value) is illustrated by curve (a) in Fig. 27. For this case, adjustment of C to obtain a good fit to the friction law yields a value $C = 6.72$ and a mean velocity profile in which the buffer layer is essentially removed and the log layer extends down to within numerical resolution of the wall.

Optimum values of C and Z were found by adjusting these parameters to obtain a good match to the DNS friction coefficient and mean velocity profile at $Re_\tau = 590$, while keeping the values of α and $L_{\max}$ constant and equal to 2/3 (corresponding to an equalization of component energies) and $2h$ (the channel width), respectively. This yields curve (b) of Fig. 27, for which $C = 12.73$ and $Z = 98$. Finally, curve (c) of Fig. 27 illustrates the effect of adjusting the value of $L_{\max}$. For $L_{\max} = 2h$, the wake region of the flow (the flow in the central portion of the channel) is not well represented. However, for $L_{\max} = h$, the wake region is captured quite well. Based on these results the best-fit values for the ODT model parameters are taken to be $C = 12.73$, $Z = 98$, and $L_{\max} = h$, and are held constant for simulations at all other Reynolds numbers.

Fig. 28 shows computed friction coefficients over a range of Reynolds numbers and compares ODT values with the DNS data of Moser *et al.* [55] and the turbulent correlation of Dean [13]. The Reynolds number used in this plot is based on the bulk velocity and the channel width ($2h$), and the friction coefficient is defined as $C_f = 2(u_\tau/\bar{U})^2$, where $\bar{U}$ is the bulk velocity. Good agreement is obtained with the DNS C_f value at $Re_\tau = 395$ but a slight overprediction of C_f at $Re_\tau = 180$ is observed. ODT is formulated based on scalings applicable to high-intensity turbulence, so it may provide a less accurate representation of the weak turbulence at this Re_τ value. For the other flow properties considered here, neither DNS nor ODT exhibit much sensitivity to Re_τ, so additional stand-alone results are shown only for $Re_\tau = 590$.

The diagonal components, and the nonvanishing off-diagonal component, of the scaled Reynolds-stress tensor are shown in Fig. 29. The physically valid ODT definitions of these and other high-order statistics are explained in detail elsewhere [35, 36]. Of note is that in general the diagonal components are somewhat underpredicted by ODT, and the profile

of the streamwise component has a small dip (due to the discrete size of eddy events) at the near-wall peak. Later it is shown that LES/ODT results for the diagonal components are in much better agreement with DNS results, suggesting a more realistic forcing of the near-wall region when the bulk flow is modeled with LES and the effects are coupled to ODT. Figure 29 also illustrates that $\langle v_2'^2 \rangle$ and $\langle v_3'^2 \rangle$ are statistically identical. This is due to the coordinate invariance of the pressure scrambling mechanism used in the current multi-component formulation. More general formulations that break this symmetry (and involve three distinct eddy types) have been tested, but are not applied here.

Despite the discrepancies seen in Fig. 29, the ODT predictions of the terms of the v_1 variance budget, shown in Fig. 30 are in good overall agreement with the corresponding DNS terms. This suggests that ODT is a fundamentally sound model of near-wall flow energetics.

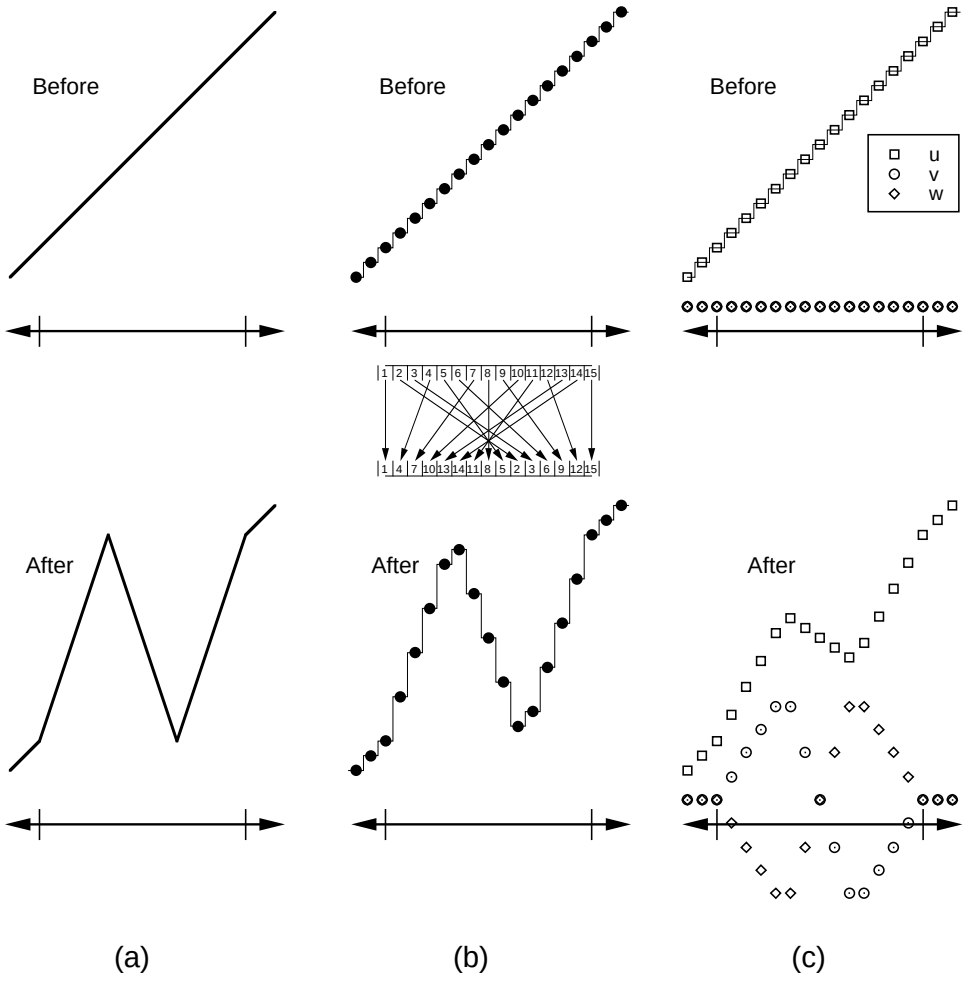

Figure 26: Illustration of (a) an analytical triplet map of a scalar with initially uniform gradient, (b) a discrete triplet map of a scalar with initially uniform gradient, and (c) a discrete eddy event on a three-component ODT velocity field where the initial values of v and w are uniformly zero.

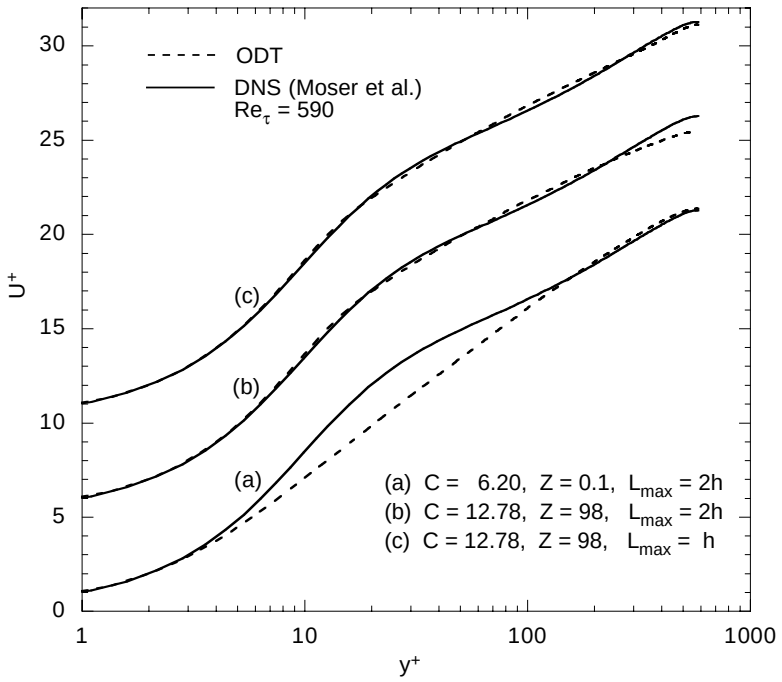

Figure 27: Semilog plot of ODT and DNS [55] mean velocity profiles for channel flow at $Re_\tau = 590$, in wall coordinates. Note that (b) and (c) are vertically offset from (a) for clarity in illustrating the effects of changing the ODT model parameters.

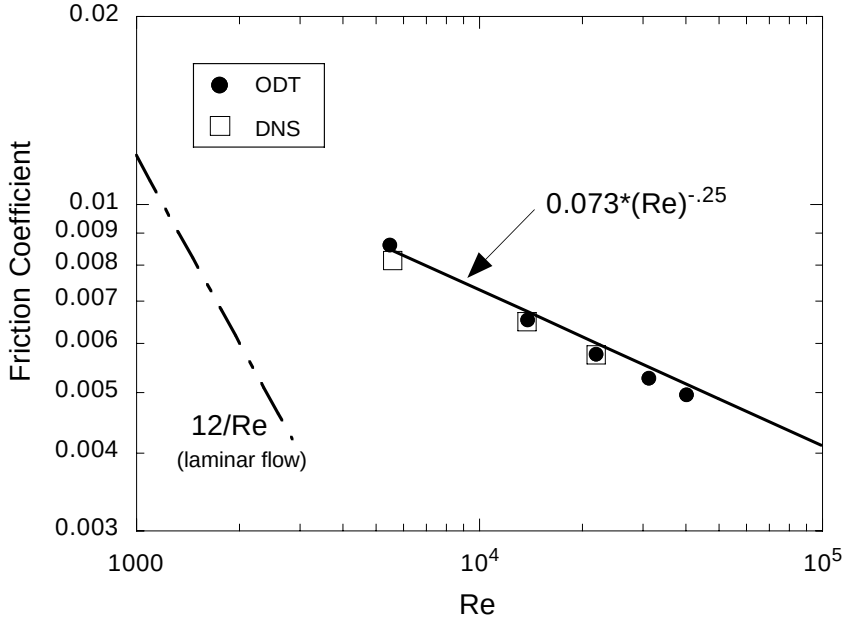

Figure 28: ODT computed friction coefficient C_f for channel flow compared to DNS data [55] and the correlation of Dean [13]. Here, Re is based on the bulk velocity and the channel width ($2h$).

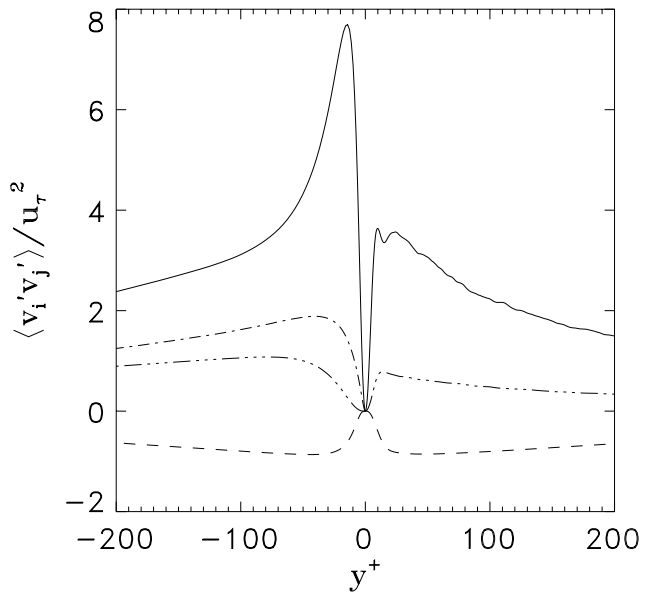

Figure 29: Lateral profiles of Reynolds stress components in channel flow, scaled by u_τ^2: ——, $\langle v_1'^2 \rangle$; — · · · —, $\langle v_2'^2 \rangle$; — · —, $\langle v_3'^2 \rangle$; – – –, $\langle v_1' v_2' \rangle$. (The ODT $\langle v_3'^2 \rangle$ profile is identical to the ODT $\langle v_2'^2 \rangle$ profile.) ODT and DNS [55] results are plotted right and left of centerline, respectively.

4.2 Formulation of an ODT-Based Near-Wall Subgrid model

Having reviewed both the ODT stand-alone model and the LES model, we now describe a method for coupling the highly resolved (in 1D space) ODT model, near all no-slip walls, with traditional 3D LES turbulence modeling in the bulk flow.

4.2.1 Geometric Considerations

The ODT wall model affects the LES equations in two distinct near-wall regions, as illustrated in Fig. 31. For reference purposes, we call the layer of LES cells that are immediately adjacent to the no-slip wall the ODT inner region. It is in this region that the ODT model is primarily active. A second region, called the LES/ODT overlap region, extends outward from the top of the inner region through a number of additional LES cell layers. The extent of this region is determined by an ODT model parameter associated with the LES filter width. The flow in this domain is primarily controlled by standard LES equations, but is also affected by an LES/ODT coupling described in Section 4.6.

From an LES perspective, we begin by conceptualizing all LES cells that lie adjacent to solid walls (i.e., the inner ODT region) in the framework of the volume-balance LES model developed by Schumann [67] and briefly described in Section 3.1 (see Eq. (2.9)). Associated with each of these inner-region control volumes, we define an ODT line that begins at the no-slip wall and extends upward to the top of the control volume. All three ODT velocity components as well as any scalar quantities of interest, except pressure, are spatially resolved in the wall-normal direction on the ODT lines. Pressure is only resolved on the LES-scale mesh (i.e., one value per LES control volume) because 3D continuity constraints are imposed by pressure only on the LES grid.

Volume-averaged instantaneous values for the inner region can be computed simply as the numerical average of their corresponding ODT values on a given ODT line, as follows:

$$\bar{\phi} = \frac{1}{N_{\mathrm{ODT}}} \sum_{m=1}^{N_{\mathrm{ODT}}} \phi_m, \tag{4.13}$$

where ϕ denotes a generic variable, and N_{ODT} is the number of ODT points on the discretized ODT line. This is a useful definition which is used for relating ODT variables to LES variables.

The ODT-resolved variable ϕ_m represents an instantaneous volume average over a control volume of height $\Delta Y/N_{\mathrm{ODT}}$ at a nominal distance $y = y_m = \left(\frac{m-\frac{1}{2}}{N_{\mathrm{ODT}}}\right)\Delta Y$ above the wall, where ΔY is the height of the LES control volume. This is illustrated pictorially in Fig. 32, where an array of ODT sub-volumes embedded in a near-wall LES control volume is depicted. In effect, each point on the ODT line is conceptualized as an LES sub-control volume in exactly the same sense as developed by Schumann, only in this case, the resolution in the wall-normal direction is very fine.

4.2.2 Revised ODT Evolution Equations

ODT as a stand-alone model is a closed system that consists of a single ODT line. However, when used as a near-wall LES subgrid model the near-wall region consists of a forest of ODT lines, and the formulation must therefore be extended to allow for advective transport between ODT domains that lie in adjacent LES control volumes. This is accomplished by modifying the ODT evolution equations (see Eqs. (4.1) and (4.2)) to include advective transport terms as follows:

$$\left(\partial_t - \nu\partial_{x_2}^2\right) v_i(y,t) + \partial_{x_j}\left(V_j(y,t)v_i(y,t)\right) + \frac{1}{\rho}\left.\frac{\partial \bar{P}}{\partial x_i}\right|_{i\neq 2} = 0 \tag{4.14}$$

$$\left(\partial_t - \nu\partial_{x_2}^2\right) \theta(y,t) + \partial_{x_j}\left(V_j(y,t)\theta(y,t)\right) = 0. \tag{4.15}$$

Here, a mean pressure gradient term (assumed constant) has been included except in the wall-normal direction ($i = 2$), and a local advective velocity field $V_j(y,t)$, has been introduced. Taking $V_1(y,t)$ and $V_3(y,t)$ to be $v_1(y,t)$ and $v_3(y,t)$ respectively gives a formally valid representation of lateral transport. However, definitions of V_1 and V_3 that involve temporal filtering of v_1 and v_3 are preferred because the spatial derivatives in the $i = 1$ and $i = 3$ directions in Eqs. (4.14) and (4.15) are implemented numerically as spatial differences over LES-scale spatial increments ΔX and ΔZ, respectively, as illustrated by the LES/ODT control-volume geometry sketched in Fig. 32. (Thus, all functions of y in Eqs. (4.14) and (4.15) are also functions of x and z, though these dependencies are not shown explicitly.)

In view of the coarseness of the x and z resolution relative to the y resolution, the convective time scale for property transfer between laterally adjacent ODT sub-volumes is the LES time scale Δt rather than the fine-grained time scale on which other ODT processes evolve. Accordingly, temporal filtering suppresses unphysical high-frequency fluctuations due to the more rapid evolution processes implemented in the vertical direction (which can be resolved temporally owing to the finer spatial resolution in that direction). These considerations are analogous to time-stepping issues that arise in any numerical scheme involving high-aspect-ratio control volumes.

A simple temporal filter that would serve this purpose is

$$V_1(y,t) = \frac{1}{\Delta t}\int_{t-\Delta t}^{t} v_1(y,t')\,dt' \tag{4.16}$$

$$V_3(y,t) = \frac{1}{\Delta t}\int_{t-\Delta t}^{t} v_3(y,t')\,dt', \tag{4.17}$$

where Δt is the LES time step. A computationally more convenient definition that serves the same purpose is introduced in Section 4.4.1.

There is an important distinction between the instantaneous wall-normal ODT velocity component v_2 and the instantaneous tangential velocity components v_1 and v_3. In the approach developed here, v_1 and v_3 are treated as true advecting velocities, and we compute V_1

and V_3 from them. However, v_2 is not considered an advecting velocity because eddy events are the model for turbulent transport in the wall-normal direction. Instead we conceptualize v_2 as a representation of the wall-normal velocity component kinetic energy per unit mass (actually the square root of that energy). Thus, no pressure gradient is included in the evolution equation for v_2. To compute the advective transport velocity in the wall-normal direction, V_2, we simply apply continuity and integrate from the wall, as follows:

$$V_2(y,t) = -\int_0^y \left(\frac{\partial V_1}{\partial x_1} + \frac{\partial V_3}{\partial x_3} \right) dy. \tag{4.18}$$

Note that this automatically satisfies continuity within the LES-scale control volume.

The ODT evolution equations are solved only in the inner region and boundary conditions must be applied both at the wall ($y = 0$) and at the top of the inner region ($y = \Delta Y$). At $y = \Delta Y$ this is accomplished by assuming a linear variation of all velocity components at every instant in time between the last ODT node ($y = \Delta Y$) and the corresponding LES values in the overlap region at $y = \frac{3}{2}\Delta Y$. (The LES grid structure and its implications for LES/ODT coupling are discussed in Section 4.6.) Given this assumption, all required boundary fluxes (both advective and diffusive) can be computed based on the boundary conditions at $y = 0$:

$$\begin{aligned} v_1 = v_2 = v_3 = 0 \\ V_2 = 0 \end{aligned} \tag{4.19}$$

and at $y = \Delta Y$:

$$\frac{\partial v_i}{\partial x_2} = \left(\bar{u}_i|_{y=(3/2)\Delta Y} - v_i|_{y=\Delta Y} \right) / [(3/2)\Delta Y]. \tag{4.20}$$

Note that in Eq. (4.20), $\bar{u}_i|_{y=(3/2)\Delta Y}$ denotes the current value of LES velocity component i at a distance from the wall equal to $\frac{3}{2}\Delta Y$.

4.2.3 LES/ODT Eddy Events

Although the ODT evolution equations are only solved in the inner region, eddy events can extend from any location within the inner region out into the LES domain. In stand-alone ODT, the length scale of the largest possible eddy event, $L_{\max}$, corresponds to the integral scale of the flow problem. For example, in channel flow the largest possible eddy is limited by the distance between the two walls, but may be set to a lower value if warranted (Section 4.1.4). However, as an LES subgrid model ODT must only model the unresolved small-scale eddies. Independent of filter type, the smallest possible eddy that can be represented on the grid by an LES is 2Δ (sometimes called the Nyquist limit), but this will not be an accurate representation. In practice, both the numerical method and the particular filter type chosen will determine the length-scale range over which the resolution of smaller eddies degrades.

When ODT is modeling the LES subgrid processes, the value for $L_{\max}$ should correspond to these same limits. In other words, the largest length scales modeled by ODT should correspond to the smallest length scales captured by the LES. How we determine the value of $L_{\max}$ is discussed in Section 4.5.

Fig. 33 illustrates that all eddy events are required to extend into the inner region, and that eddies are allowed to extend out as far as permitted by the eddy-size bound $L_{\max}$. Eddies can therefore extend out as far as $y = \Delta Y + L_{\max}$, which sets the vertical extent of the overlap region. Eddy events can thus transfer fluid between the inner and overlap regions and within each region. Overlap-region LES control volumes do not contain ODT substructure. Transfers that involve the overlap region therefore employ a coarse-grained representation of eddy effects in the overlap region. Namely, fluxes corresponding to transfers of fluid properties (momentum, mass fractions, etc.) across overlap-region LES control-volume interfaces are summed at each interface (Section 4.4.1).

Overlap-to-inner transfer requires a construction of ODT-resolved information using overlap-region LES-scale variables. For this purpose, linear interpolation of the LES-scale variables in the overlap region is used to provide ODT-resolved values as needed.

The accumulated fluxes due to eddy events that transfer fluid across LES control-volume interfaces are incorporated into the LES time-stepping scheme, both to enforce consistency between ODT and LES evolution and to evaluate unclosed terms in the LES evolution equations (Section 4.4.2). Note that the LES-scale properties at the LES node points are considered unchanged during the fine-grained ODT time evolution. LES-scale effects of ODT processes are implemented during time advancement of the LES equations.

4.2.4 Synopsis of the Coupled LES/ODT Model

As modeled here, the equations simulating the turbulent flow are distinct in each of the three flow regions, i.e., the ODT inner region, the LES/ODT overlap region, and the LES core-flow region.

In the ODT inner region, the revised ODT evolution Eqs. (4.14) and (4.15) are solved subject to the boundary conditions given by Eqs. (4.19) and (4.20), and the advecting velocities defined in Section 4.6.1 (with $V_2(y,t)$ defined by Eq. (4.18)). Eddy events occur at various times and locations, and with various length scales as per the stochastic model described in Section 2.

When an instantaneous eddy event extending into the overlap region occurs, time-accurate implementation of conservation laws would require all affected LES quantities to be adjusted based on the net transport across each LES control-volume face. However, in practice, the LES equations of motion are solved numerically using time steps that are much larger than those required by the ODT subgrid model. In the current numerical implementation (described in detail in Section 4.6), explicit LES/ODT coupling is accomplished by accumu-

lating the net transfer across each LES control-volume interface (from all processes) during the ODT evolution within an LES time step. The net transfer during this time period is summed and then divided by the LES time step - thus providing an explicit flux value for input to the LES equations, in lieu of instantaneous adjustment of LES values when eddy events occur. These inputs supplement LES fluxes in the LES/ODT overlap region (that are modeled based on the LES model chosen for the bulk flow), and constitute the up-scale coupling between the ODT equations and the LES equations. Down-scale coupling occurs when the LES equations are solved. LES time advancement yields a revised LES velocity field that reflects the global effects of the pressure field. At this point, ODT velocities in the inner region are adjusted to be consistent with LES. This adjustment event is similar to an ODT eddy event in that it occurs at an instant in time. However, this event only affects the average velocity in the inner region, not the ODT scale variations. The specific method used here is explained in Section 4.6.4.

In the LES/ODT overlap region, the LES equations (Eqs. (2.7) and (2.8)) are solved subject to a flux-matching condition at the LES/ODT interface (i.e., $y = \Delta Y$), and the addition of the supplemental fluxes caused by eddy events that extend across LES cell boundaries in the overlap region. Note that the flux at $y = \Delta Y$ includes a flux implied by Eq. (4.18) and the net effect of instantaneous transport due to eddy events extending outward from the ODT inner region (see Fig. 33).

In the LES core-flow region, the LES equations are solved without modification.

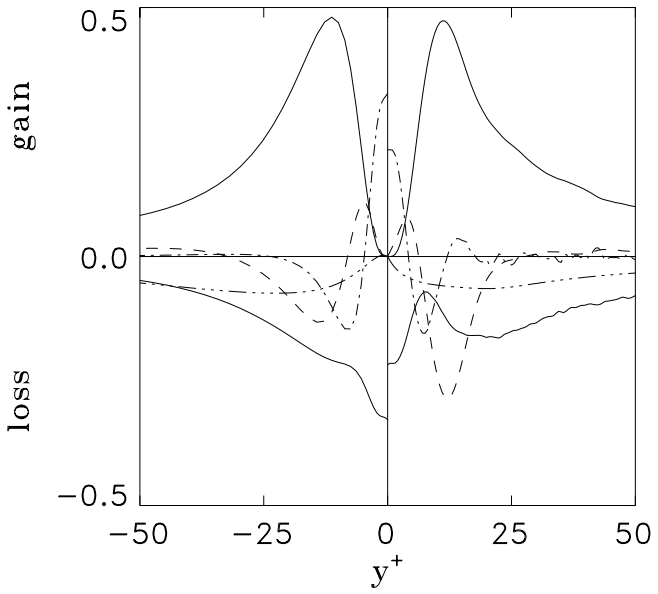

Figure 30: Budget of $\langle v_1'^2 \rangle$ in channel flow, in wall coordinates: ——, production (upper), dissipation (lower); – – –, advective transport; — · —, viscous transport; — · · · —, scrambling. ODT and DNS [55] results are plotted right and left of centerline, respectively.

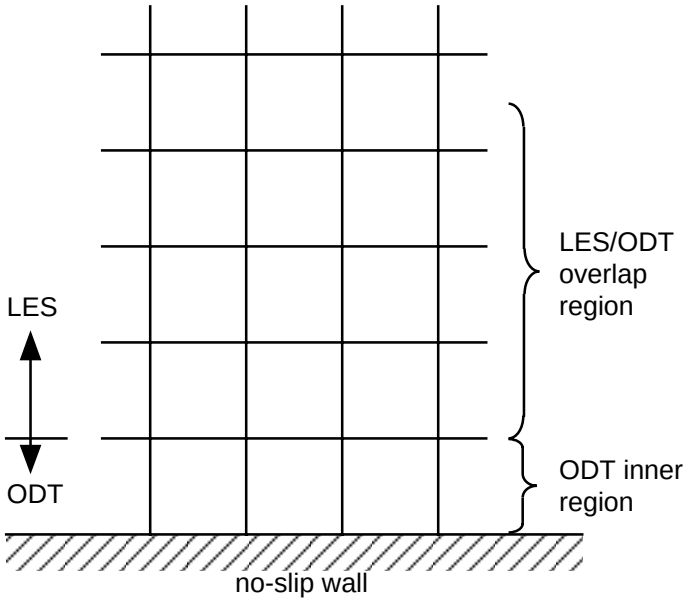

Figure 31: Illustration of the ODT inner and overlap region domains in the LES mesh.

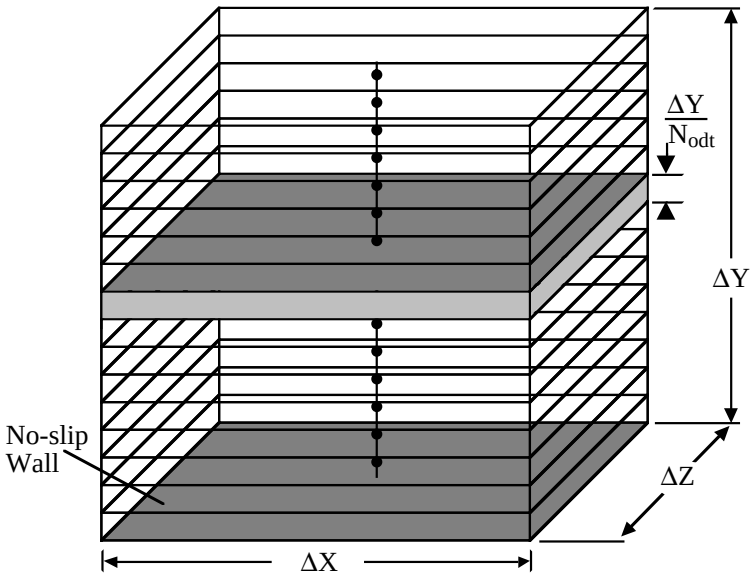

Figure 32: Illustration of ODT sub-control volumes embedded in an "inner-region" LES control volume. The nominal ODT domain is the wall-normal line passing through the center of the control volume. Points of the discretized domain mark the ODT sub-control volumes.

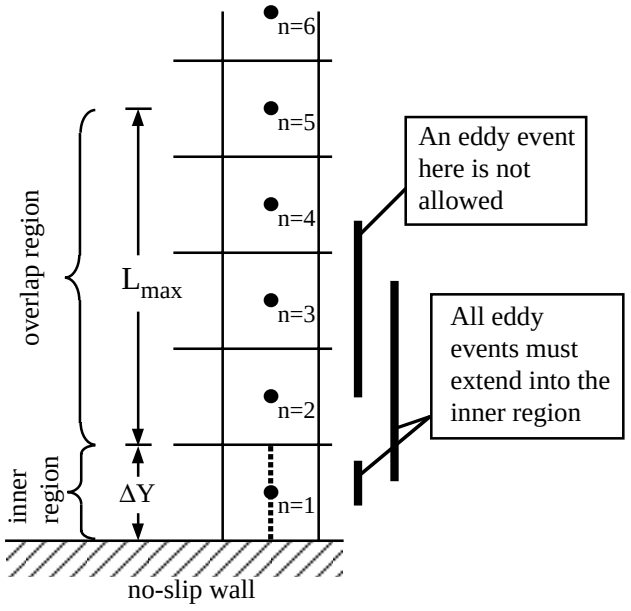

Figure 33: Illustration of allowable eddy event locations within the near-wall region. The dashed line in the inner region indicates that the fine grained ODT domain exists only in this region.

4.3 Description of the LES Simulation Code

The base LES code used for testing the near-wall ODT subgrid model is a structured-grid second-order finite-difference code specifically designed for doing channel flow [54], and was obtained from Stanford University through our collaboration with the Center for Turbulence Research. In this code, periodic boundary conditions are imposed in the streamwise (x) and spanwise (z) directions and the flow is driven by a constant pressure gradient in the streamwise direction. The grid is staggered (see [28, 59, 67]) and can be stretched in the wall-normal direction using a hyperbolic-tangent mapping if desired.

A semi-implicit time-integration algorithm is used where the diffusion terms in the wall-normal direction (y) are treated implicitly with the Crank-Nicholson scheme, and a third-order Runge-Kutta scheme (see [72]) is used for all other terms. The fractional-step method of Dukowicz & Dvinsky [17] is used in conjunction with a Van Kan [33] type of pressure term. The corresponding Poisson equation for pressure is solved using a tri-diagonal matrix algorithm in the wall-normal direction and fast Fourier transforms (FFT) in the periodic directions.

The three-step time-advancement scheme used in the base LES code can be written in the following way:

$$\begin{aligned}\frac{\bar{u}_i^k - \bar{u}_i^{k-1}}{\Delta t} = \quad & \alpha_k \mathbf{L}_y(\bar{u}_i^{k-1}) + \beta_k \mathbf{L}_y(\bar{u}_i^k) + (\alpha_k + \beta_k)\mathbf{L}_{xz}(\bar{u}_i^{k-1}) \\ & -\gamma_k \mathbf{N}(\bar{u}_i^{k-1}) - \zeta_k \mathbf{N}(\bar{u}_i^{k-2}) - (\alpha_k + \beta_k)\tfrac{1}{\rho}\tfrac{\delta \bar{P}^k}{\delta x_i} - (\alpha_k + \beta_k)\tfrac{PG_i}{\rho} \qquad (4.21)\end{aligned}$$

$$\frac{\delta \bar{u}_i^k}{\delta x_i} = 0, \qquad (4.22)$$

where $k = 1, 2, 3$ denotes the sub-step number, $\bar{u}_i^0$ and $\bar{u}_i^3$ are the LES velocities at the beginning and end of the time step, and PG_i denotes the constant portion of the pressure gradient driving the channel flow (zero for $i = 2$ and 3). In the present implementation, $\delta/\delta x_i$ denotes a second-order central-difference operator and accordingly, $\mathbf{N}(\bar{u}_i)$ represents a second-order finite-difference approximation to the advection terms:

$$\mathbf{N}(\bar{u}_i) = \frac{\delta}{\delta x_j}(\bar{u}_i \bar{u}_j). \qquad (4.23)$$

Two distinct operators for the viscous terms, $\mathbf{L}_{xz}(\bar{u}_i)$ and $\mathbf{L}_y(\bar{u}_i)$, are defined so that the implicit treatment of the wall-normal diffusion terms can be clearly distinguished:

$$\mathbf{L}_{xz}(\bar{u}_i) = \frac{\delta}{\delta x_j}\left[(\nu + \nu_S)\left(\frac{\delta \bar{u}_i}{\delta x_j}\right)\right] \qquad (4.24)$$

$$\mathbf{L}_y(\bar{u}_i) = \frac{\delta}{\delta x_2}\left[(\nu + \nu_S)\left(\frac{\delta \bar{u}_i}{\delta x_2}\right)\right], \qquad (4.25)$$

where the right-hand side of Eq. (4.24) is summed over $j = 1$ and 3, the relation $\nu = \mu/\rho$ and the definition $\nu_S = \mu_S/\rho$ of the kinematic eddy viscosity have been introduced, and second-order central differencing is again used.

The time-advancement coefficients α_k, β_k, γ_k, and ζ_k, $k = 1$, 2, 3, are constants selected such that third-order accuracy is obtained for the advection term and second-order accuracy for the viscous term. The values of these coefficients are

$$\gamma_1 = 8/15 \quad \gamma_2 = 5/12 \quad \gamma_3 = 3/4$$

$$\zeta_1 = 0 \quad \zeta_2 = -17/60 \quad \zeta_3 = -5/12$$

$$\alpha_1 = 4/15 \quad \alpha_2 = 1/15 \quad \alpha_3 = 1/6$$

$$\beta_1 = 4/15 \quad \beta_2 = 1/15 \quad \beta_3 = 1/6.$$

Because ζ_1 vanishes, Eq. (4.21) does not require the evaluation of $\bar{u}_i^{k-2}$ for $k = 1$. The effective sub-time-step for this method is $\Delta t_k = (\alpha_k + \beta_k)\Delta t$.

Applying the fractional-step method of Dukowicz & Dvinsky [17] to Eqs. (4.21) and (4.22), we obtain

$$\begin{aligned}\frac{\hat{\bar{u}}_i^k - \bar{u}_i^{k-1}}{\Delta t} = \quad & \alpha_k \mathbf{L}_y(\bar{u}_i^{k-1}) + \beta_k \mathbf{L}_y(\hat{\bar{u}}_i^k) + (\alpha_k + \beta_k)\mathbf{L}_{xz}(\bar{u}_i^{k-1}) \\ & -\gamma_k \mathbf{N}(\bar{u}_i^{k-1}) - \zeta_k \mathbf{N}(\bar{u}_i^{k-2}) \\ & -(\alpha_k + \beta_k)\tfrac{1}{\rho}\tfrac{\delta \bar{P}^{k-1}}{\delta x_i} - (\alpha_k + \beta_k)\tfrac{PG_i}{\rho} \end{aligned} \tag{4.26}$$

$$\frac{\bar{u}_i^k - \hat{\bar{u}}_i^k}{\Delta t} = -\frac{\delta \phi^k}{\delta x_i}, \tag{4.27}$$

where ϕ^k and $\bar{P}$ are related by

$$\frac{\delta \phi^k}{\delta x_i} = (\alpha_k + \beta_k)\frac{1}{\rho}\frac{\delta}{\delta x_i}(\bar{P}^k - \bar{P}^{k-1}) - \beta_k \mathbf{L}_y(\bar{u}_i^k - \hat{\bar{u}}_i^k), \tag{4.28}$$

and the hat symbol placed over a variable denotes an intermediate value. For clarity we note that Eq. (4.21) can be recovered by solving for $\hat{\bar{u}}_i^k$ in Eq. (4.27), and then substituting this identity and that of Eq. (4.28) back into Eq. (4.26). In practice, the rightmost term in Eq. (4.28) is neglected, resulting in the 'splitting' error associated with this method.

Solving for $\bar{u}_i^k$ in Eq. (4.27) and applying the divergence-free constraint, Eq. (4.22), we obtain the discrete Poisson equation,

$$\frac{1}{\Delta t}\frac{\delta \hat{\bar{u}}_i^k}{\delta x_i} = \frac{\delta^2 \phi^k}{\delta x_i \delta x_i}. \tag{4.29}$$

To advance from sub-step k-1 to k requires the completion of a two-part fractional-step cycle. In the first part, Eq. (4.26) is solved for $\hat{\bar{u}}_i^k$, the intermediate or interim velocity field.

In the second part, Eq. (4.29) is solved for ϕ^k. Knowing ϕ^k, Eq. (4.28) is integrated (with the rightmost term omitted) to compute the change in pressure from $k-1$ to k, and Eq. (4.27) is used to compute the new velocity field, $\bar{u}_i^k$.

The subgrid-scale model used to compute the subgrid eddy viscosity is the dynamic Smagorinsky model of Germano [24] with the least-square technique of Lilly [44] as described in Section 2. Averaging in the spanwise and streamwise directions is used to compute C_S (see Eq. (2.33)) and filtering is performed in these directions but not in the y direction. The ratio of the test filter width to the grid filter width is taken to be 2.0.

4.4 Numerical Implementation of the Near-Wall Model Within a LES Code

In order for the LES pressure field to couple properly to the ODT velocities, it is important to assure that the spatial locations of the ODT velocity components are consistent with the LES numerical discretization. In the staggered-grid method used in the LES code, the control volumes for mass and momentum are offset from one another such that the velocity components are calculated for the points that lie on the faces of the mass-conservation control volumes. This is illustrated in Fig. 34, where the LES-scale velocities are represented with large arrow heads, and the locations of the associated ODT velocity components are given by the points that lie on the lines shown.

It is also important for the ODT temporal advancement scheme to couple in a consistent way to the LES code. As described above, the LES time-integration scheme used here is a three step Runga-Kutta method where each step consists of a two-part fractional-step cycle. To use the ODT wall model, we modify this cycle to include two additional parts specific to the near-wall ODT model. In the new part 1, the inner region ODT equations are evolved and the momentum exchange at LES interfaces due to the ODT processes are summed. At the end of this part, values for interim LES velocities $\hat{\bar{u}}_i^k$ in the ODT inner region are computed from these results. In part 2, modified forms of Eq. (4.26) are solved for $\hat{\bar{u}}_i^k$ throughout the rest of the domain. The modifications correspond to ODT contributions to the surface fluxes in the LES/ODT overlap region. Part 3 is the continuity-enforcing pressure-projection step that involves solving a discrete Poisson equation for a pressure-adjusted velocity field $\bar{u}_i^k$. This part is unchanged. The fourth and final part consists of adjusting the ODT-resolved profiles so that the step-ending values of $V_i(y)$ and $v_i(y)$ are consistent with the new pressure-adjusted LES velocity field in the inner region.

Details of each of these four parts are given next.

4.4.1 Details of part 1

We begin by defining an ODT time step $\Delta t'$, and the associated ODT time-step index k'. The value of $\Delta t'$ is much smaller than the LES time step Δt so that a significant number

of ODT time steps must be taken to advance in time from LES substep index $k-1$ to k, where $k=0$ represents the final state of the previous LES time step.

Each ODT time step consists of (a) the evolution of the molecular equations from time t to $t+\Delta t'$, (b) the stochastic sampling procedure by which eddy events are determined, and (c) implementation of the selected eddy (if the sampling procedure determines that an eddy should be implemented).

The molecular equations are numerically integrated using the following explicit numerical approximation to Eq. (4.14):

$$\frac{v_i^{k'}-v_i^{k'-1}}{\Delta t'}=\frac{\delta}{\delta x_2}\left(\nu\frac{\delta v_i^{k'-1}}{\delta x_2}\right)-\frac{\delta}{\delta x_j}\left(V_j^{k'-1}v_i^{k'-1}\right)-\frac{PG_i}{\rho}, \tag{4.30}$$

where PG_i denotes the constant mean pressure gradient imposed on the flow, which in channel flow is zero for $i=2$ and 3. This term does not reflect the fluctuating pressure field that arises due to the turbulent fluctuations in the flow. This part of the pressure field is modeled through the pressure projection (see Sections 4.4.3 and 4.4.4). Second-order central differencing is used to compute all gradients, and boundary conditions are imposed as per Eqs. (4.19) and (4.20).

To compute the new ODT advecting velocity field $V_i^{k'}$, an alternative to Eqs. (4.16) and (4.17) has been implemented that avoids the need to maintain a memory-intensive history of the instantaneous ODT velocity field. Namely, a temporal 'mixing-cup' approach is adopted. Given the values of V_i at time index $k'-1$, the values at k' are computed as

$$V_i^{k'}=\left(1-\frac{\Delta t'}{\Delta t}\right)V_i^{k'-1}+\left(\frac{\Delta t'}{\Delta t}\right)v_i^{k'} \tag{4.31}$$

for $i=1$ and 3 and Eq. (4.18) is applied for $i=2$. We note that an alternative (not implemented here) to using Eq. (4.31) would be to hold $V_i^{k'}$ constant over the LES sub-step k to $k+1$, and update these values at the same time the LES velocity field is updated.

After the molecular processes have evolved from time t to $t+\Delta t'$, the possibility of an eddy event is evaluated through the standard ODT stochastic-sampling procedure. However, allowable eddies are limited to those that extend into the inner region (as illustrated in Fig. 33), and the length of the largest possible eddy, $L_{\max}$, is a model parameter that, for now, must be specified. By design it must be of the order of the smallest length scale resolved by LES. Since this is a function of the numerics and filtering used in the LES code, its specific value must be likewise dependent.

If a trial-eddy location and length are chosen such that the eddy extends into the overlap region (see Fig. 33), ODT-resolved values are obtained in that region by linear interpolation of the LES field variables, as explained in Section 4.2.3.

Although eddy events implemented in the usual manner would modify property profiles in the LES/ODT overlap region, the modifications are not implemented in that region. Rather,

statistics are gathered, as described next, that subsequently enable LES-scale implementation of the implied property transfers across LES control-volume interfaces.

As the ODT velocity fields are advanced in time from LES substep index $k-1$ to k, momentum is transferred across the interface between the inner and overlap regions by three mechanisms: molecular diffusion, wall-normal advection, and eddy events. In addition, eddy events that extend to points greater than $y = 2\Delta Y$ induce momentum transfer across LES control-volume interfaces in the overlap region. In order for the ODT model to couple properly to the LES, a running sum of the net transport across all LES control-volume interfaces due to ODT processes must be maintained. For convenience in explaining the model, we define these sums as follows:

$S_i^n = i^{\text{th}}$ component momentum transport (per unit time, mass, and area) across an interface between a near-wall LES control volume n (where $n = 1$ denotes the inner region) and its adjacent $(n+1)$-layer LES control volume.

$S_{D_i}^n =$ that portion of S_i^n due entirely to the molecular-diffusive term of Eq. (4.30).

$S_{A_i}^n =$ that portion of S_i^n due entirely to the advective term of Eq. (4.30).

$S_{E_i}^n =$ that portion of S_i^n due entirely to ODT eddy events.

For $n = 1$, these sums are computed as

$$\begin{aligned} S_i^{1,k} &= -\tfrac{\Delta t'}{\Delta t_k}\textstyle\sum_{k'}\left(\nu\tfrac{\delta v_i^{k'-1}}{\delta x_2}\right)\Big|_{y=\Delta Y} + \tfrac{\Delta t'}{\Delta t_k}\textstyle\sum_{k'}\left(V_2^{k'-1}v_i^{k'-1}\right)\Big|_{y=\Delta Y} + \tfrac{1}{\Delta t_k}\textstyle\sum_m E_{m,i}^1 \\ &= S_{D_i}^{1,k} + S_{A_i}^{1,k} + S_{E_i}^{1,k} \end{aligned} \tag{4.32}$$

where the additional superscript k has been added to denote that these quantities are computed during the interval Δt_k from LES substep $k-1$ to k.

The only ODT process that can influence the LES equations at control volume interfaces greater than $y = \Delta Y$ is an eddy event. Thus for $n > 1$, $S_{D_i}^n = S_{A_i}^n = 0$, and we can write

$$S_i^{n,k} = S_{E_i}^{n,k} = \frac{1}{\Delta t_k}\sum_m E_{m,i}^n \qquad (for\ \ n > 1), \tag{4.33}$$

where Δt_k is the sub-time-step defined in Section 4.3 and $E_{m,i}^n$ denotes a transfer of i-component momentum across an interface between LES layers n and $n+1$ due to an eddy event m. It is easily computed as the x_2-integrated difference in momentum (after minus before) on one side of the interface following an eddy event.

At the end of part 1, the ODT velocity field has evolved due to advection, diffusion, and eddy events, but without a two-way coupling with the LES velocity field (which has been held constant). Part 1 is the ODT analog of solving Eq. (4.26) for the interim LES velocity $\hat{\tilde{u}}_i^k$ (part 2 below). Thus ODT values that have been evolved through the end of part one are in like manner hereafter denoted with a hat, e.g., $\hat{V}_i^k(y)$.

4.4.2 Details of part 2

In part 2 we solve for the interim LES velocity field $\hat{\bar{u}}_i^k$ throughout the rest of the domain outside of the inner region, a process corresponding to the solution of Eq. (4.26), but with modifications associated with the LES/ODT overlap region that reflect ODT contributions to the LES surface fluxes in that region.

In the first LES layer of the overlap region, the transport across the LES/ODT interface at the top of the inner region is completely specified by the values computed in part 1. Also, the LES-specified advective flux across the top of this layer is enhanced by any contributions due to eddy events bridging this face. To account for these effects, Eq. (4.26) must be modified (in this layer only) as follows:

$$\begin{aligned}
\frac{\hat{\bar{u}}_i^k - \bar{u}_i^{k-1}}{\Delta t} = \quad & \frac{(\nu+\nu_S)}{\Delta x_2}\left[\alpha_k\left(\frac{\delta \bar{u}_i^{k-1}}{\delta x_2}\right) + \beta_k\left(\frac{\delta \hat{\bar{u}}_i^{k}}{\delta x_2}\right)\right]\Bigg|_{x_2=2\Delta Y} \\
& -\frac{(\alpha_k+\beta_k)}{\Delta x_2}\left[S_{E_i}^{2,k-1} - S_{E_i}^{1,k-1} - S_{D_i}^{1,k-1}\right] \\
& +(\alpha_k+\beta_k)\mathbf{L}_{xz}(\bar{u}_i^{k-1}) - \gamma_k\mathbf{N}_{xz}(\bar{u}_i^{k-1}) - \zeta_k\mathbf{N}_{xz}(\bar{u}_i^{k-2}) \\
& -\frac{1}{\Delta x_2}\left[\gamma_k\left(\bar{u}_i^{k-1}\bar{u}_2^{k-1}\right) + \zeta_k\left(\bar{u}_i^{k-2}\bar{u}_2^{k-2}\right)\right]\Bigg|_{x_2=2\Delta Y} \\
& +\frac{(\alpha_k+\beta_k)}{\Delta x_2}\left[S_{A_i}^{1,k-1}\right] \\
& -(\alpha_k+\beta_k)\frac{1}{\rho}\frac{\delta \bar{P}^{k-1}}{\delta x_i} - (\alpha_k+\beta_k)\frac{PG_i}{\rho}.
\end{aligned} \tag{4.34}$$

Here, the modified convection operator $\mathbf{N}_{xz}$ is defined as

$$\mathbf{N}_{xz}(\bar{u}_i) = \frac{\delta}{\delta x_j}(\bar{u}_i\bar{u}_j), \tag{4.35}$$

where the right-hand side is summed over $j = 1$ and 3. Note that the difference between Eq. (4.26) and Eq. (4.34) is that all finite-difference terms associated with transport across the LES/ODT interface at the top of the inner region are replaced by the explicit sums computed in part 1, and the fluxes at the top of layer 2 are augmented by ODT contributions. For example, the two RHS terms on the first line of Eq. (4.34) are the diffusion terms (molecular and subgrid turbulent) across the $y = 2\Delta Y$ interface from the normal LES model. Because the wall normal diffusion terms are integrated using a Crank-Nicholson scheme, there are both α_k and β_k contributions to the sub-time-step advancement. On the second line of Eq. (4.34) are found the eddy event contributions to the transport at $y = 2\Delta Y$ ($S_{E_i}^{2,k-1}$) and $y = \Delta Y$ ($S_{E_i}^{1,k-1}$), and the molecular diffusion term evaluated at the top of the ODT domain ($S_{D_i}^{1,k-1}$). Similarly, wall-normal advection terms for $y = 2\Delta Y$ are found on line 4 (where both γ_k and ζ_k Runge-Kutta contributions are represented) and the ODT advective term for $y = \Delta Y$ ($S_{A_i}^{1,k-1}$) is on line 5.

For all other LES volumes located within the overlap region (denoted by the superscript n, with $n > 2$), Eq. (4.26) is revised to look as follows:

$$\frac{\hat{\bar{u}}_i^k - \bar{u}_i^{k-1}}{\Delta t} = \quad \alpha_k\mathbf{L}_y(\bar{u}_i^{k-1}) + \beta_k\mathbf{L}_y(\hat{\bar{u}}_i^k) - \frac{(\alpha_k+\beta_k)}{\Delta x_2}\left(S_{E_i}^{n,k-1} - S_{E_i}^{n-1,k-1}\right)$$

$$+(\alpha_k+\beta_k)\mathbf{L}_{xz}(\bar{u}_i^{k-1})-\gamma_k\mathbf{N}(\bar{u}_i^{k-1})-\zeta_k\mathbf{N}(\bar{u}_i^{k-2})$$
$$-(\alpha_k+\beta_k)\tfrac{1}{\rho}\tfrac{\delta\bar{P}^{k-1}}{\delta x_i}-(\alpha_k+\beta_k)\tfrac{PG_i}{\rho}. \tag{4.36}$$

Note that the only difference between Eq. (4.26) and Eq. (4.36) is the addition of wall-normal transport terms coming from the ODT eddy events crossing LES boundaries as computed in part 1.

For LES volumes located outside of the LES/ODT overlap region, Eq. (4.26) is solved without modification.

4.4.3 Details of part 3

Part 3 requires values for the interim LES velocity field at all locations. To obtain these values in the ODT inner region, we apply Eq. (4.13) to the ODT advecting velocities, as follows:

$$\hat{\bar{u}}_i^k\Big|_{\text{inner region}}=\hat{\bar{V}}_i\equiv\frac{1}{N_{\text{ODT}}}\sum_{m=1}^{N_{\text{ODT}}}\hat{V}_{i,m} \tag{4.37}$$

for $i=1$ and 3. Equation (4.37) is not valid for the wall-normal velocity, $i=2$, because of the definition of the ODT control volumes and locations as illustrated in Figs. 32 and 34. At the top of the inner region, the control surface through which the ODT advecting velocity $V_2|_{y=\Delta Y}$ fluxes fluid corresponds exactly to the LES interface through which the LES velocity component $\bar{u}_2$ fluxes fluid. The LES velocity is spatially filtered over a height ΔY, but the ODT advecting velocity corresponds to a cell of height $\Delta Y/N_{\text{ODT}}$. For use in part 3, the ODT velocity is actually a more accurate approximation for the desired quantity because it is determined by enforcement of continuity, Eq. (4.18), reflecting ODT evolution since the previous LES time step. Thus we simply set

$$\hat{\bar{u}}_2^k\Big|_{\text{inner region}}=\hat{V}_2|_{y=\Delta Y}. \tag{4.38}$$

.

Part 3 begins by solving the discrete Poisson equation, Eq. (4.29), for ϕ. Knowing ϕ^k, Eq. (4.28) is integrated (with the rightmost term omitted, as explained in Section 4.3) to compute the change in pressure from $k-1$ to k. The new pressure is then given by

$$\bar{P}^k=\bar{P}^{k-1}+\frac{\rho\phi^k}{\alpha_k+\beta_k}. \tag{4.39}$$

Next, Eq. (4.27) can be applied to solve for the new velocity field:

$$\bar{u}_i^k=\hat{\bar{u}}_i^k-\Delta t\frac{\delta\phi^k}{\delta x_i}. \tag{4.40}$$

As indicated by Eqs. (4.37) and (4.38), $\hat{\bar{u}}_i^k$ in the inner region is determined solely by ODT quantities.

4.4.4 Details of part 4

The fourth and final part of the cycle consists of adjusting the ODT-resolved profiles of $\hat{V}_i^k(y)$ and $\hat{v}_i^k(y)$ to be consistent with the new pressure-adjusted velocity field in the inner region, but without significantly modifying the microstructure of the ODT profiles. Fig. 35 is useful in explaining how this is done.

Consider an ODT advective velocity field $\hat{V}_i^k(y)$ in the inner region after the completion of part 1. Since it has not yet been adjusted by the pressure-projection procedure, this profile is denoted with a hat. It has an average value $\hat{\bar{V}}_i^k$ (see Eq. (4.37)), but may have an irregular variation with y. A linear profile can be drawn from $y = 0$ to $y = \Delta Y$ that passes through the value $\hat{\bar{V}}_i^k$ at exactly $y = \Delta Y/2$. At any location y from the wall, one can compute a difference or 'variation' between the local value of $\hat{V}_i^k(y)$ and this linear function.

After part 3 is completed, a new adjusted value for $\bar{u}_i^k$ in the inner region is known. For $i = 1$ and 3, we impose the requirement that the difference (as a function of y) between the new $V_i^k(y)$ and the line $2\bar{u}_i^k y/\Delta Y$ is the same as the difference function $\hat{V}_i^k(y) - 2\hat{\bar{V}}_i^k y/\Delta Y$. Put another way, we obtain $V_i^k(y)$ by adding a linear profile to $\hat{V}_i^k(y)$ that enforces $\bar{V}_i^k = \bar{u}_i^k$, where the left-hand side of this equality represents the average of $V_i^k(y)$ over $0 \le y \le \Delta Y$, as defined by Eq. (4.13). This gives

$$V_i^k(y) - 2\frac{\bar{u}_i^k y}{\Delta Y} = \hat{V}_i^k(y) - 2\frac{\hat{\bar{V}}_i^k y}{\Delta Y} \tag{4.41}$$

for $i = 1$ and 3. After $V_1^k(y)$ and $V_3^k(y)$ are found, $V_2^k(y)$ is computed using Eq. (4.18).

To preserve the relationship between instantaneous and time-filtered ODT velocities when this adjustment is performed, the ODT instantaneous velocity profiles are adjusted based on the relationship

$$v_i^k(y) - 2\frac{\bar{u}_i^k y}{\Delta Y} = \hat{v}_i^k(y) - 2\frac{\hat{\bar{V}}_i^k y}{\Delta Y} \tag{4.42}$$

for $i = 1$ and 3. $v_2^k(y)$ is not adjusted because it is not kinematically linked, through relations like Eqs. (4.31) and (4.37), to LES-scale processes.

At the end of part 4, all values have been advanced from LES sub-time-step $k-1$ to k.

4.4.5 Remarks

The LES/ODT subprocesses and couplings are formulated to be complementary, each providing the other with the information needed to simulate flow evolution within the range of scales that it represents. However, we note here that neither the ODT momentum equation, Eq. (4.14), nor the adjustment in part 4 communicates the large-scale forcing to the wall-normal ($i = 2$) ODT velocity component. It is neither necessary nor desirable to couple v_2 to these forcings. Continuity is sufficient to determine the advective velocity V_2 that provides an LES-scale representation of the effect of ODT evolution on wall-normal flow. As

in ODT stand-alone implementation, v_2 is a kinetic-energy reservoir that is incorporated to improve the fidelity of the ODT representation of energy transfers among the three velocity components. Owing to the distinctive role of v_2 in the formulation of the ODT event-rate distribution, v_2 may have additional physical significance in future applications to transition and other phenomena that are sensitive to details of this formulation.

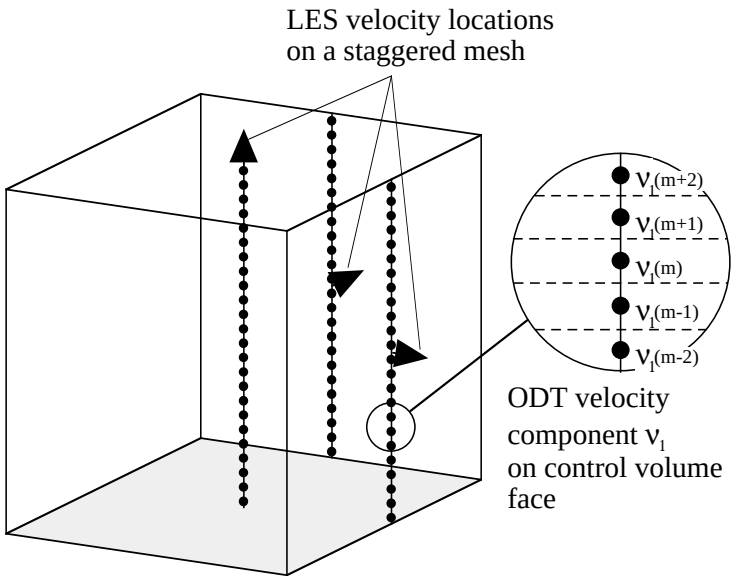

Figure 34: Spatial location of LES and ODT velocity components on a staggered grid.

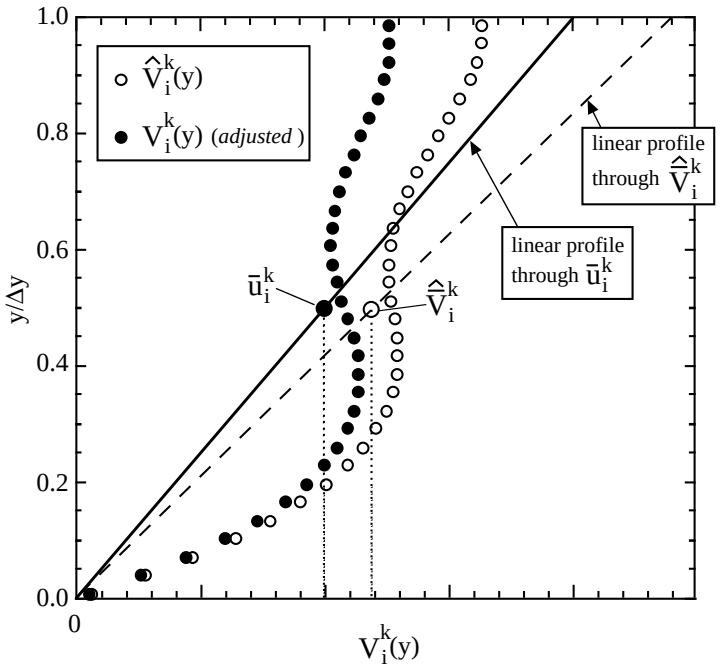

Figure 35: Illustration of how an ODT velocity field is adjusted following a pressure-projection update.

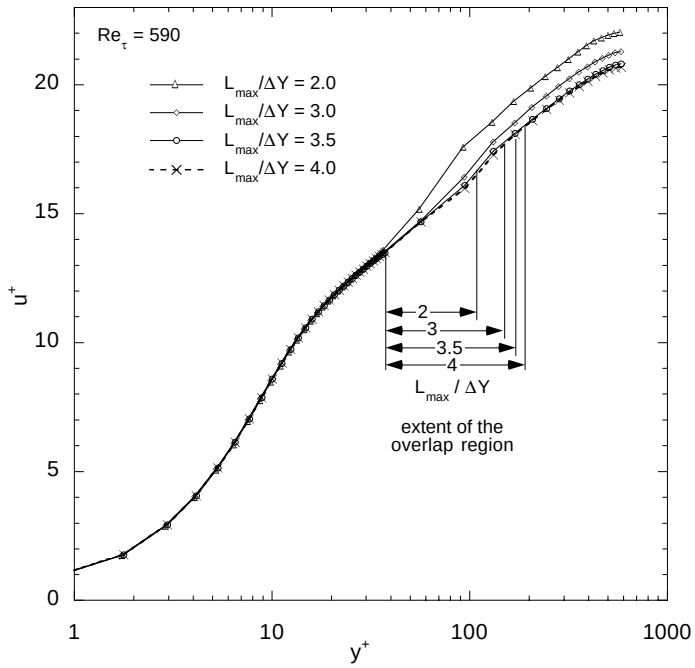

Figure 36: Sensitivity of the LES/ODT mean velocity profiles to different values of $L_{\max}$.

4.5 Coupled LES/ODT Simulations of Turbulent Channel Flow

Fully developed turbulent channel flow has been studied extensively in the past and both experimental [13, 77] and numerical DNS data [55] are available for comparison purposes. Stand-alone ODT results for this flow are presented in Section 4.1.4. Here we present results based on the coupled LES/ODT model.

The LES computational domain is 2π, $2\pi/3$, and 2 in the streamwise (x), spanwise (z), and wall-normal (y) directions, respectively. Calculations were performed at Reynolds numbers based on friction velocity ranging from 395 to 10,000 in order to test the modeling over a wide range of Reynolds numbers. For all but the highest-Reynolds-number flows considered, the domain is discretized by a relatively coarse but uniform $32 \times 32 \times 32$ grid in the streamwise, spanwise, and wall-normal directions. As the Reynolds number is increased, a smaller portion of the total kinetic energy is captured on the LES grid. Thus for the higher Reynolds-number flows the resolution was increased and a uniform $48 \times 48 \times 64$ discretization was used. Although more refined LES meshes could have been chosen, one purpose of this work is to test the new approach under coarsely meshed LES conditions in order to determine if the ODT subgrid modeling can still be usefully applied. To resolve the ODT domain properly, an ODT near-wall mesh spacing of approximately 1 wall unit (y^+) was found to be sufficient to achieve grid-independent results.

To perform a set of coupled LES/ODT calculations, the ODT model constants C, Z, α, and $L_{\max}$ must be specified. $\alpha = 2/3$ is used for all results shown in this section, and Z is again assigned the value 98. These values, together with the choice $C = 12.73$, yield a good fit of DNS data by stand-alone ODT (Section 4.1.4). For LES/ODT, it is found that a slightly lower value of the overall rate constant, $C = 9.9$, is the best value for matching the DNS mean velocity profile at $Re_\tau = 590$. This adjustment reflects the impact of the large scale LES forcings on the ODT model when coupled together. Although the adjustment is relatively small, it nevertheless is sufficient to imply a distinction between the coupling of near-wall and bulk regions in stand-alone ODT and LES/ODT, respectively.

The coupled LES/ODT model requires a different approach for determining the maximum eddy length parameter, $L_{\max}$, than was used when doing stand-alone ODT calculations. This is because the integral length scale of the flow (e.g, the channel width) is no longer an appropriate measure of this parameter. Instead, $L_{\max}$ is now associated with the LES filter width, and determines the length of the overlap region (as illustrated in Fig. 31). It corresponds physically to the largest length scale captured by ODT, and should also correspond approximately to the smallest length scales resolved by the LES. Thus, one can also think of an overlap region of length scales in which both ODT and LES models are active.

To determine the appropriate value of $L_{\max}$, a simple parametric sensitivity study was performed. Fig. 36 illustrates the results of this exercise for flow at $Re_\tau = 590$. Four different

Case	Re_τ	Re	N_{ODT}	$\Delta y^+_{\mathrm{ODT}}$	N_x	N_y	N_z
A	395	14020	24	1.03	32	32	32
B	590	22472	32	1.17	32	32	32
C	1200	49336	64	1.17	32	32	32
D	2400	108624	128	1.17	32	32	32
E	4800	234332	128	1.17	48	64	48
F	10000	534224	256	1.17	48	64	48

Table 1. Computed cases.

simulations were performed, keeping all other values and conditions constant except for the value of $L_{\max}$. A large change is seen as $L_{\max}$ is increased from $2\Delta Y$ to $3\Delta Y$, but very little difference is seen as its value is increased from $3.5\Delta Y$ to $4\Delta Y$. These results are consistent with the notion that this value should correspond approximately to the smallest length scales resolved by the LES on the numerical mesh. For all other calculations shown here we use the value $L_{\max} = 3.5\Delta Y$.

Table 1 summarizes six calculations performed as a test of the current LES/ODT coupled model. In each of these runs, the values of C, Z, α, and $L_{\max}$ were held fixed at the values specified above. In each case, the simulation was started by specifying a randomly perturbed initial velocity profile and then allowing the computation to proceed without taking statistics until the initial transient behavior had settled out and the time-averaged wall stress balanced the mean pressure gradient exactly. This typically occurred within several hundred non-dimensional time units (based on bulk velocity and channel half width). Statistics were then taken over non-dimensional time periods of about 300 time units. As a final check, the calculations were then continued over a similar time period and the results compared so as to assure that the statistics were adequately converged.

All calculations were performed on single-processor SGI workstations with run times varying from several hours for the lower-Reynolds-number flows to several days for the highest-Reynolds-number flows. However, extensive optimization of the code and model algorithms has not yet been attempted, and some improvement in run times would be expected when this is done.

Figure 37 helps illuminate the dynamics of the coupled LES/ODT model by showing near-wall mean and instantaneous velocity profiles for an illustrative calculation at $Re_\tau = 1200$. In contrast to the smoothly varying time-averaged profile that is shown, instantaneous profiles are highly irregular. Of particular note are the wrinkling effects of eddy events on the velocity profiles in the ODT inner region. At the particular instant shown, the effects of both large

and small eddy events can be clearly seen. Furthermore, the smoothing effect of molecular processes over time can be seen and contrasted to the sharp gradients imposed by recent eddy events.

Figure 38 presents LES/ODT model results for the mean velocity profiles over the Reynolds-number range indicated in Table 1. For cases A and B, the DNS data of Moser *et al.* [55] are available and are used for direct comparison. For all cases, the inner law ($u^+ = y^+$) and a commonly accepted [13] log law ($u^+ = 2.44 \ln(y^+) + 5.2$) are also plotted for comparison. Data symbols are used to denote LES/ODT node-point values in order to highlight the increased resolution of the model in the ODT domain.

At all Reynolds numbers, the simulations produce a physically realistic viscous sublayer smoothly transitioning through the buffer zone into a log layer. At the edge of the overlap region (between the second and third LES nodal values), a slight rise in the mean profile can be noticed in the lower-Reynolds-number cases. This is likely due to imperfect transitioning from ODT-based modeling of the turbulent transport to the LES modeling in the overlap region. This aspect may improve with model refinement. At the highest Reynolds numbers (cases E and F), the mean profile in the LES region above the ODT domain is somewhat high. It is not clear yet why this occurs, but it may reflect under-resolved LES effects coupled to imperfections in the overlap-region transition to the ODT near-wall domain. Further investigation will be needed to better understand the performance of the coupled model at these higher Reynolds numbers. Overall, the coupled LES/ODT model performs remarkably well at reproducing the mean velocity profiles for this flow and compares very favorably with other recent work in this area (e.g., [57, 42, 60]).

Figure 39 is a plot of the friction coefficient as a function of Reynolds number. The LES/ODT results, extending over a wide range of the bulk-flow Reynolds number, are in good agreement with DNS and experimental results. At the highest Reynolds numbers (cases E and F), the LES/ODT results suggest a trend that is slightly high compared to the correlation of Dean [13]. The source of this difference is most likely due to the poor LES resolution of the wake region, leading to a comparatively lower bulk velocity and thus a higher friction coefficient (see [9] for a discussion of this topic).

Figures 15-19 are plots of root-mean-square (RMS) velocity fluctuation profiles, normalized by u_τ. These results are important because they help characterize the near-wall dynamic behavior that cannot be obtained from low-order RANS-based models. The dynamic fluctuations that are reflected in these profiles are also important to multiphysics applications where physical processes such as heat transfer and chemical reactions are strongly affected.

In Fig. 40 LES/ODT computed RMS velocity fluctuation profiles at $Re_\tau = 590$ are compared with the DNS calculations of Moser *et al.* [55] and results of the previously discussed stand-alone ODT calculations (Section 2.4). We begin by noting that overall, the magnitudes and shapes of the LES/ODT RMS velocity fluctuation profiles compare quite favorably with DNS and show noticeable improvement over stand-alone ODT results. This

improvement reflects the impact of large scale LES forcings on the ODT model when coupled together, and highlights the complementary nature of the combined modeling approach.

In comparing LES/ODT results for $u_{\rm rms}$ with DNS, we can see (1) perfect agreement for $y^+ < 9$, (2) a somewhat flattened peak region where the LES/ODT results are about 10 percent lower than DNS, (3) good agreement (although slightly high) in the central channel region ($y^+ > 200$), and (4) a rise of LES/ODT values compared to DNS as the wall is approached from the central region, but a return to the DNS profile in the LES/ODT overlap region. Elevated values of $u_{\rm rms}$ near the wall are symptomatic of under-resolved LES (e.g., Kravchenko *et al.* [42]), and this figure illustrates clearly how the ODT subgrid model coupling acts to suppress this problem.

For stand-alone ODT only a single profile is plotted for both wall-normal $v_{\rm rms}$ and spanwise $w_{\rm rms}$ velocity fluctuations because in the current three-component model, the statistics for these two components are identical and their near-wall behavior is intermediate between the DNS data for $v_{\rm rms}$ and $w_{\rm rms}$. However, for LES/ODT the profiles are not identical because they couple to distinctly different LES velocity fields. This can be seen in Fig. 40 where very near the wall, the profiles are almost identical, but as the top of the inner region is approached and the coupling to LES becomes stronger, the profiles diverge. We also note a small dip in the $w_{\rm rms}$ profile at the upper edge of the inner region, and a subsequent discontinuity in the slope (also seen in each of the other profiles). This reflects the abrupt jump from a finely resolved ODT mesh to the much coarser LES mesh and may be associated with the rather simple interfacial boundary conditions applied.

In Fig. 41, LES/ODT results for $u_{\rm rms}$ from simulations at six Reynolds numbers are compared to the DNS results of Moser *et al.* [55] and the data of Wei and Willmarth [77]. (Unfortunately, reliable near-wall data for RMS velocity fluctuations are not currently available for channel flow at high Reynolds numbers comparable to Cases E and F.) This figure illustrates that most of the characteristics pointed out in commenting on Fig. 40 remain apparent for all cases considered. All cases collapse to a single curve for $y^+ < 9$, and show a somewhat suppressed and flattened peak region relative to DNS and measurements. One trend of note is the clear transition from scaling on inner variables very near the wall to the qualitatively correct Reynolds number dependence away from the wall. Although not plotted here, away from the wall all cases collapse to a single curve if plotted in global coordinates (y) [37] and show good agreement with the DNS and experimental data.

In Fig. 42, LES/ODT results for $w_{\rm rms}$ are shown. The DNS results of Moser *et al.* [55] are once again plotted for comparison with the lower Reynolds number cases. (Note that $w_{\rm rms}$ data was not obtained by Wei and Willmarth [77]). Although the very near-wall (i.e. $y^+ < 9$) LES/ODT profiles are consistently lower than the DNS results, the slight Re dependence shown by the DNS results even at the lowest values of y^+ is captured by the LES/ODT model. As with the $u_{\rm rms}$ results, the peak region is flattened, but the profiles converge rapidly to their expected values away from the wall where LES is unmodified by the near-wall subgrid

model.

Figure 43 is a plot of $v_{\rm rms}$ that shows LES/ODT results, the DNS results of Moser *et al.* [55] and the data of Wei and Willmarth [77]. Here the LES/ODT profiles are consistently higher than the DNS data in the inner region, diverge from scaling on inner variables at a smaller value of y^+, and peak at a lower value of y^+ - once again reflecting the intermediate nature of the ODT $v_{\rm rms}$ component between the DNS $v_{\rm rms}$ and $w_{\rm rms}$. At the top of the inner region, the profiles tend to dip, due to the stronger coupling to the LES. In the overlap region the profiles gradually converge to the LES dominated behavior, which is broadly consistent with the available data in the central portion of the channel.

In constructing the LES/ODT subgrid model a set of advecting velocities are defined in Section 4.6. V_1 and V_3 are based directly on v_1 and v_3 respectively (see Eq.(48)), and results show that the RMS velocity fluctuation profiles based on V_1 and V_3 are virtually the same as the RMS profiles based on for v_1 and v_3. However, the advecting wall-normal velocity component V_2 is based on satisfying continuity in the ODT sub-control volumes (see Eq. (35)), and is not directly tied to the ODT component v_2. Figure 44 is identical to Fig. 43 except that $V_{\rm rms}$ is plotted in the inner region instead of $v_{\rm rms}$. As can be seen, these profiles are quite different. Here we see that the LES/ODT values for $V_{\rm rms}$ are consistently lower than the DNS data. In fact, the DNS data falls intermediate between the values for $V_{\rm rms}$ shown here and the values for $v_{\rm rms}$ shown in Fig. 43. Also of note is the strong Reynolds number dependence of $V_{\rm rms}$ even in the very near-wall region. This points out that V_2 is subject to large-scale influences even near the wall, which may be an artifact of the LES-scale averaging (V_2 is an average over a X-Z face as illustrated in Fig. 7) or the simple profile assumptions made in constructing the velocity adjustment described in Section 4.6.4. In this context, V_2 may be viewed as an auxiliary quantity used to enforce continuity. v_2 provides a better, though approximate, representation of wall-normal point-value flow statistics.

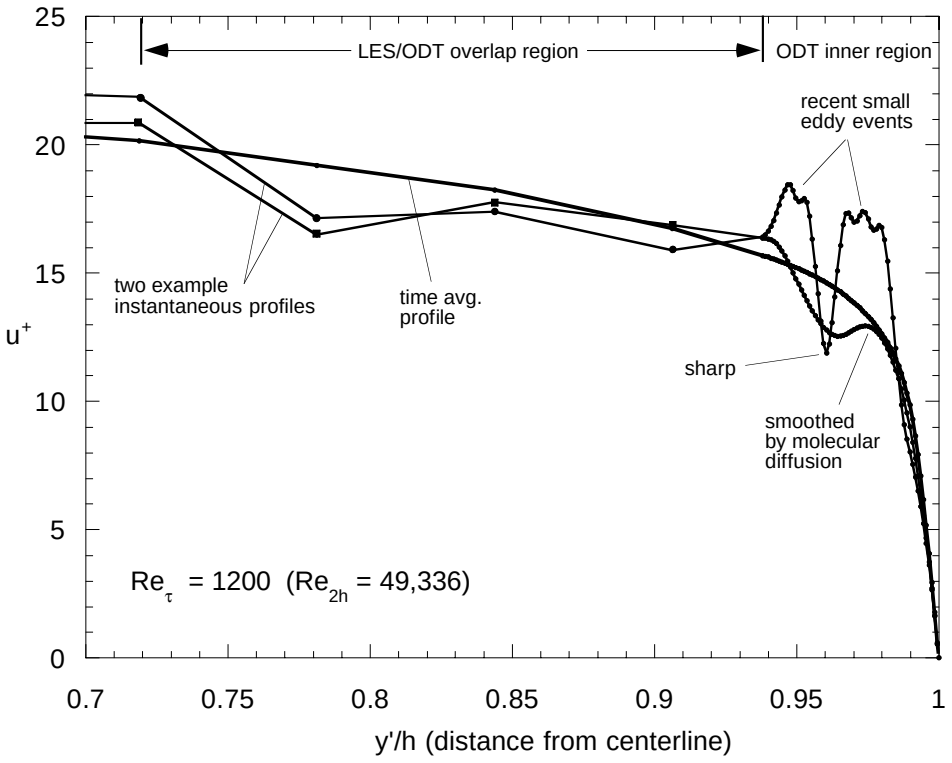

Figure 37: Near-wall mean and sample instantaneous velocity profiles.

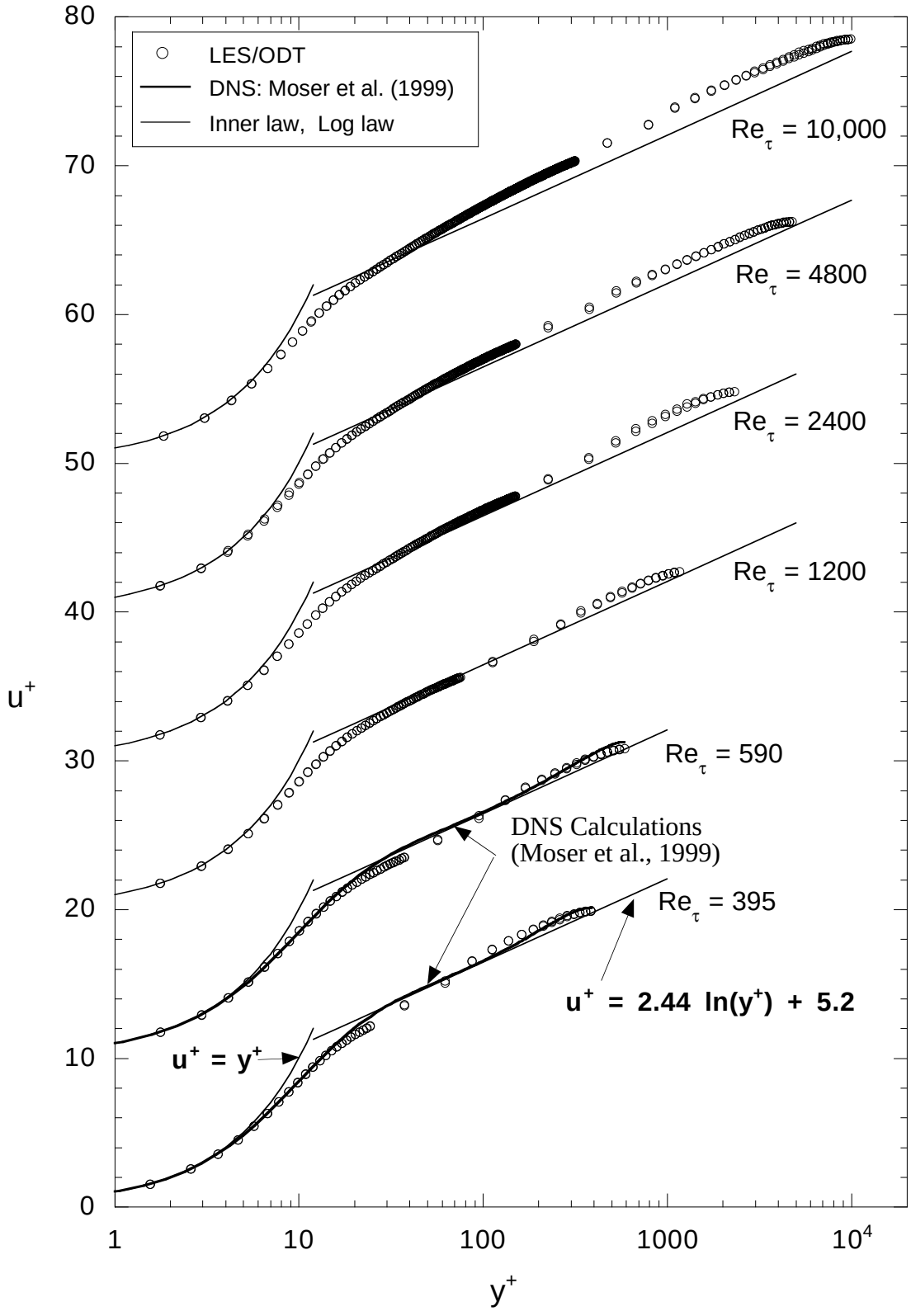

Figure 38: Semilog plot of LES/ODT mean velocity profiles for a range of Reynolds numbers. Successive profiles are vertically displaced for clarity. Pairs of overlapping symbols reflect the folding of the computed profiles for the two channel walls onto a single profile.

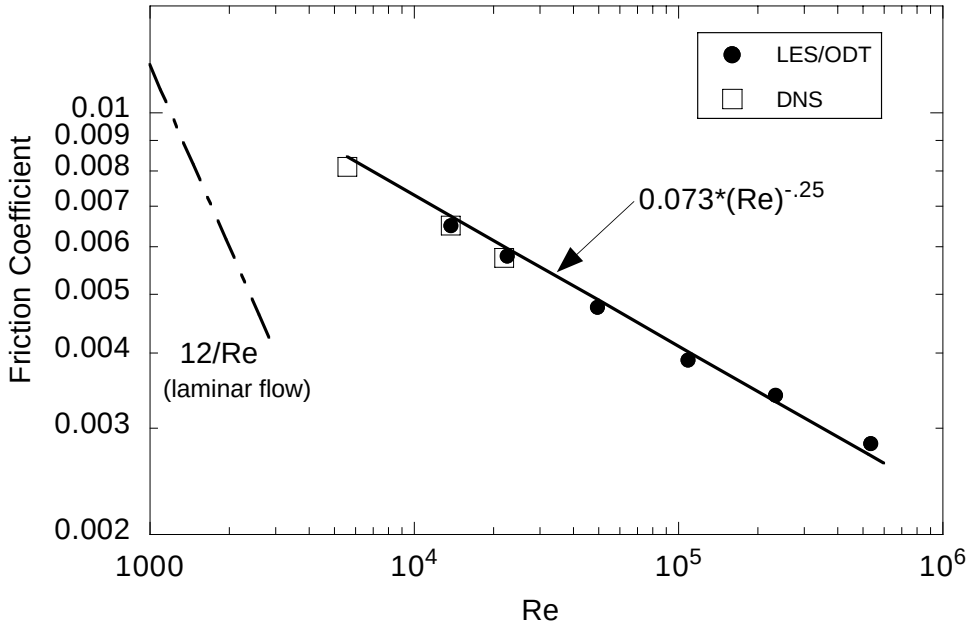

Figure 39: LES/ODT computed friction coefficient for channel flow compared to DNS data [55] and the correlation of Dean [13]. Here, Re is based on the bulk velocity and the channel width ($2h$).

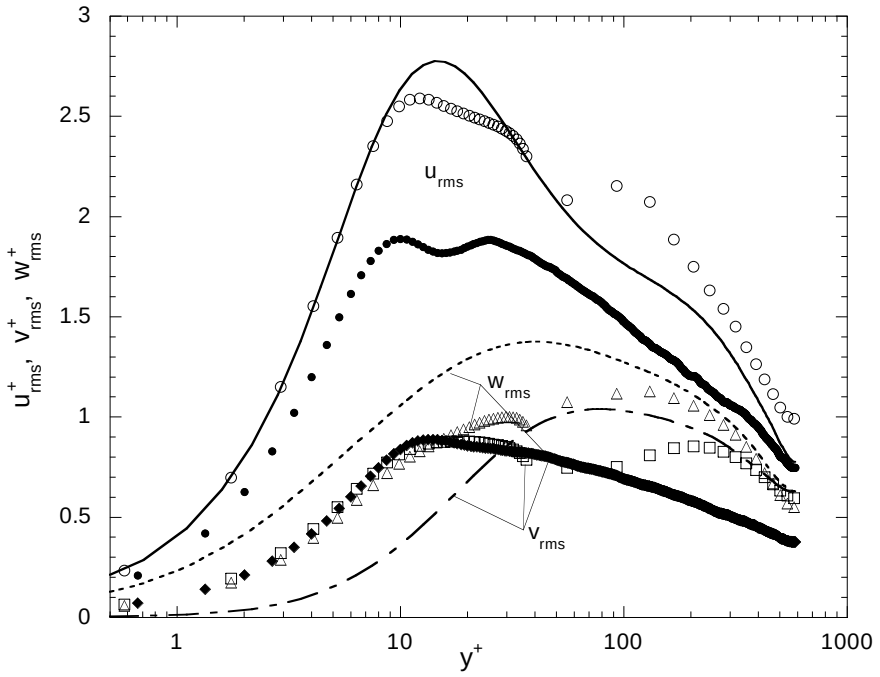

Figure 40: Root-mean-square velocity fluctuation profiles normalized by the friction velocity for $Re_\tau = 590$ and computed from LES/ODT (open symbols), ODT stand-alone (filled symbols), and DNS [55] (solid and dashed lines).

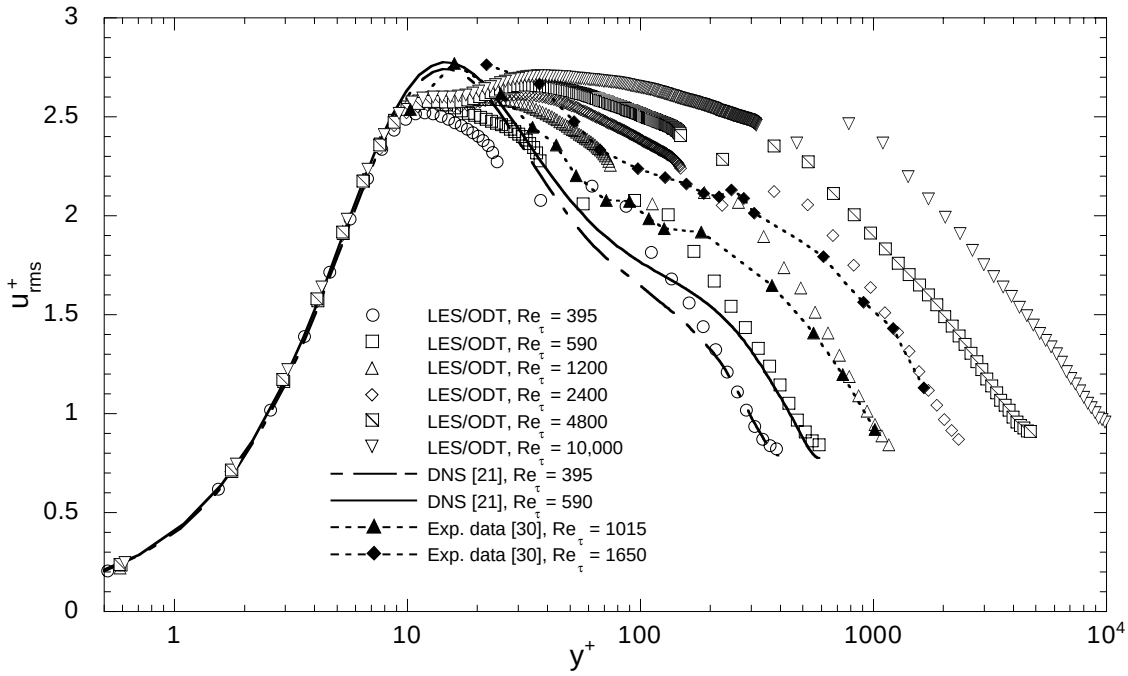

Figure 41: Streamwise root-mean-square velocity fluctuation profiles normalized by the friction velocity.

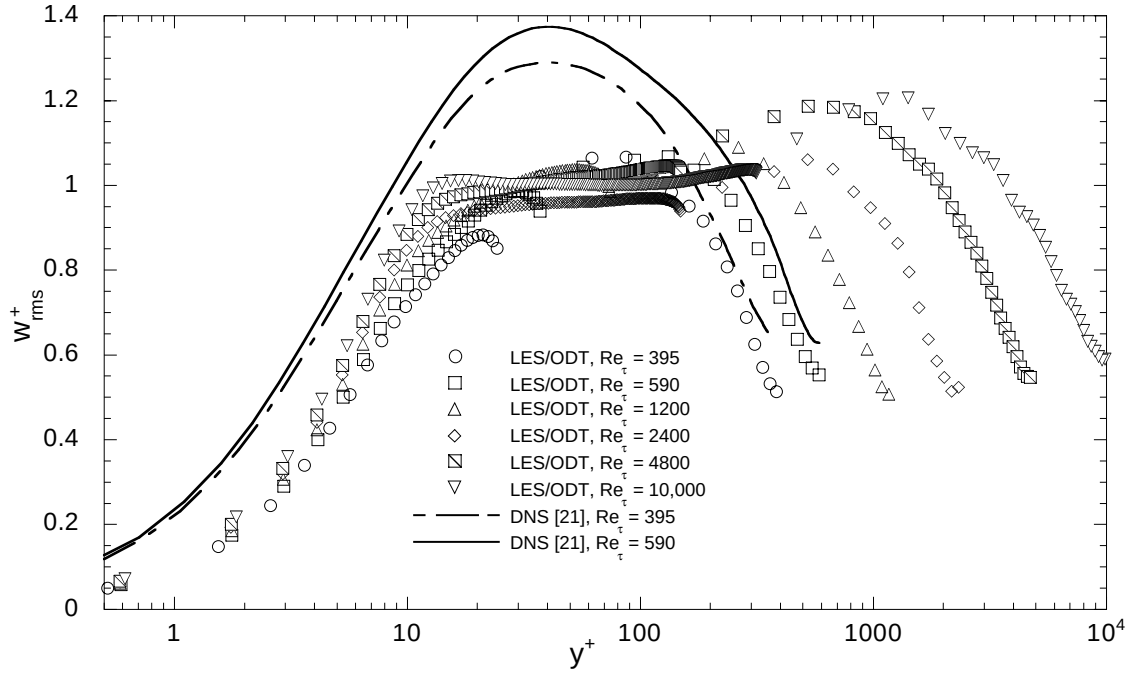

Figure 42: Cross-stream root-mean-square velocity fluctuation profiles normalized by the friction velocity.

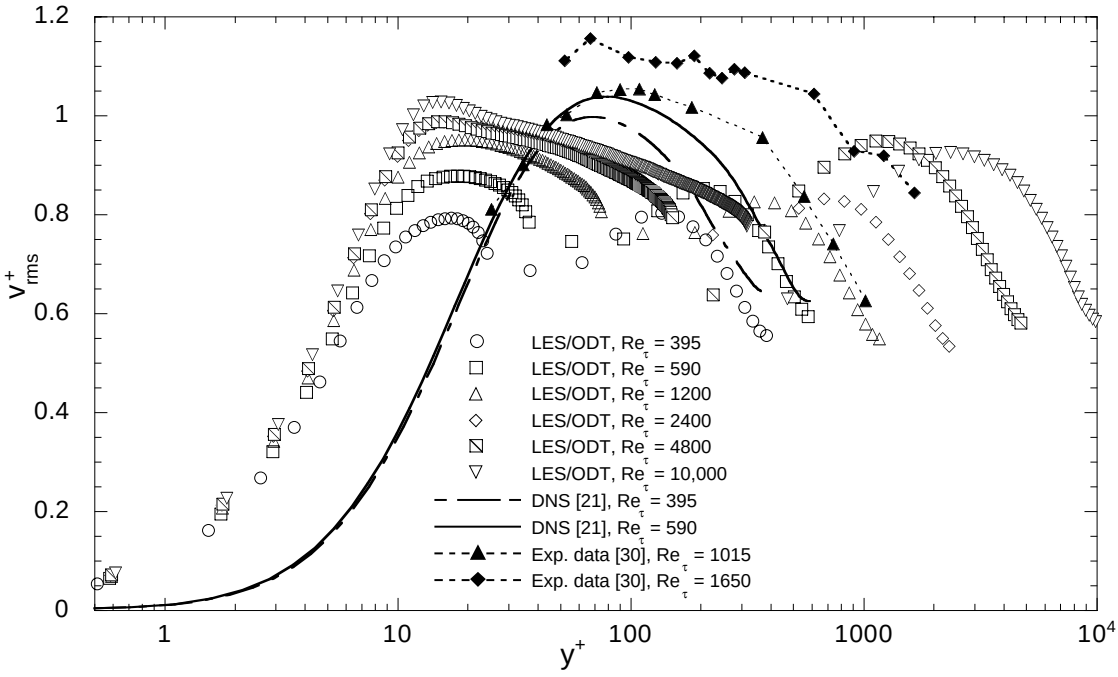

Figure 43: Wall-normal root-mean-square velocity fluctuation profiles normalized by the friction velocity.

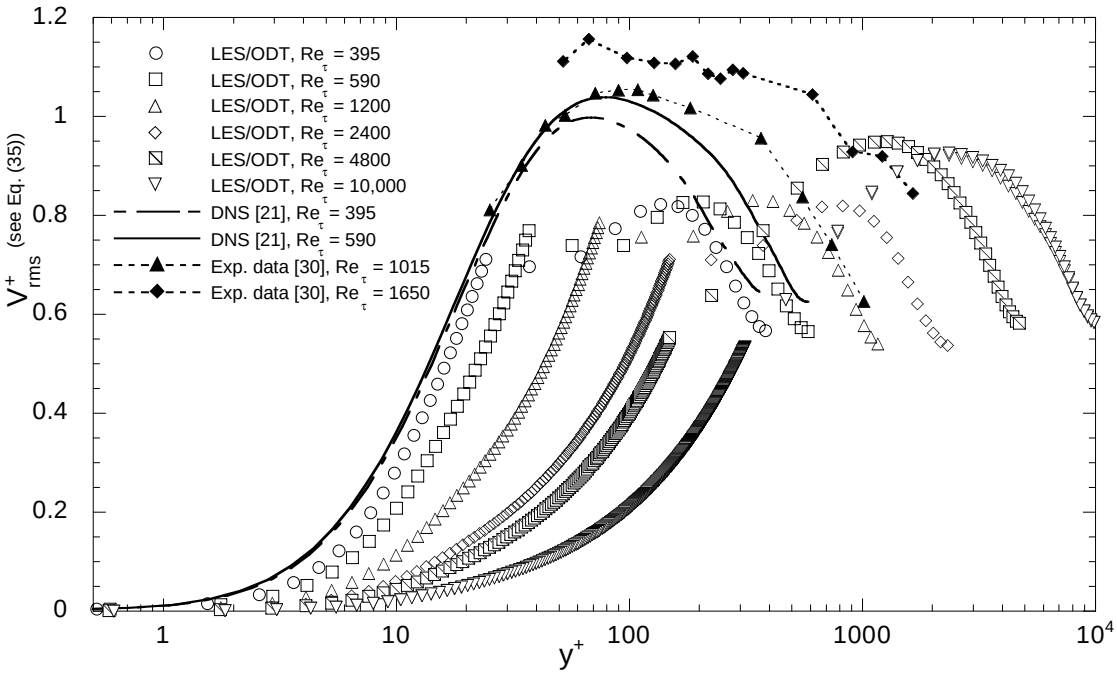

Figure 44: Wall-normal root-mean-square velocity fluctuation profiles normalized by the friction velocity. Inner region values taken from the advecting velocity defined by Eq. (35).

4.6 LES/ODT Simulations of Turbulent Flow over a Backward Facing Step

To be more generally useful as a near-wall model, the ODT approach must be shown to be valid for a variety of near-wall flow conditions. Turbulent impinging flows, developing boundary layers, flow separation and reattachment are all examples of important flow conditions for which the new approach should be tested and evaluated.

Here we present results of some preliminary calculations of a reattaching turbulent shear layer generated as a result of flow over a backward facing step. The conditions are for one of the cases studied experimentally by Kim, Kline and Johnston [38, 39]. For the case simulated, the ratio of step height H to inlet channel width W_{in} is 0.5 and the Reynolds number based on W_{in} and the inlet bulk flow velocity is 90,000.

This problem was chosen as a preliminary test of the model for the following reason. By starting the computational domain at the step plane, the same computer code as was used for the fully developed channel flow problem could be used with only a few modifications. The key change is that the flow is no longer periodic in the stream-wise flow direction. Thus for this problem the inflow boundary conditions must be specified, outflow boundary conditions treated properly, and the flow solver modified to account for the fact that the flow is periodic in only one direction.

Figure 4.6 illustrates the computational domain used in the simulations. A uniform mesh of 64x48x32 in the streamwise (X), vertical (Y), and transverse (Z) direction was used. The inlet velocity was curve fit to the experimental data, and was specified as constant in time. The mesh was not refined near the vertical plane, which means that the shear layer emanating from the inlet at the top of the step was not resolved in the calculation. However, this is not important for the purposes of this preliminary calculation as the intent was to determine of the near wall model worked in the region near the reattachment point, independent of exactly where that point occurred.

All control volumes adjacent to either the upper or lower walls are controlled by the ODT near-wall subgrid model, in which 45 ODT points per line are employed. The computational domain extends approximately 19 step-heights downstream from the inlet.

Even though the specified inflow is steady, the strong shear layer flowing off the step invokes a strongly unsteady flow field downstream. This is illustrated in Figure 4.6a which shows the instantaneous streamwise velocity field at the channel midplane. Also shown are the time averaged values of the streamwise velocity component, an instantaneous snapshot of the pressure field averaged through the channel, and the flow stream lines computed from the time averaged velocity field.

The results of the calculations demonstrate that the model appears to work as expected from a qualitative point of view. However, in order to fully test the model, calculations in the future will be made which include a significant portion of the upstream inlet flow domain. They will also resolve the shear layer after the step in order to access the accuracy of the

approach in computing the length of the recirculation zone, and provide statistical data with which to compare with the more detailed results of the experiment.

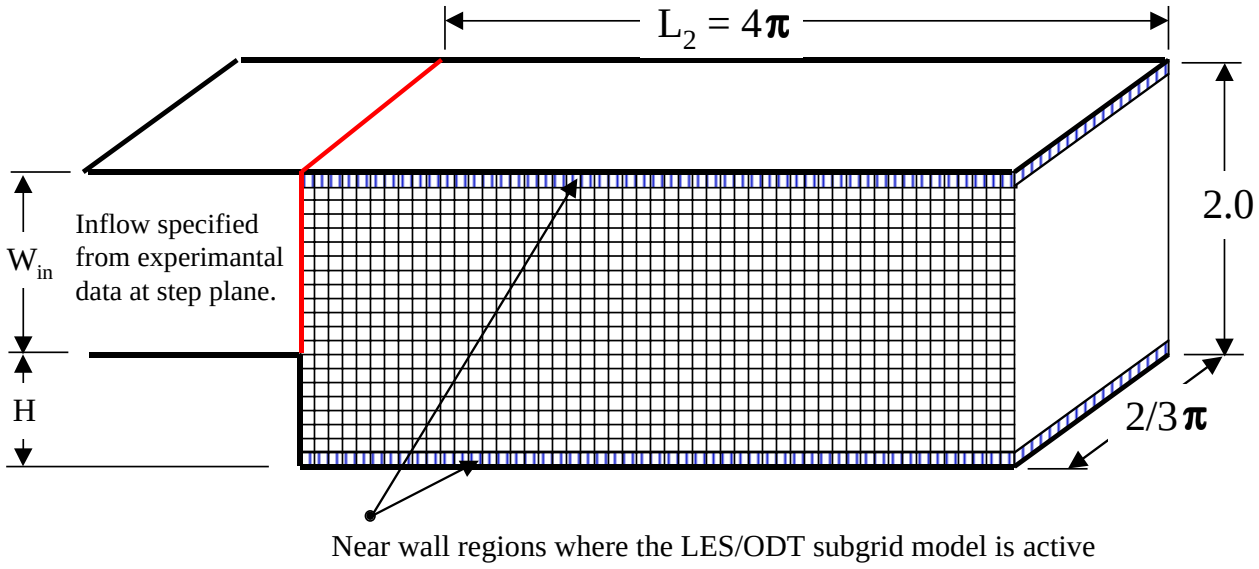

Figure 45: Sketch of the computational domain for the backward facing step problem (not to scale).

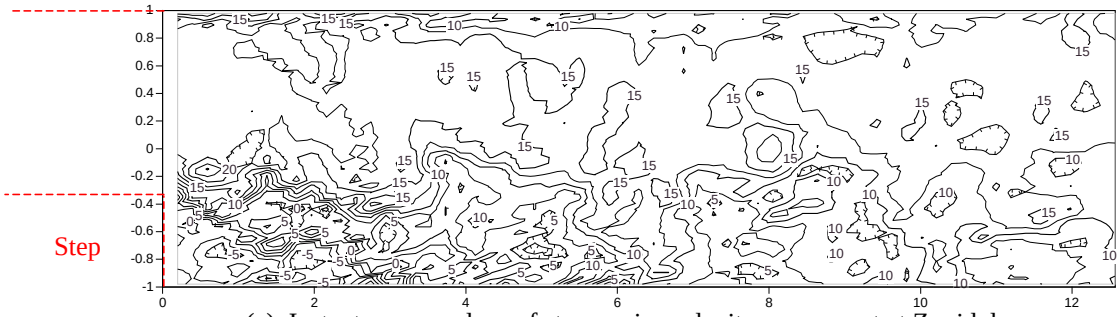

(a) Instantaneous values of streamwise velocity component at Z midplane

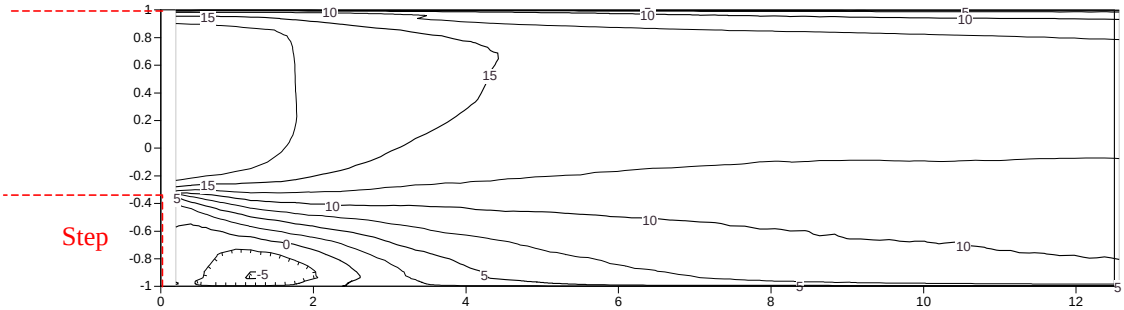

(b) Z-plane (spatial) and time averaged streamwise velocity component.

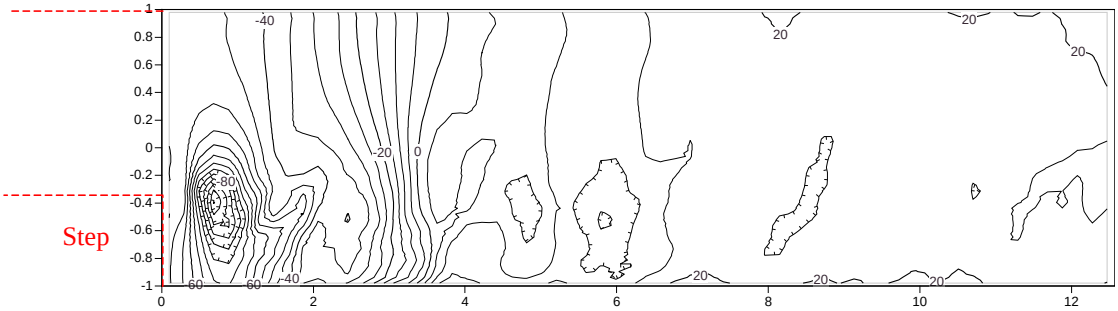

(c) Instantaneous pressure field spatially averaged in the Z-plane.

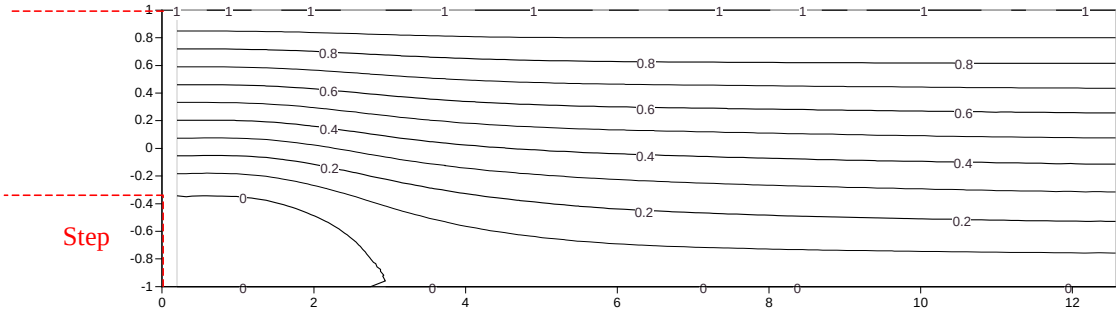

(d) Streamlines of the time averaged and spatially averaged velocity field

Figure 46: Visualization of results from LES/ODT simulations of the backward facing step problem. Note that the vertical scale is stretched in each plot.

A Spectral Behavior of RKPM Filters

Begin by considering the discrete fourier transform (DFT) of a periodic function, $H(x_i)$, on a one-dimensional domain of extent L. Discretizing the domain with Nnp particles spaced Δx apart, the inverse DFT is,

$$\widetilde{H}(k_l) = h(k_l) = \sum_{n=0}^{Nnp-1} H(x_n) \exp(-\iota k_l x_n) \Delta x_n, \tag{A.1}$$

where $\iota = \sqrt{-1}$ and $k_l = 2\pi j / L$ is the wavenumber associated with mode, l ($0 \leq l \leq Nnp - 1$).

Now, consider the RKPM reproducing equation in the one-dimensional domain,

$$u_j^a = \sum_{i=0}^{Nnp-1} u_i^I \overline{\phi^a}(x_j - x_i) \Delta x_i \tag{A.2}$$

where $u_i^I = u^I(x_i)$ is the original function, and $\overline{\phi^a}(\bullet)$ and $u_j^a = u^a(x_j)$ are the modified kernel function and resultant filtered function both at scale a. Recall that $a = r\Delta x$ on the discretized grid.

The spectral evaluation of Eq. (A.2) begins by placing the periodic waveform,

$$u_i^I = \sum_{l=0}^{Nnp-1} a_l \exp(\iota k_l x_i) \tag{A.3}$$

on the one-dimensional domain. Here a_l is the amplitude associated with mode l and k_l is defined above. Note that the summation in Eq. (A.3) over the modes, l, ranges from 0 through $Nnp - 1$. Modes higher than $Nnp - 1$ on the discrete particle distribution are aliased to the lower (discretely represented) modes when the continous $u^I(x)$ is sampled. Thus, even though $u^I(x)$ may be a continuous function, its representation u_i^I on the discrete grid is discrete and higher mode information is "lost". Substituting Eq. A.3 into Eq. A.2 yields,

$$u_j^a = \sum_{l=0}^{Nnp-1} \sum_{i=0}^{Nnp-1} a_l \exp(\iota k_l x_i) \overline{\phi^a}(x_j - x_i) \Delta x_i \tag{A.4}$$

Assuming that $\overline{\phi^a}((x_j + n\Delta x) - (x_i + n\Delta x)) = \overline{\phi^a}(x_j - x_i)$ where n is an integer (i.e. every modified kernel function looks like every other function) we may rewrite Eq. (A.4) as,

$$u_j^a = \sum_{l=0}^{Nnp-1} \sum_{i=0}^{Nnp-1} a_l \exp(\iota k_l x_j) \exp(-\iota k_l v_i) \overline{\phi^a}(v_i) \Delta v_i \tag{A.5}$$

where $v_i = x_j - x_i$ and $\Delta v_i = \Delta x_i$. Rearranging Eq. (A.5) we have,

$$u_j^a = \sum_{l=0}^{Nnp-1} a_l \exp(\iota k_l x_j) \sum_{i=1}^{Nnp-1} \exp(-\iota k_l v_i) \overline{\phi^a}(v_i) \Delta v_i. \tag{A.6}$$

Defining the individual *discrete* wave components of u_j^I to be $u_j^{I,l} = a_l \exp(\iota k_l x_j)$ and substituting Eq. (A.1) into Eq. (A.6) yields,

$$u_j^a = \sum_{l=0}^{Nnp-1} u_j^{I,l} \widetilde{\overline{\phi^a}}(k_l) = \sum_{l=0}^{Nnp-1} u_j^{a,l}, \tag{A.7}$$

where $u_j^{a,l} = u_j^{I,l} \widetilde{\overline{\phi^a}}(k_l)$ is the lth mode of u^I filtered though application of Eq. (A.2). Since u_j^a is a linear combination of $u_j^{a,l}$ we can use the amplification ratio of each individual mode,

$$AR_l = \frac{u_j^{a,l}}{u^{I,l}} = \widetilde{\overline{\phi^a}}(k_l) \tag{A.8}$$

as a measure of the filtering properties of $\overline{\phi^a}$ as a function of wavenumber of the input signal. Clearly, the DFT of the modified window function is directly related to the amplification ratio and is an appropriate measure of the attenuation of a signal passed though the *discrete* RKPM reproducing conditions (c.f. Eq. (A.2)).

Equation (A.8) provides a convenient way of calculating the amplification ratio for RKPM on a uniform grid of particles, where every modified kernel function "looking like" every other function. Of course, RKPM modified kernel functions, in general, do not look alike from location to location. Modified kernel functions vary in the domain with particle spacing, and near boundaries in order to ensure the desired reproducing conditions. For this reason, the assumptions leading to Eq. (A.8) are invalid and we must evaluate the amplification ratio directly. Employing Eq. (A.4) and recalling that u_j^a is a linear combination of the $u_j^{a,l}$ yields,

$$AR_l = \frac{u_j^{a,l}}{u_j^{I,l}} = \frac{\sum_{i=0}^{Nnp-1} \exp(\iota k_l x_i) \overline{\phi^a}(x_j - x_i) \Delta x_i}{\exp(\iota k_l x_j)}. \tag{A.9}$$

where $u_j^I = u_j^{I,0} AR_0 + u_j^{I,1} AR_1 + \cdots + u_j^{I,Nnp-1} AR_{Nnp}$. As an aside, note that a comparison of Eq.s (A.8) and (A.9) suggest that the right-hand-side of the later equation represents the DFT of some effective modified kernel function operating in the region around particle j. At this time, there is no indication that this is anything more than a curiosity.

References

[1] A. A. Aldama. *Filtering techniques for Turbulent Flow Simulation*, volume 56 of *Lecture notes in Engineering*. Springer-Verlag, Berlin, 1990.

[2] J. S. Baggett. On the feasibility of merging LES with RANS for the near-wall region of attached turbulent flows. *Annual Research Briefs 1998*, page 267, 1998. Center for Turbulence Research, Stanford University, Palo Alto, California.

[3] J. Bardina, J. H. Ferziger, and W. C. Reynolds. Improved subgrid scale models for large eddy simulation. *AIAA Paper 80-1357*, 1980.

[4] J. Bardina, J. H. Ferziger, and W. C. Reynolds. Improved subgrid scale models for large eddy simulation of homogeneous, incompressible, turbulent flows. Report TF-19, Thermosciences Division, Dept. of Mech. Engineering, Stanford University, 1983.

[5] G. K. Batchelor. *The Theory of Homogeneous Turbulence*. Cambridge University Press, 1953.

[6] R. W. Bilger. Reaction rates in diffusion flames. *Combustion and Flame*, 30:277–284, 1977.

[7] J. Boussinesq. *Mem. Pres. Acad. Sci.*, 113:9, 1877. Paris.

[8] W. Cabot. Large-eddy simulations with wall models. *Annual Research Briefs 1995*, page 41, 1995. Center for Turbulence Research, Stanford University, Palo Alto, California.

[9] W. Cabot, J. Jimenez, and J. S. Baggett. On wakes and near-wall behavior in coarse large-eddy simulation of channel flow with wall models and second-order finite-difference methods. *Annual Research Briefs 1999*, page 343, 1999. Center for Turbulence Research, Stanford University, Palo Alto, California.

[10] B. M. Cetegen and T. A. Ahmed. Experiments on the periodic instabilities of buoyant plumes and pool fires. *Combustion and Flame*, 93:157–184, 1993.

[11] M. Ciofalo. Large-eddy simulation: A critical survey of models and applications. *Adv. Heat Transf.*, 25:321, 1994.

[12] G. Comte-Bellot and S. Corrsin. Simple eulerian correlation of full-and narrow band velocity signals in grid-generated 'isotropic' turbulence. *Journal of Fluid Mechanics*, 48:273–337, 1971.

[13] R. B. Dean. Reynolds number dependence of skin friction and other bulk flow variables in two-dimensional rectangular duct flow. *J. Fluids Eng. Trans. ASME*, 100:215, 1978.

[14] P. E. DesJardin. *Large Eddy Simulation of Strongly Radiating Nonpremixed Turbulent Jet Flames*. PhD thesis, School of Mechanical Engineering, Purdue University, West Lafayette, IN, 1998.

[15] P. E. DesJardin and S. H. Frankel. Two-dimensional large eddy simulation of soot formation in the near-field of a strongly radiating nonpremixed acetylene-air turbulent jet flame. *Combustion and Flame*, 119:121–132, 1999.

[16] P. E. DesJardin, T. M. Smith, and C. J. Roy. Numerical simulations of a methanol pool fire. *AIAA Paper 2001-0636*, 2001.

[17] J. K. Dukowicz and A. S. Dvinsky. Approximate factorization as a high-order splitting for the implicit incompressible flow equations. *J. Comput. Phys.*, 102:336, 1992.

[18] J. R. Edwards. A low-diffusion flux-splitting scheme for navier-stokes calculations. *Computers and Fluids*, 26:635–659, 1997.

[19] J. R. Edwards and C. J. Roy. Preconditioned multigrid methods or two-dimensional combustion calculations at all speeds. *AIAA Journal*, 36:185–192, 1998.

[20] T. D. Blacker et al. Cubit mesh generation environment. SAND94-1100 Revised, Sandia National Laboratories, 1994.

[21] I. Fedioun, N. Lardjane, and I. Gokalp. Revisiting numerical errors in direct snd large eddy simulations of turbulence: Physical and spectral space analysis. *J. of Computational Physics*, 174:816–851, 2001.

[22] C. Fureby and F. F. Grinstein. Monotonically integrated large eddy simulation of free shear flows. *AIAA Journal*, 37:544–556, 1999.

[23] E. Garnier, M. Mossi, P. Sagaut, M. Deville, and P. Comte. On the use of shock capturing schemes for large-eddy simulation. *J. of Computational Physics*, 153:273–311, 1999.

[24] M. Germano, U. Piomelli, P. Moin, and W. H. Cabot. A dynamic subgrid-scale eddy viscosity model. *Phys. Fluids A*, 3:1760, 1991.

[25] S. Ghosal. An analysis of numerical errors in large-eddy simulations of turbulence. *J. of Computational Physics*, 125:187–206, 1996.

[26] S. Ghosal, T. S. Lund, P. Moin, and K. Akselvoll. A dynamic localization model for large-eddy simulation of turbulent flows. *J. Fluid Mech.*, 286:229, 1995.

[27] S. Ghosal and P. Moin. The basic equations of the large eddy simulation of turbulent flows in complex geomtry. *J. of Computational Physics*, 118:24, 1995.

[28] F. H. Harlow and J. E. Welch. Numerical calculation of time-dependent viscous incompressible flow of fluid with free surface. *Phys. Fluids*, 8:2182, 1990.

[29] C. Hartel. Turbulent flows: direct numerical simulation and large-eddy simulation. In Roger Peyret, editor, *Handbook of Computational Fluid Mechanics*, pages 283–338. Academic Press, 1996.

[30] K. Horiuti. Backward scatter of subgrid-scale energy in a wall-bounded turbulence and free shear flow. *J. Phys. Soc. Japan*, 66:91–107, 1997.

[31] K. E. Jansen. A stabilized finite element method for computing turbulence. *Computer Methods in Applied Mechanics and Engineering*, 174:299–317, 1999.

[32] J. Jimenez and R. Moser. LES: Where are we and what can we expect? *AIAA paper 98-2891*, 1998.

[33] J. Van Kan. A second order accurate pressure-correction scheme for viscous incompressible flow. *SIAM J. Sci. Stat. Comp.*, 7:870, 1986.

[34] A. R. Kerstein. Linear-eddy modeling of turbulent transport. Part 6. Microstructure of diffusive scaler mixing flields. *J. Fluid Mech.*, 231:361, 1991.

[35] A. R. Kerstein. One-dimensional turbulence: Model formulation and application to homogeneous turbulence, shear flows, and buoyant stratified flows. *J. Fluid Mech.*, 392:277, 1999.

[36] A. R. Kerstein, W. T. Ashurst, S. Wunsch, and V. Nilsen. One-dimensional turbulence: Vector formulation and application to free shear flows. *J. Fluid Mech.*, 2001. In press.

[37] A. R. Kerstein, R. C. Schmidt, S. Wunsch, W. T. Ashurst, V. Nilsen, and T. D. Dreeben. High-resolution modeling of multiscale transient phenomena in turbulent boundary-layers. Report No. SAND2001-8108, Sandia National Laboratories, 2001.

[38] J. Kim, S. J. Kline, and J. P. Johnston. Investigation of a reattaching turbulent shear layer: Flow over a backward-facing step. *J. of Fluids Engineering, Transactions of the ASME*, 102:303–308, 2001.

[39] J. J. Kim. *Investigation of Separation and reattachment of a turbulent shear layer: Flow over a backward facing step.* PhD thesis, Stanford, University, California, April 1978.

[40] W.-W. Kim. *A New Dynamic Subgrid-Scale Model for Large-Eddy Simulation of Turbulent Flows.* PhD thesis, Georgia Institute of Technology, Atlanta, Georgia, September 1996.

[41] A. N. Kolmogorov. Equations of turbulent motion of an incompressible turbulent fluid. *Izk. Akad. Nauk SSSR Ser. Phys. VI*, page 56, 1942.

[42] A. G. Kravchenko, P. Moin, and R. Moser. Zonal embedded grids for numerical simulations of wall-bounded turbulent flows. *J. Comput. Phys.*, 127:412, 1996.

[43] Y. Li. Wavenumber-extended high-order upwind-biased finite-difference schemes for convective scalar transport. *Journal of Computational Physics*, 133:235–255, 1997.

[44] D. K. Lilly. A proposed modification of the Germano subgrid-scale closure method. *Phys. Fluids A*, 4:633, March 1992.

[45] S. Liu, C. Meneveau, and J. Katz. On the properties of similarity subgrid scale models as deduced from measurements in a turbulent jet. *J. of Fluid Mechanics*, 275:83, 1994.

[46] Wing Kam Liu, Y. Chen, C. T. Chang, and T. Belytschko. Advances in multiple scale kernel particle methods. *Computational Mechanics*, 18:73–111, 1996.

[47] Wing Kam Liu, Y. Chen, J. S. Chen, T. Belytschko, C. Pan, R. A. Curas, and C. T. Chang. Overview and applications of the reproducing kernel particle methods. *Archives of Computational Methods in Engineering*, 3(1):3–80, 1996.

[48] Wing Kam Liu, Yijung Chen, R. Aziz Uras, and Ching Tang Chang. Generalized multiple scale reproducing kernel particle methods. *Computer Methods in Applied Mechanics and Engineering*, 139:91–157, 1996.

[49] Wing Kam Liu, Sukky Jun, and Yi Fei Zhang. Reproducing kernel particle methods. *International Journal for Numerical Methods in Fluids*, 20:1081–1106, 1995.

[50] T. S. Lund. On the use of discrete filters for large eddy simulation. *Annual Research Briefs 1997*, page 83, 1997. Center for Turbulence Research, Stanford University, Palo Alto, California.

[51] A. L. Marsden, O. V. Vasilyev, and P. Moin. Construction of commutative filters for LES on unstructured meshes. *J. of Computational Physics*, 175:584–603, 2002.

[52] P. J. Mason. Large-eddy simulation: A critical review of the technique. *Q. J. R. Meteorol. Soc.*, 120:1–26, 1994.

[53] P. J. Mason and A. R. Brown. The sensitivity of large eddy simulations of turbulent shear flow to subgrid models. *Boundary Layer Meteorol.*, 70:133–150, 1994.

[54] Y. Morinishi. Conservative properties of finite difference schemes for incompressible flow. *Annual Research Briefs 1995*, page 121, 1995. Center for Turbulence Research, Stanford University, Palo Alto, California.

[55] R. D. Moser, J. Kim, and N N. Mansour. Direct numerical simulation of turbulent channel flow up to Re=590. *Phys. Fluids*, 11:943, 1999.

[56] C. C. Nelson. *Simulations of Spatially Evolving Compressible Turbulence Using a Local Dynamic Subgrid Model.* PhD thesis, Georgia Institute of Technology, Atlanta, Georgia, December 1997.

[57] N. Nikitin, F. Nicoud, B. Wasistho, K. Squires, and P. Spalart. An approach to wall modeling in large-eddy simulations. *Phys. Fluids*, 12:1629, 2000.

[58] S. Nishikawa, Y. Watanabe, K. Fujitani, R. Himeno, and M. Takagi. Computational study of three-dimensional flow around a heavy-duty truck body. *Proc. EUROTECH-Direct '91, Thermofluids Eng., Birmington, UK*, 1991.

[59] S. V. Patankar. *Numerical Heat Transfer and Fluid Flow.* Hemisphere, 1981.

[60] U. Piomelli. High Reynolds number calculations using the dynamic subgrid-scale stress model. *Phys. Fluids A*, 5:1484, 1993.

[61] S. B. Pope. *Turbulent Flows.* Cambridge University Press, 2000.

[62] L. Prandtl. Bericht uber untersuchungenzur ausgebildeten turbulenz. *Z. Angew. Math. Mech*, 5:136, 1925.

[63] L. Prandtl. Uber ein neues formalsystem fur die ausgebildete turbulenz. *Nachrichten von der Akad. der Wissenschaft Gottingen*, 1945.

[64] P. Quemere, P. Sagaut, and V. Couailler. A new multi-domain/multi-resolution method for large-eddy simulation. *Int. J. Numerical Methods in Fluids*, 36:391, 2001.

[65] J. D. Ramshaw, P. J. ORourke, and L. R. Stein. Pressure gradient scaling method for fluid flow with nearly uniform pressure. *Journal of Computational Physics*, 58:360–376, 1985.

[66] P. Sagaut. *Large Eddy Simulation for Incompressible Flows.* Springer-Verlag, 2001.

[67] U. Schumann. Subgrid scale model for finite difference simulation of turbulent flows in plane channels and annuli. *J. Comput. Phys.*, 18:376, 1975.

[68] J. N. Shadid, H. K.Moffat, S. A. Hutchinson, G. L. Hennigan, G. L. Devine, and A. G. Salinger. MPSalsa: A finite element computer program for reacting flow problems Part 2: Users guide. SAND96-2331, Sandia National Laboratories, 1996.

[69] J. N. Shadid, A. G. Salinger, R. C. Schmidt, T. M. Smith, S. A. Hutchinson, G. L. Hennigan, K. D. Devine, and H. K. Moffat. MPSalsa version 1.5: A finite element computer program for reacting flow problems Part 1: Theoretical development. SAND98-2864, Sandia National Laboratories, 1998.

[70] C. W. Shu and S. Osher. Efficient implementation of essentially non-oscillatory shock-capturing schemes. *J. Comput. Phys.*, 83:32–78, 1989.

[71] P. Spalart and P. R. Allmaras. A one-equation turnulence model for aerodynamic flows. *La Recherche Aerospatiale*, 1:5, 1994.

[72] P. Spalart, R. Moser, and M. Rogers. Spectral methods for the Navier-Stokes equations with one infinite and two periodic directions. *J. Comput. Phys.*, 96:297, 1991.

[73] C. G. Speziale. Galilean invariance of subgrid-scale stress models in the large-eddy simulation of turbulence. *J. Fluid Mechanics*, 156:55–62, 1985.

[74] H. Tennekes and J. L. Lumley. *A First Course in Turbulence*. MIT Press, 1992.

[75] O. V. Vasilyev, T. S. Lund, and P. Moin. A general class of commutative filters for les in complex geometries. *J. of Computational Physics*, 146:82, 1998.

[76] E. J. Weckman and A. B. Strong. Experimental investigation of the turbulence structure of medium-scale methanol pool fires. *Combustion and Flame*, 105:245–266, 1996.

[77] T. Wei and W. W. Willmarth. Reynolds-number effects on the structure of a turbulent channel flow. *J. Fluid Mech.*, 204:57, 1989.

Distribution

External Distribution:

Prof. Patrick McMurtry

Department of Mechanical Engineering

University of Utah

Salt Lake City, UTAH 84112

Randy McDermmott

Chemical Engineering Dept.

University of Utah

Salt Lake City, UTAH 84112

Prof. Suresh Menon

School of Aerospace Engineering

Georgia Institute of Technology

Atlanta, Georgia 30332-0150

Internal Distribution:

15	0316	Rodney Schmidt, 9233
3	0316	Thomas Smith, 9233
1	0316	Joseph Castro, 9233
1	0316	Sudip Dosanjh, 9233
1	0316	David Gardner, 9233
1	0316	Robert Hoekstra, 9233
1	0316	Curtis Ober, 9233
1	0316	Roger Pawlowski, 9233
1	0196	Paul Lin, 9233
1	0196	Larry Musson, 9233
1	0318	Paul Yarrington, 9230
1	0321	Bill Camp, 9200
1	0819	Karen Devine, 9226
1	0819	Edward Boucheron, 9231
1	0819	Mark Christon, 9231
1	0819	Tim Trucano, 9231
1	0819	Thomas Voth, 9231
1	0821	Louis Gritzo, 9132
1	0825	Frederick Blottner, 9115
1	0825	Christopher Roy, 9115
1	0835	Robert Cochran, 9141
1	0835	Stefan Domino, 9141
1	0835	Steven Kempka, 9141
1	0835	James Peery, 9142
1	0836	Paul Desjardin, 9132
1	0836	Vernon Nicolette, 9132
1	0836	Sheldon Tieszen, 9132
1	1111	Andrew Salinger, 9233
1	1111	John Shadid, 9233

1 9051 William Ashurst, 8351

1 9051 Jacqueline Chen, 8351

1 9051 Alan Kerstein, 8351

1 9051 Habib Najm, 8351

1 9051 Joseph Oefelein, 8351

1 9051 Larry Rahn 8351

1 9051 James Sutherland, 8351

1 9051 Scott Wunsch, 8351

1 9018 Central Technical Files, 8945-1

2 0899 Technical Library, 9616

1 0612 Review & Approval Desk, 9612

1 0188 LDRD Office, 1030